

**FREQUENCY ADAPTIVE DISCRETE REPETITIVE CONTROLIER DESIGN
FOR ELECTRIC VEHICLE CHARGER**

DISSERTATION/THESIS

SUBMITTED IN PARTIAL FULFILLMENT OF THE REQUIREMENTS
FOR THE AWARD OF THE DEGREE
OF

MASTER OF TECHNOLOGY
IN
POWER ELECTRONICS & SYSTEMS

Submitted by:

SAKSHI CHALIA

2k20/PES/18

Under the supervision of

PROF. MUKHTIAR SINGH
(Professor, EED, DTU)



DEPARTMENT OF ELECTRICAL ENGINEERING
DELHI TECHNOLOGICAL UNIVERSITY

(Formerly Delhi College of Engineering)
Bawana Road, Delhi-110042

MAY,2022

DEPARTMENT OF ELECTRICAL ENGINEERING
DELHI TECHNOLOGICAL UNIVERSITY
(Formerly Delhi College of Engineering)
Bawana Road, Delhi-110042

CANDIDATE'S DECLARATION

I, **SAKSHI CHALIA**, Roll No. 2k20/PES/18 student of M.Tech (Power Electronics & System), hereby declare that the project Dissertation titled “**Frequency Adaptive Discrete Repetitive Controller Design for Electric Vehicle Charger**” which is submitted by me to the Department of Electrical Engineering Department, Delhi Technological University, Delhi in partial fulfillment of the requirement for the award of the degree of Master of Technology, is original and not copied from any source without proper citation. This work has not previously submitted for the award of any Degree, Diploma.

Place: Delhi

(Sakshi Chalia)

Date:

DEPARTMENT OF ELECTRICAL ENGINEERING
DELHI TECHNOLOGICAL UNIVERSITY
(Formerly Delhi College of Engineering)
Bawana Road, Delhi-110042

CERTIFICATE

I hereby certify that the Project Dissertation titled “**Frequency Adaptive Discrete Repetitive Controller Design for Electric Vehicle Charger**” which is submitted by **SAKSHI CHALIA**, Roll No. 2K20/PES/18, Department of Electrical Engineering, Delhi Technological University, Delhi in partial fulfillment of the requirement for the award of the degree of Master of Technology, is a record of the project work carried out by the student under my supervision. To the best of my knowledge this work has not been submitted in part or full for any Degree or Diploma to this University or elsewhere.

Place: Delhi

Date:

PROF. MUKHTIAR SINGH
(SUPERVISOR)

ACKNOWLEDGEMENT

I would like to express my gratitude towards all the people who have contributed their precious time and effort to help me without whom it would not have been possible for me to understand and complete the project.

I would like to thank **Prof. Mukhtiar Singh** (Professor, Department of Electrical Engineering, DTU, Delhi) my Project guide, for supporting, motivating and encouraging me throughout the period of this work was carried out. His readiness for consultation at all times, his educative comments, his concern and assistance even with practical things have been invaluable.

Besides my supervisor, I would like to thank *Dr. Aakash Kumar Seth*, and all the PhD scholars of *PE LAB* for helping me wherever required and provided me continuous motivation during my research.

Finally, I must express my very profound gratitude to my parents, seniors and to my friends for providing me with unfailing support and continuous encouragement throughout the research work.

Date: 30/05/22

Sakshi Chalia
M.Tech (Power Electronics & System)
Roll No. 2K20/PES/18

ABSTRACT

Electric vehicles (*EVs*) are very efficient, cheap, and cause less pollution to environment than internal-combustion (*IC*) engine based vehicles. As *EVs* are gaining lot of popularity globally so it becomes very important to standardize its infrastructure. This paper summarizes the various charging standards followed by different country regions globally and focuses the standards adopted by India. As of now, every standard identified with charging infrastructure depend on the European ambient conditions. As India being a tropical country, subsequently settling the *EV* charging standards, vehicle adoption pattern and India's encompassing temperature will become basic contemplations. Therefore, India has followed and modified various other standards to comply with Indian conditions

This research work introduces the designing of bidirectional two-stage, on-board electric vehicle (*EV*) charger's controller. As with the growing trend of *EVs*, their widespread use may compromise grid quality, leading to the demand for a stable, simple, and better control system. However, some controllers provide sluggish responses and fail to compensate for harmonics. Therefore, to mitigate the grid current harmonics, repetitive controller (*RC*) has been analyzed. Within a specified integer period, the *RC* may accomplish zero steady-state error tracking of any periodic signal. However, the performance of conventional *RC* degrades when grid frequency varies within the permissible range. Therefore, a Lagrange interpolating polynomial-based fractional-order *RC* has been implemented with a fixed sampling rate to enhance its performance during frequency fluctuations. The *PLL* estimated frequency has been fed back to update the controller's resonant frequency, and the fractional delay is approximated using a Lagrange interpolating polynomial. The proposed controller has been designed within a *MATLAB* environment. Its performance has also been tested in a real-time experimental setup using *OPAL-RT (4510)*.

TABLE OF CONTENTS

CANDIDATE DECLARATION	II
CERTIFICATE	III
ACKNOWLEDGEMENT	IV
ABSTRACT	V
TABLE OF CONTENTS	VI
LIST OF FIGURES	IX
LIST OF TABLES	XIII
LIST OF ABBREVIATIONS	XIV
LIST OF SYMBOLS	XVI
CHAPTER-1: INTRODUCTION	
1.1 IC engine vs Electric Vehicle	1
1.2 Electric Vehicle Technology	2
1.3 Background	4
1.4 Problem Statement and Motivation	7
1.5 Objective	8
1.6 Outline of Thesis	8
CHAPTER-2: ELECTRIC VEHICLE CHARGING STANDARDS IN INDIA AND SAFETY CONSIDERATION	
2.1 Introduction	10
2.2 Charging Power Levels and International Standards	12
2.3 Electric Vehicle Charging Standards	13
2.4 Application of EV Charging standards	16
2.5 Overview of Charging Standards in India	17
2.6 Safety Consideration of EV Charging Standards in India	21
2.7 Conclusion	23
CHAPTER-3: SYSTEM ARCHITECTURE AND PI BASED EV CHARGER CONTROLLER	

3.1 Introduction	24
3.2 Operating Modes of EV Charger	25
3.2.1 Unidirectional EV Charger's Operation	26
3.2.2 Bidirectional EV Charger's Operation	26
3.3 Controller Design	28
3.3.1 AC- DC Converter Control	28
3.3.2 DC-DC Converter Control	29
3.4 PI- Based EV Charger Control Structure	30
3.5 Results	31
3.5.1 Simulation Result	31
3.5.2 Experimental Result	34
3.6 Conclusion	35
CHAPTER-4: FUNDAMENTAL OF REPETITIVE CONTROL	
4.1 Introduction	37
4.2 RC Controller based EV Charger	38
4.3 Fundamental of Repetitive Control	39
4.3.1 Internal Model Principle	39
4.3.2 Repetitive Controller	40
4.3.3 Transfer Function for RC controller	47
4.3.4 Stability: RC System	47
4.4 Results	48
4.4.1 Simulation Results	48
4.4.2 Experimental Results	52
4.5 Conclusion	56
CHAPTER-5: FRACTIONAL ORDER REPETITIVE CONTROLLER: DESIGN AND ANALYSIS	
5.1 Introduction	57
5.2 State of Art Research	59
5.3 Repetitive Control Schemes Based on Fractional Delay Filter	60
5.3.1 Optimal Designing of Fractional Delay Filter	60
5.3.2 Design & Analysis of Fractional Order Repetitive Controller	62

5.3.3 FORC: Stability Criteria	64
5.4 Results	65
5.4.1 Simulation Results	65
5.4.2 Experimental Results	67
5.5 Conclusion	68
CHAPTER-6: RESULTS: SIMULATION AND EXPERIMENTAL	
6.1 Simulation Results	69
6.2 Experimental Results	77
CHAPTER 7: CONCLUSION AND FUTURE SCOPE OF WORK	84
APPENDIX A: MODELING OF EV CHARGER	
A.1 AC-DC Converter Modeling (Single-phase)	86
A.2 Battery Pack Modeling	89
A.2 DC-DC Converter Modeling	90
APPENDIX B: COMPONENT CALCULATION	
B.1 DC Link Voltage	94
B.2 DC Link Capacitance	94
B.3 DC-DC Converter Filter	95
BIBLIOGRAPHY	96

LIST OF FIGURES

S No	Figure Name	Page no.
1	Figure 1.1. Classification of Electric Vehicles	2
2	Figure 1.2. Flow of power in EVs (a)PHEV (b)BEV.	3
3	Figure 1.3: Typical architecture of an Electric Vehicle	4
4	Figure 2.1: EV charging standards followed by various countries.	13
5	Figure 2.2: (a) AC and DC charging ports (b) AC and DC charging connectors, followed by different countries.	17
6	Figure 2.3: Public Charging Characterization of EVs in India	19
7	Figure 2.4: (a) Indian electrical safety regulations based on IS: 13252-2010. (b) Indian standard for EV safety.	22
8	Figure 3.1: Architecture of two-stage on- board charger	25
9	Figure 3.2: Operating mode for Unidirectional charger	26
10	Figure 3.3: Operating mode for Bidirectional charger	27
11	Figure 3.4: Overall control structure for two- stage EV charger	28
12	Figure 3.5: Dual-loop control for AC-DC converter	29
13	Figure 3.6: Control architecture of AC-DC converter	29
14	Figure 3.7: Control architecture of DC-DC converter	30
15	Figure 3.8 PI based control algorithm for EV charger	31
16	Figure 3.9. Simulation results of measured P - Q , grid current (I_g), DC-link voltage (V_{dc}), battery voltage (V_{bat}), battery current (I_{bat})	32
17	Figure 3.10 Transition of active-reactive power and grid current from (a) Mode-1 to 2, (b) Mode-3 to 4.	33
18	Figure 3.11. THD in grid- current (a) Mode 1 (b) Mode 2 (c) Mode 3 (d) Mode 4	34
19	Figure 3.12. Transition between (a) Mode 1-2, (b) Mode 3-4: grid voltage-current, DC-link voltage, and battery current, battery voltage & frequency.	35
20	Figure 4.1 RC based control algorithm for EV charger	38
21	Figure 4.2 Block diagram of discrete-integrator	39
22	Figure 4.3: Block diagram of standard memory-loop (discrete domain)	40

23	Figure 4.4: Conventional RC	40
23	Figure 4.5: Frequency response of RC (a) within the range of angular frequency of 1 rad/sec to 105 rad/sec (b) frequency sensitivity illustration at 3rd harmonics	41
24	Figure 4.6: Conventional Repetitive Controller Structure	43
25	Figure 4.7: Feed- forward Repetitive Controller Structure includes feed-forward command signal	43
26	Figure 4.8: RC with plug-in structure	43
27	Figure 4.9: Block Diagram of discrete time RC structure	44
28	Figure 4.10: Pole zero plot of an internal model $\left(\frac{z^{-200}}{1-z^{-200}}\right)$, illustrating all the poles on the boundary of unity circle	44
29	Figure 4.11 Magnitude response of different $Q(z)$: low-pass filter	45
30	Figure 4.12 Pole-zero plot of internal model $\left(\frac{z^{-400}}{1-z^{-400}}\right)$, along with different $Q(z)$ filters: (a) $Q(z) = 0.25z^{-1} + 0.5 + 0.25z^1$ (b) $Q(z) = 0.15z^{-1} + 0.7 + 0.15z^1$ (c) $Q(z) = 0.05z^{-1} + 0.9 + 0.05z^1$	46
31	Figure 4.13. Measured grid-voltage (V_g), grid-current (I_g), active (P) - reactive (Q) power, DC-link voltage (V_{dc}), battery-voltage (V_{bat}) and battery-current (I_{bat}).	49
32	Figure 4.14 Measured grid-voltage (V_g) and grid-current (I_g) during transition from (a) Mode 1 to Mode 2 (b) Mode 3 to Mode 4	49
33	Figure 4.15 THD in I_g (a) Mode 1 (b) Mode 2 (c) Mode 3 (d) Mode 4.	50
34	Figure 4.16 Phase difference between I_g and V_g due to frequency deviation (a) at 49.5Hz (b) at 50.5Hz.	51
35	Figure 4.17. THD in grid I_g without frequency adaptability when grid frequency (a) 50 Hz (b) 49.5 Hz and (c) 50.5 Hz	52
36	Figure 4.18. Transition with RC from (a) Mode 1 to 2 and (b) Mode 3 to 4.	53
37	Figure 4.19. THD in I_g in all operating modes (a) Mode 1 (b) Mode 2 (c) Mode 3 (d) Mode 4	54
38	Figure 4.20. Phase difference between I_g and V_g due to frequency deviation (a) at 49.5Hz (b) at 50.5Hz.	55
39	Figure 5.1 For fractional delay range ($F = 0:0.1:0.9$) magnitude response plot of Lagrange-interpolation based FD filter (a) $L = 1$ (b) $L = 2$, (c) $L = 3$	61

40	Figure 5.2: a) Fractional order repetitive control (b) Block diagram of the frequency adaptive RC.	62
41	Figure 5.3. No phase difference between I_g and V_g with frequency adaptability due to frequency deviation (a) at 49.5Hz (b) at 50.5Hz.	66
42	Figure 5.4. THD in grid I_g with frequency adaptability when grid frequency (a) 49.5 Hz and (b) 50.5 Hz.	66
43	Figure 5.5. Steady-state performance of the frequency adaptive RC controller at (a) 49.5 Hz (b) 50.5 Hz	67
44	Figure 6.1: Measured grid-voltage (V_g), grid-current (I_g), active (P) - reactive (Q) power, DC-link voltage (V_{dc}), battery-voltage (V_{bat}) and battery-current (I_{bat}).	70
45	Figure 6.2: Measured grid-voltage (V_g) and grid-current (I_g) during transition with RC from (a) Mode 1 to Mode 2 (b) Mode 3 to Mode 4	71
46	Figure 6.3: Transition from mode 1 to 2 with RC controller	72
47	Figure 6.4: THD in grid I_g without frequency adaptability when grid frequency (a) 50 Hz (b) 49.5 Hz and (c) 50.5 Hz.	72
48	Figure 6.5: Phase difference between I_g and V_g without frequency adaptability due to frequency deviation (a) at 49.5Hz (b) at 50.5Hz.	74
49	Figure 6.6: THD in grid I_g with frequency adaptability when grid frequency (a) 49.5 Hz and (b) 50.5 Hz.	75
50	Figure 6.7: No phase difference between I_g and V_g with frequency adaptability due to frequency deviation (a) at 49.5Hz (b) at 50.5Hz	76
50	Figure 6.8: THD comparison	76
52	Figure 6.9: Hardware Setup (a) Hardware Setup (b) Battery bank	77
53	Figure 6.10: Transition with RC from (a) mode 1 to 2 and (b) mode 3 to 4.	79
54	Figure 6.11: THD in I_g at 50 Hz (a) Mode 1 (b) Mode 2 (c) Mode 3 (d) Mode 4	80
55	Figure 6.12: Steady-state performance of the RC without frequency adaptability scheme at (a) 49.5 Hz (b) 50.5 Hz	81
56	Figure 6.13: Steady-state performance of the frequency adaptive RC controller at (a) 49.5 Hz (b) 50.5 Hz	82
57	Figure 6.14: Dynamic performance of the frequency adaptive technique under grid frequency step changes (a) 49.5 Hz – 50.5 Hz (b) 50.5 Hz – 49.5 Hz	83
58	Figure A.1: AC-DC converter switching model	86
59	Figure A.2: Battery pack equivalent model	89
60	Figure A.3: DC-DC Converter	90

61	Figure A.3: Buck operation state: ON	91
62	Figure A.5: Buck mode operation: OFF	92
63	Figure A.6: Two- stage bidirectional EV charger's average model	93

LIST OF TABLES

S No	Table Name	Page no.
1	Table I: Summary of charging level standards for electric vehicles	12
2	Table II: SAE AC charging levels	14
3	Table III: SAE DC charging levels	15
4	Table IV: IEC-62196 summary	15
7	Table V: Modes of Charging Operation	28
8	Table VI: System Parameter	69
9	Table VII: Modes of Operation	70

LIST OF ABBREVIATIONS

S No	Abbreviated Name	Full Name
1	EV	Electric Vehicle
2	IC	Internal Combustion Engines
3	CNG	Compressed Natural Gas
4	FCEV	Fuel Cell Electric Vehicle
5	HEV	Hybrid Electric Vehicle
6	AEV	All- Electric Vehicle
7	BEV	Battery Electric Vehicle
8	PHEV	Modified Genetic Algorithm
9	AC	Alternating Current
10	DC	Direct Current
11	DG	Distribution Grid
12	DSP	Digital Signal Processor
13	PI	Proportional Integral
14	RC	Repetitive Controller
15	RES	Resonant Controller
16	THD	Total Harmonic Distortion
17	MRES	Multiple Resonant Controller
18	SHC	Selective Harmonic Control
19	DCFC	DC Fast Charging
20	OBC	On-board Battery Chargers
21	ISO	International Organization for Standardization
22	SAE	Society of Automotive Engineers
23	IEEE	Institute of Electrical and Electronics Engineers
24	IEC	International Electrotechnical Commission
25	GB/T	Guobiao
26	IS	Indian Standard
27	AISC	Automotive Industry Standards Committee
28	DCFC	DC Fast Charging
29	DER	Distributed Energy Resources

30	SAC	Standardization Administration of China
31	CCS	Combined Charging System
32	BEVC- AC001	Bharat EV charger-AC001
33	BEVC- DC001	Bharat EV charger-DC001
34	ARAI	Automotive Research Association of India
35	AIS	Automotive Industry Standard
35	CAN	Controlled Area Network
36	OCPP	Open Charge Point Protocol
37	MoRT&H	Ministry of Road Transport & Highways
38	TSC	Technical Standing Committee
39	SMC	Sliding Mode Control
40	MPC	Model Predictive Control
41	PR	Proportional Resonant
42	HB	Hysteresis Band
43	FLC	Fuzzy Logic Controller
44	IMP	Internal Model Principal
45	G2V	Grid to Vehicle
46	V2G	Vehicle to Grid
47	V2V	Vehicle to Vehicle
48	PWM	Pulse Width Modulation
49	FD	Fractional Delay
50	FORC	Fractional Order Repetitive Controller

LIST OF SYMBOLS

S. NO.	SYMBOLS	DESCRIPTION
1	f_s, T_s	Sampling Frequency, Sampling Time
2	f_o	Fundamental Frequency
3	L	Grid Side Inductor
4	I_g, V_g	Grid Current, Grid Voltage
5	L_f, C_f	DC-DC side filter inductor & capacitor
6	C_{dc}	DC-link Capacitor
7	I_g^*, V_{dc}^*	Reference grid current, reference DC-link voltage
8	P, Q	Active power, Reactive power
9	P^*, Q^*	Reference active power & reference reactive power
10	ω	Periodic Angular Frequency
11	ω_0	Fundamental Angular Frequency
12	$G_c(z)$	Phase-lead Compensator
13	$Q(z)$	Low-pass Filter
14	$G_p(z)$	Plant transfer function

Chapter 1

INTRODUCTION

1.1 IC engine vs Electric Vehicle

With the increasing population, engine-based vehicle use may become 2.5 billion by 2050, which may lead to a shortage of fossil fuels and cover all the cities with extreme air pollution [1]. To limit this, a paradigm shift in perspective is needed for maintainable vehicle; it implies the utilization of low or zero discharge vehicles, most extreme usage of public vehicles, utilization of sustainable power source.

Electric vehicles (*EVs*) are the best example of sustainable transportation. Its contribution in world's transportation sector to remove the harmful emissions is increasing day by day. Electric vehicles are the best replacement of internal- combustion (*IC*) engine-based vehicles for addressing enhancement in pollution, global warming, depleting natural resources etc. As gasoline, which is petrol, diesel, compressed natural gas (*CNG*) can be used as a fuel in vehicles. There are various types of pollutants and greenhouse gases are released as emission from vehicles which becomes a reason for smog, and air pollution. The particulates released in the combustion cycle are in range of micrometers. Due to small size these cannot be filtered out by human nose/throat and effects heart or lungs after entering the body [2].

However, in terms of efficiency, an *EV* has higher energy efficiency. If fuel tank is compared to vehicle efficiency, an *IC* engine-based vehicle has 16% efficiency. Whereas an *EV* and fuel cell electric vehicle (*FCEV*) provides 72% and 40% efficiency respectively at the wheels if the starting source is taken as 100% [3].

Despite of so many benefits of *EV*, there are some issues that need to be considered are limited driving range, high costs, battery life issues and charging. It is found that driving range go down by 41% when the temperature dropped to 20° Fahrenheit [4]. However, the driving range can be extended by increasing the energy levels of battery pack, but it can be increased only up to a certain size and mass to achieve good results. Charging infrastructure is also a problem for *EVs*, a smaller number of charging station are built as compared to gas stations.

1.2 Electric Vehicle Technology

Hybrid electric vehicles (*HEVs*) and all-electric cars (*AEVs*) are the two basic types of *EVs*. *AEVs* have only electric motors that are powered by electricity [5]. *AEVs* are further divided into two types: battery electric vehicles (*BEVs*) and fuel cell electric vehicles (*FCEVs*). There is no need for an external charging system with an *FCEV*. A *BEV*, on the other hand, relies solely on grid electricity to charge its storage unit. A plug-in hybrid electric vehicle (*PHEV*) is a type of *HEV* that can recharge its battery from the grid.

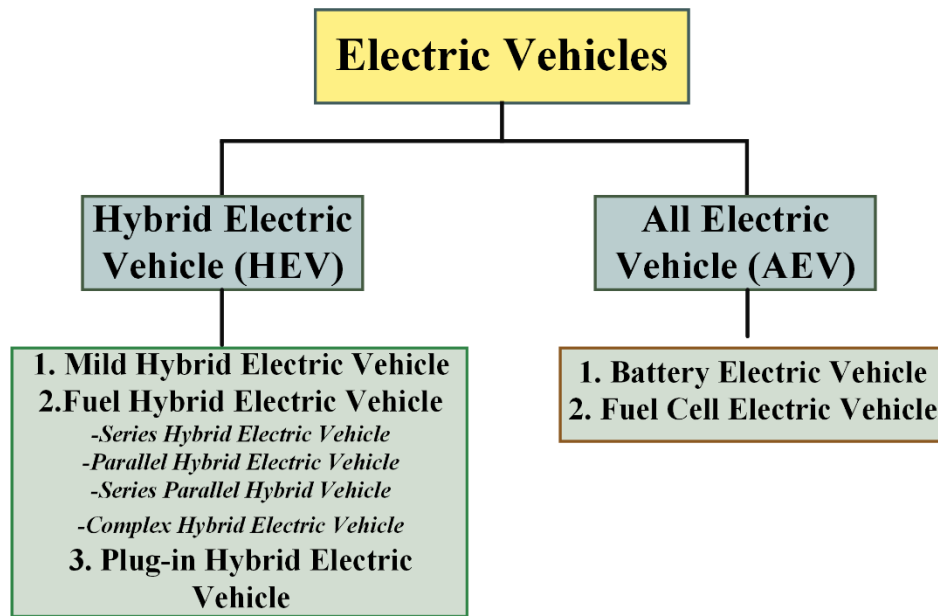


Fig.1.1. Classification of Electric Vehicles

BEVs and *PHEVs* are referred to as *EVs* in this study. Fig.1.1. depict the classification of various types of electric vehicles, while Fig.1.2. depicts the power flow from the energy source to the wheels. As illustrated in Fig. 1.3 [6], the *EV* consists primarily of three electric components: an electric motor with gearbox, an energy storage system (battery), and a power electronics converter for battery charging and motor driving. To solve the problem of a limited driving range Fast *EV* charging are required in electric vehicles [7]. On-board and off-board charging are the two forms of charging [8]. OFF board chargers are outdoor chargers and are put outside, whilst ON board chargers are positioned inside the automobile. Two-stage or single-stage *EV* chargers are available [9].

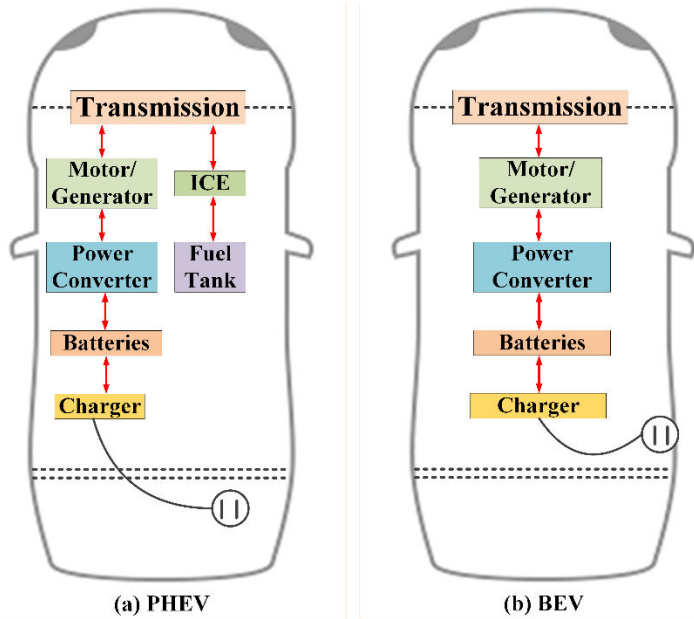


Fig.1.2. Flow of power in EVs (a) PHEV (b) BEV

Charger with only one stage only has one power conversion step, which is *AC* to *DC*. The grid is linked to the *AC* side, while the battery pack of vehicle is connected to the *DC* side [10]- [11]. Dual-stage *EV* chargers, on the other hand, are made up of two back-to-back coupled power conversion stages, such as *AC-DC* and *DC-DC* converters [11]. The second-stage *DC-DC* converter lowers battery ripple and offers galvanic isolation between the grid and the battery pack. A *DC-DC* stage between the battery and the *AC-DC* conversion stage is recommended from the perspective of battery life.

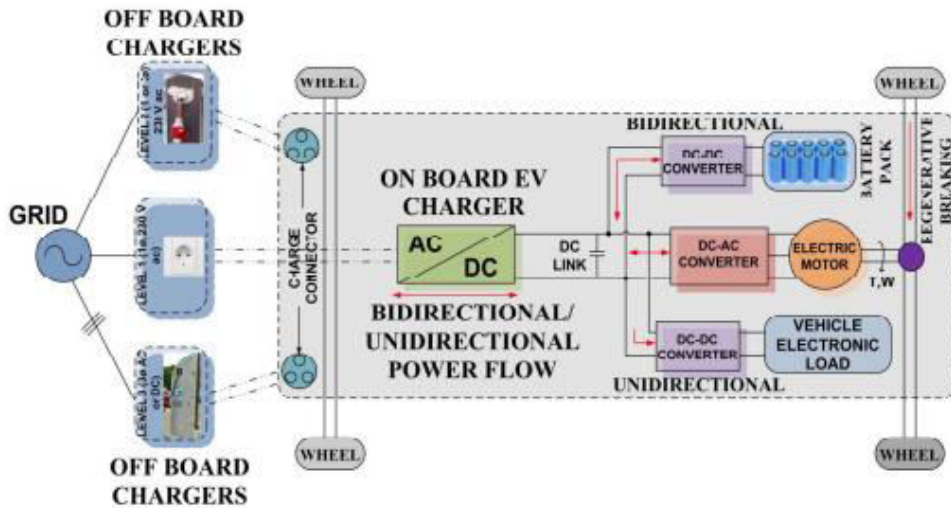


Fig.1.3. Typical architecture of an Electric Vehicle

The adoption of a *DC-DC* stage, on the other hand, will raise the hardware cost, as well as the efficiency and component count. Furthermore, as compared to two-stage chargers, single-stage chargers have a lower control complexity, but they must have a greater *DC* link voltage than the *AC* side voltage amplitude. However, in line with battery characteristics, the *EV* charger achieves the required voltage level through a two-stage conversion.

1.3 BACKGROUND

The main enabling technology for renewable energy source management and load integration is power electronics [13,14]. Smart power electronic systems with high efficiency can accurately convert, regulate, and condition electricity [15]. Grid converters (power electronic interfaces) enable large penetration of distribution grids (*DGs*) into electrical grids [16–19]. Grid converters have a wide range of power conditioning capabilities. Power distribution networks may be changed into flexible, interactive, bidirectional smart grids that distribute electricity more effectively with more grid converter interfaced *DGs*.

As the popularity of electric vehicles grows, their high penetration on the power distribution grid can lead to catastrophic issues such as excessive fault current, induces harmonic, phase difference, frequency, and voltage deviations. As *EVs* are nonlinear load on the grid, a variation in power generation and consumption might cause a frequency divergence in the system. Furthermore, the power converters used in *EV* charging systems might emit harmonics. These produced harmonics can increase power losses, device failure, and system instability [3]. As a result, to overcome the aforementioned issues, grid converters require high-performance control techniques to regulate voltage, current, and frequencies, assuring robustness, minimal steady-state error, preserving fast transient response, yet being practical. To meet system requirements, power electronics converters must use high-performance control techniques to manage voltages, currents, and/or frequencies with minimal steady-state error while preserving fast transient response, ensuring resilience, and being practical in practice. In other words, high-performance control techniques must be precise, stable, fast, and easy to execute. Because

the system's fundamental electrical signals (voltage and current) are periodic ac signals, an associated control challenge is how to precisely follow periodic ac signals.

Various control techniques, such as synchronous-frame proportional-integral [20], sliding mode control [21], predictive control [22], and hysteresis control [23], have been created with the advent of fast switching power devices, microcontrollers, digital signal processors (*DSPs*), and control strategies in EVs. Synchronous-frame *PI* controller is best suited for three-phase converters and can only regulate sinusoidal fundamental frequency signals. The performance of a predictive controller is susceptible to uncertainties and disturbances, and it is entirely reliant on an accurate model. Sliding mode and hysteresis control's erratic switching patterns can make low-pass filtering difficult, and switching devices and microprocessors might be stressed. As a result, these control techniques fail to provide a sufficient power converter control solution.

The Internal Model Principle (*IMP*) was developed by Francis and Wonham in the 1970s and asserted that complete asymptotic rejection/tracking of a persistent input could only be achieved by reproducing its signal generator (internal model) in a stable feedback loop [24–26]. To assess the effect of a system command, the internal model simulates the system's (plant) response. The *IMP* is used in both the Repetitive Controller (*RC*) and the Resonant Controller (*RES*). The feedback control scheme of *IMP*-based controllers is modified to achieve zero steady-state tracking error of the reference signal in three sorts of scenarios.

These are:

- When the goal is a periodic (command or reference) signal.
- When the goal is to cancel or reject periodic disturbance and obtain constant dc output in case where the desired output signal is constant but there is a periodic disturbance.
- When the desired output and the disturbance signal have the same frequency and the goal is to produce a zero steady-state tracking error of a periodic reference in the presence of periodic disturbance.

Any periodic signal may be broken down into its fundamental frequency and an infinite number of harmonic components. We can compute the steady state frequency response to

each of these frequencies using traditional control approaches. However, because infinite harmonic frequencies are not practicable to accommodate, a compromise is made and zero steady-state error is only obtained up to a certain cutoff frequency, generally the Nyquist frequency. With zero steady-state error, RC and RES can perfectly track/reject periodic reference/disturbance waveforms. The internal model principle based periodic control techniques (*RC & RES*) provide potential high performance control approaches for grid converters since the grid electrical variables (voltage and current) are periodic. Grid converters are frequently controlled using periodic control schemes (RC & RES).

By incorporating the generator in a closed-loop system, a resonant controller may accomplish precise tracking of a sinusoidal signal based on the IMP [26]. A parallel combination of Multiple Resonant Controllers (MRES) can be utilized to remove corresponding harmonics to minimize Total Harmonic Distortion (THD) [27, 28]. Because of the parallel construction, MRES may have independent gain for each resonant control component, resulting in a very quick transient response. However, MRES may generate a severe calculation burden and parameter tuning problem if the number of resonant control components is considerable [27]. RES has been a common current regulator for grid converters due to its simplicity and efficacy [49-33].

RC may also regulate periodic waveform signals with zero steady-state error using the IMP but with a poor dynamic response. On the other hand, RES, on the other hand, is fast but only eliminates single-frequency components [27, 28]. At all harmonic frequencies, RC is comparable to a parallel combination of a PI controller and RES components [27, 28, 29]. By delivering the same yet very high gains at all harmonic frequencies, these RES components enable RC to reject all harmonics (also called resonant frequencies). Because of its recursive nature, RC uses far less computing power than MRES. On the other hand, RC systems, on the other hand, cannot have an optimal transient response since the gains for all RES components of RC are identical.

Because the control gain at all harmonic frequencies is the same, RC generally produces substantially slower transient response than MRES. Selective Harmonic Control (SHC) was developed to govern the featured $n \pm mk$ order harmonics of grid converters in order to provide a good trade-off between accuracy but sluggish RC and high computational

burden but rapid RSC. Selective harmonic RC (SHC) is another name for SHC, which is compatible with RC. Grid converters are controlled using periodic control techniques such as RC, RSC, and SHC [27].

1.4 PROBLEM STATEMENT AND MOTIVATION

The discrete domain is used to create repetitive control in most applications. That is, computations are only conducted at specific times (e.g., at T_s , $2T_s$, $3T_s$, etc.) and the signal created by the repeating controller is a discrete time periodic signal. It is necessary that the sampling frequency ($f_s = 1/T_s$) and the reference signal frequency (f) be integers in order for the number of samples per reference signal period to be an integer. Because of the intermittent DG systems, the frequency of the electrical power system is growing more and more variable. As a result, in the case of grid connected converters, the sampling frequency to grid frequency ratio cannot always maintain an integer value, because the grid frequency varies owing to a brief imbalance between load and produced power, and among many other things. In India, practically, grid frequency varies within a specific range, i.e., 49 Hz to 51 Hz. When frequency fluctuates due to brief fluctuations, system operators restore the frequency to the usual band as soon as practically possible, taking into account all of the factors surrounding the fluctuation [34]. The sampling to reference frequency ratio might become non-integer due to the typical frequency band and transient changes. The non-integer samples would cause a repetitive controller's resonant frequencies to stray from the grid frequencies (fundamental and harmonics). That is, RC cannot precisely monitor or reject grid frequency periodic signals. Grid converters pump inter-harmonic currents into the grid as a result, causing power-flow oscillations. A non-integer number of samples per period affects electricity quality and may possibly jeopardize grid operation.

Variable sample rate RC or RES can be utilized to prevent the issue caused by changing grid frequency. However, due to its complexity and other factors, the variable sampling rate approach is rarely employed. According to preliminary study, fractional-period repetitive control technology may successfully handle fractional-period or variable frequency periodic signals. [35] proposes an adaptive repetitive control for tracking a variable period signal with a fixed sample time. For three-phase grid inverters, Rashed et al. [33] developed a technique that employed estimated grid frequency to adaptively update

the RC period and RSC resonant frequency, while interpolation was used to retain the RC rejection ability under non-integer samples per period. Fractional delay-based repetitive control techniques, on the other hand, can be utilized, where a fractional delay low pass filter is used to simulate the internal model (signal generator) of fractional-period signals [36,37]. To develop fractional delay low-pass filters, the Lagrange interpolation approach was utilized.

1.5 OBJECTIVE

This thesis contributes to the topic of “Discrete RC based frequency adaptive controller for EV charger”. In the research work, primarily two-stage On-board electric vehicle charger has been simulated using repetitive control structure. The computational results illustrate that RC systems are unable to regulate a changing frequency reference signal because the steady-state tracking error is quite large. As a result, the goal of this study is to create sophisticated periodic control technology to cope with time-varying periodic signals, allowing grid converters to precisely track periodic voltages or currents for improved power quality and power conditioning. The controllers of electric vehicle chargers were evaluated in four distinct modes, including charging/discharging and reactive power compensation. All suggested control techniques' performance has been simulated and tested in a MATLAB/Simulink environment. Its performance has also been tested in a real-time experimental setup using *OPAL-RT (4510)*.

1.5 OUTLINE OF THESIS

As stated previously, the primary goal of the thesis is to develop a battery voltage equalization, which involves a thorough examination of the architecture and modes of the proposed topology, switching mechanism, and control strategy. The thesis is organized as follows:

Chapter-1: This chapter provides the reader with an introduction of Electric Vehicle technology and background on the importance of control structure. The various issues happen on the grid.

Chapter-2: This chapter elaborates the *EV* charging standards followed by various countries. It also covers the major charging standard and safety consideration followed in India in detail.

Chapter-3: This chapter includes the architectural study of the *EV* two-stage on-board charger in detail along with the operating modes. It also detailed about the dual- loop control strategy. A *PI*-based *EV* charger controller has been developed and analyzed.

Chapter-4: Fundamental of RC has been explained in this chapter in detail. The stability of the RC system has also been analyzed. An *RC* based control structure for *EV* charger has been developed and detailed analysis of the performance of repetitive control scheme under variable grid frequency has been done.

Chapter-5: This chapter deals with the fractional order RC control strategy. It presents contribution to the design of Fractional Order Repetitive Controller (*FORC*) and stability analysis of *FORC* controlled systems.

Chapter-6: This chapter validates the result of frequency adaptive *RC*. Both simulation and experimental results has been verified.

Chapter-7: This chapter summaries the contributions of this thesis and highlights potential future research opportunities.

Chapter 2

ELECTRIC VEHICLE CHARGING STANDARDS IN INDIA AND SAFETY CONSIDERATION

2.1 INTRODUCTION

With increasing population, engine-based vehicle use may become 2.5 billion by 2050 which may lead to the shortage of fossil fuels and may cover all the cities with extreme air pollution [1]. To limit this, a paradigm shift in perspective is needed to maintainable vehicle it implies utilization of low or zero discharge vehicles, most extreme usage of public vehicle, utilization of sustainable power source.

Electric vehicles (*EVs*) are the best example of sustainable transportation. Its contribution in world's transportation sector to remove the harmful emissions is increasing day by day. Electric vehicles are the best replacement of internal-combustion (*IC*) engine-based vehicles for addressing enhancement in pollution, global warming, depleting natural resources etc. As gasoline, which is petrol, diesel, compressed natural gas (*CNG*) can be used as a fuel in vehicles. There are various types of pollutants and greenhouse gases are released as emission from vehicles which becomes a reason for smog, and air pollution. The particulates released in the combustion cycle are in range of micrometers. Due to small size these cannot be filtered out by human nose/throat and effects heart or lungs after entering the body [2].

However, in terms of efficiency, an EV has higher energy efficiency. If fuel tank is compared to vehicle efficiency, an IC engine-based vehicle has 16% efficiency. Whereas an EV and fuel cell electric vehicle (FCEV) provides 72% and 40% efficiency respectively at the wheels if the starting source is taken as 100% [3].

Despite of so many benefits of EV, there are some issues that need to be considered are limited driving range, high costs, battery life issues and charging. It is found that driving range go down by 41% when the temperature dropped to 20 degrees Fahrenheit [4]. However, the driving range can be extended by increasing the energy levels of battery pack, but it can be increased only up to a certain size and mass to achieve good results.

Charging infrastructure is also a problem for EVs, a smaller number of charging station are built as compared to gas stations.

Generally, EV has battery pack with Li-ion cells and to charger this pack, three types of charging Levels are utilized i.e., level 1, level 2 & level 3. Level 1 is slow charging corresponds to supply voltage of 110V–120 V while level 2 (semi-fast) is of 220V–240 V and level 3 (fast) or DC fast charging (DCFC) is of 200V–800 V [1]. On-board battery chargers (OBC) are restricted by size, weight, and volume for this reason they are typically viable with level 1 (supports 110- 120V) and level 2 (220-240V) chargers. The level 3 (200- 800V) charger requires high charging voltage and current, therefore it cannot be installed onto the vehicle as it is higher in weight and requires larger space [38].

As EVs are evolving globally, it becomes essential to standardize the related aspects for the uniform operation. ISO i.e., International Organization for Standardization is among the EV charging component standardization organizations that deals with EVs standardization and the rest works on the specification of component level [2]. Every country follows different standards like society of automotive engineers (SAE), institute of electrical and electronics engineers (IEEE), international electrotechnical commission (IEC), Guobiao (GB/T) and CHAdeMO. The USA follows IEEE standards where IEC standards is utilized by Europe. The CHAdeMO standards is followed by Japan. Whereas the IEC and SAE are mostly used standards in worldwide [39,40,41].

The EV charging standards used in India are AC-001 specified by Indian standard (IS): 17017 and DC-001 specified by IS: 17017-1 for low voltage EV applications. India is in the stage of developing the EV standards for medium as well as high voltage applications. Whereas right now India is using IEC standards for AC high voltage charging and SAE/CHAdeMO for DC high voltage charging applications [42,43,44].

With the global regulatory landscape dynamic evolvement, the standardization of charging infrastructure is very crucial and with this electrical safety is a key concern. Safety, compatibility, and performance are three basic regulation aspects. In India, some safety regulations of international and national standard are taken up by Indian agencies like automotive industry standards committee (AISC) for featuring the need of harmonization [45]. This chapter discusses about the international standards for EV charging and further

focus on charging standards used by Indian organizations and safety requirements.

2.2 CHARGING POWER LEVEL AND INTERNATIONAL STANDARDS

Gas and diesel-based vehicles have been in existence for more than 100 years, and the business has built up a vigorous refueling foundation for the help of billions of vehicles. Nonetheless, with the new ascent in emerging trends of electric vehicles, new "refueling" methods are developing practices. The three EV charging levels i.e., level 1, level 2 & level 3 (DCFC) are summarized in table I.

Table I
SUMMARY OF CHARGING LEVELS STANDARDS FOR ELECTRIC
VEHICLES.

Charging Specification	Level 1	Level 2	Level 3 (DCFC)
Voltage	120 V AC @60Hz	240 V AC @60Hz	2 00-800V D.C
Current (A)	15	40	60
Charge Time	Up to 20 hrs.	Up to 7 hrs.	Up to 30 min
Vehicle Charge Port	Nema 515, Nema 520	SAE J1772, Nema 1450, Nema 6-50	CHAdEMO, SAE
Power Equivalent	Toaster	Clothes dryer	15 Central A.C.
Installation	Self	Professional	Professional

Level 1: The basic EV charging level is Level 1 charger. It is charged from a standard 120 V household outlet, which gives around 4 to 5 miles of reach in one hour of charging. Most of EV producers incorporate Level 1 EVSE cord set, therefore no extra charging hardware is required. A totally drained EV battery requires around 20 hours to fully re-energize [3]. Level 1 charging is for the most part kept to North, South and Central

America, Europe and a large part of the world uses a 220 V inventory framework. Around 500-880 USD installation cost is required for this type of charging method.

Level 2: Level 2 charging equipment utilizes 220 V supply system private or 208 V for an outside charging station [3]. A 3.3 KW on-board charger gives around 15 miles of travelling in an hour of charging. However, a 6.6 KW on-board charger gives around 30 miles of travel in same time span of charging. Level 2 EVSE uses gear explicitly intended to give speed up recharging and requires proficient electrical establishment utilizing a devoted electrical circuit. Around 1000-3000 USD establishment cost is required for Level 2 charging system.

Level 3 OR DCFC: The Level 3 charging system requires 480 V AC supply system. This type of charger gives around 80-100 miles of travelling in 20-30 minutes of charging. The DCFC converts AC supply into DC and then DC supply is sent directly to EV battery pack. This level of charging is suitable only for commercial usage not for residential locations. The executing cost is between 30000-160000 USD. The summary of all charging levels is listed in Table I.

2.3 Electric Vehicle Charging Standards

There are a few guidelines accessible globally which manage EV charging foundation. Fig.2.1 shows the country region and their EV charging standard organization. The SAE and IEEE standards are utilized in USA. based makers while IEC is limitlessly utilized in Europe. Japan and China have their own EV charging norms named CHAdeMO and Guobiao (GB/T) standard respectively. Guobiao (GB/T) standard given by the Standardization Administration of China and Chinese National Committee of ISO and IEC for AC and DC charging. However, GB/T AC charging principles are like IEC norms. All these major standards are explained below and summarized in Tables.

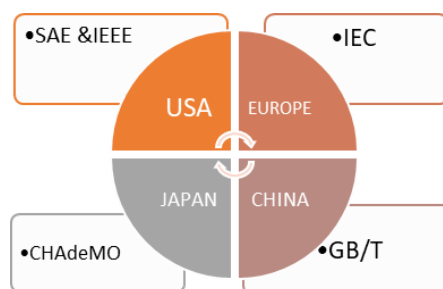


Fig. 2.1. EV charging standards followed by various countries.

SAE Standards: The SAE international have 128,000 members from over 100 nations. This standard for Level 1 and level 2 EVSE is accommodated onto the vehicle. Whereas for fast DC charging it should be outside the vehicle. The SAE worldwide coordinates the advancement of technical standards based on best practices distinguished and portrayed. They developed the EV charging standards for both AC and DC supply system. SAE: J1772 discuss all the equipment ratings for EV charging includes circuit breaker, current rating of charging voltage and so on. The voltage and current ratings of AC and DC charging system according to SAE: J1772 are listed in Table II and III respectively [46].

Table II
SAE AC CHARGING LEVELS

Charging System	Supply System	Maximum Current (A)	Branch Circuit Breaker Rating (A)	Power Rating (KW)
AC Level 1	1- ϕ , 120 V	12	15	1.44
		16	20	1.92
AC Level 2	1- ϕ , 208-240 V	≤ 80	AS PER NEC625	UP TO 19.2

Table III
SAE DC CHARGING LEVELS

DC Charging System	EVSE DC Output Voltage (V)	Maximum Current (A)	Power Rating (kW)
Level 1	200-450	80	36
Level 2	200-450	200	90
Level 3	200-600	400	240

IEC Standards: The IEC is a non-benefit, non-administrative worldwide norms association that prepares International Standards for electrical, electronic, and related technologies. The IEC: 62196 is an international standard for plugs, sockets outlet, electrical connectors, and vehicle inlet for EVs. [3]. Moreover, a Combined Charging system (CCS) is developed which have combo 1 and 2 connectors. These connectors are the extension of IEC: 62196 type 1 and 2 connectors with additional DC contacts for high power up to 350 KW DC fast charging. IEC defines the power levels in Modes as summarized in Table IV [47].

Table IV
IEC-62196 SUMMARY

Source	Mode	Voltage (V)	Supply System	Maximum Current (A)
AC	Mode 1	240	1- ϕ	16
	Mode 2	240	1- ϕ	32
	Mode 3	415	3- ϕ	250
DC	Mode 4	600	DC	400

IEEE Standards: The IEEE is world's biggest specialized proficient affiliation devoted to propelling innovation to support humankind. The IEEE Standard 2030.1.1TM-2015 explains fundamental interoperability and characterizes prerequisites for the plans of EVs and DC fast chargers. The IEEE: 2030.1.1 is for fast DC charging of EVs [4]. IEEE: 1547 summarized “Standards for interconnecting distributed resources with electric power systems.” It is pertinent for all Distributed Energy Resources (DER) technologies with an aggregate limit of 10 MVA, covers necessities applicable to the performance, operation, testing, safety contemplations and maintenance for DERs interconnection, and emphasizes on the establishment of DERs on primary and secondary networks distribution systems. [48]











CHAdEMO Standards: The CHAdEMO Research and Development began in 2005 determined to build up a public foundation of quick chargers that empowers individuals to

drive EVs. The principal business CHAdeMO charging foundation was appointed in 2009 and CHAdeMO was distributed as IEC standard in 2014 (IEC: 62196-3 arrangement AA for connector and IEC: 61851-23 for charging framework). Around the same time, CHAdeMO was published as European Committee for Electrotechnical Standardization, followed by the distribution as IEEE Standard 2030.1.1TM-2015. CHAdeMO is for DC fast charging delivering up to 400 kW by 400 A, 1000 V DC [49].







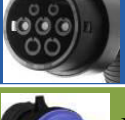



GB/T: The Standardization Administration of China (SAC) issued Chinese national standards i.e., GB standards. The GB/T: 20234 specifies about the general requirements for conductive charging of EVs i.e., the specifications of plugs, socket-outlets, vehicle couplers and vehicle inlets [50].

2.4 APPLICATION OF EV CHARGING STANDARDS

Various nations adhere to various charging standards. The major contrast among these charging principles is of ports/connectors plan. To avoid the charging standards conflicts manufactures are attempting to concoct a typical charging connector contention. In the USA, SAE: J1772 connectors can be used for AC as well as DC charging ability. Tesla has manufactured its own connector that additionally upholds both AC as well as DC quick charging. Tesla additionally has planned a connector for other vehicle models, which changes over SAE: J1772 connectors to empower them by Tesla supercharging stations.

Country	AC Charging Ports	DC Charging Ports
USA	 SAE: J1772 level 1, 2 (1- ϕ)	 <ul style="list-style-type: none"> • SAE: J1772 level 1+DC • SAE: J1772 level 2+DC combo
JAPAN	 SAE: J1772 level 1, 2 (1- ϕ)	 JEVS G105-1993, CHAdeMO fast charging
EU	 <ul style="list-style-type: none"> • IEC: 62196, level 1 (1-ϕ) • IEC: 62196-2, level 2 & 3 (1 & 3-ϕ) 	 IEC: 62196-3, hybrid combo
CHINA	 IEC: 62196-2, level 2 & 3 (1 & 3- ϕ)	 GB/T: 20234.3-2011 DC fast charging
INDIA	 IEC: 60309 female connector	 GB/T: 20234.3-2011 DC fast charging

(a)

Country	AC Charging Ports	DC Charging Ports
USA	 SAE: J1772 level 1, 2 (1- ϕ)	 <ul style="list-style-type: none"> • SAE: J1772 level 1+DC • SAE: J1772 level 2+DC combo
JAPAN	 SAE: J1772 level 1, 2 (1- ϕ)	 CHAdeMO DC fast charging
EU	 <ul style="list-style-type: none"> • IEC: 62196, level 1 (1-ϕ) • IEC: 62196-2, level 2 & 3 (1 & 3-ϕ) 	 IEC: 62196-3, hybrid combo
CHINA	 IEC: 62196-2, level 2 & 3 (1 & 3- ϕ)	 GB/T: 20234.3-2011 DC fast charging
INDIA	 IEC: 60309 male connector	 GB/T: 20234.3-2011 DC fast charging

(b)

Fig. 2.2. (a) AC and DC charging ports (b) AC and DC charging connectors, followed by different countries.

A “combo,” charging connector is used in Europe. This combo has separate DC charging pins added with the existing AC chargers’ connectors. EV & charging hardware producers are attempting to homogenize the charging standards and accompany a widespread arrangement of the EV charging gadget. Fig.2.2 (a) and (b) shows charging ports and connectors respectively of various standards individually for both AC and DC charging.

2.5 OVERVIEW OF CHARGING STANDARDS IN INDIA

In India, light vehicle category of EV is widely adopted, with more modest battery pack and lower power prerequisites. As of 2017, 2-wheeler (2W) and 3-wheeler (3W) represented 99% of the aggregate EVs in India, with 3-wheeler assessing 78% (17.5 lakhs) and 2-wheeler assessing 21% (4.75 lakh). So, it is necessary to characterize the standards for category of EVs.

The connectors between EV and EVSE, particular of communication conventions and characterizing the level of voltage/current are prerequisites for standardization. India is expecting to deploying a modular charging infrastructure giving all the accessible

alternatives like Bharat chargers, CHAdeMO & CCS to EV users. Primary requirement for standardization includes defining the level of voltage/current and finding connectors between the EV and EVSE.

A committee on standardization of protocol for EV formed by the ministry of heavy industries in late 2017. On the basis of voltage and charging time, they framed draft standards for charging stations named as Bharat EV charger-AC001 (BEVC- AC001) and Bharat EV charger-DC001 (BEVC-DC001). In India, bureau of Indian standards (BIS) drafted IS:15886 for standardization of EVs and hybrid electric vehicles (HEVs) and their components.

The automotive research association of India (ARAI) also drafted some of the standards which includes automotive industry standard (AIS)-138. It is for DC charging system by existing international standards which includes IEC: 61851-1 specifies general requirements, IEC: 61851-23 is for charging station of EVs and IEC: 61851-24 is for digital communication [5]. The AIS: 102 (Part 1 and 2) and AIS: 123 include central motor vehicles rules (CMVR) type approval for HEVs. Further, AIS: 131 specifies approval procedure for EVs and HEVs presented in market for demonstration projects for government schemes.

With the type of EV (2W, 3W, 4W and buses), the design of charger depends on battery selection, system architecture and electronics for vehicle. India has adopted BEVC-AC001 (15 A, KW, IEC-60309 connector) and BEVC-DC001 (200 A, 15 KW, GB/T-20234 connector) for EVs low voltage applications. Right now, India is in the stage to characterize the standards for various, i.e., low or high, voltage applications as shown in Fig.2.3 The EV chargers demand for DC-DC converters and inverters is likely to increase in near future, going forward.

For Low Voltage EVs (2 & 3-W as well as some cars)	
Bharat EV charger AC001 for AC Charging	<ul style="list-style-type: none"> • 240V, 15A, 3.3kW, IEC60309 connector • Can deliver current at 3.3 kW to power three vehicles at a time. • Slow charging • Used by all 2W and 3W companies
Bharat EV charger DC001 for DC Charging	<ul style="list-style-type: none"> • <100V, 200A, 15kW, GB/T 20234 connector • Can deliver current at 15kW. • Fast charging. • Used by Tata Motors and Mahindra electric cars.
For High Voltage EVs (Premium cars and buses)	
Combined Charging System	<ul style="list-style-type: none"> • Combo 1 & Combo 2 connectors at up to 350 kW • High power DC charging • Can be with or without AC connector • Used by Toyota, Honda , Suzuki • Identical across the globe
CHAdeMO Standards	<ul style="list-style-type: none"> • User combination of Type 1 and Type 2 Connectors. • Power DC charging • Used by Volkswagen , Hyundai , Ford Motors , Renault , BMW , Audi , Jeep.

Fig.2.3. Public Charging Characterization of EVs in India

BEVC-AC001: - The detailed specifications of low voltage AC EV charger are shown below. These specifications apply to charge three EVs simultaneously from single phase AC supply at 230 V with maximum 15A output current and maximum 3.3 kW output power with IEC: 60309 connectors. The global reference to this standard is IS: 12360.

General Requirements

- **EVSE:** AC.
- **Energy Transfer Mode:** Conductive mode.

Input Requirements

- **Input Supply System:** AC ,3- ϕ , 5 wire system (3P+N+PE).
- **Input Voltage:** 415 V as per IS: 12360.
- **Input Frequency:** 50 Hz (\pm 1.5 Hz).
- **Failure Backup for Input Supply:** For the control system and billing unit minimum 1 hour battery backup for. During back up time in case battery drains out, data logs should be synchronized with CMS (Central management system).

Output Requirements

- **Number of Ports:** 3

- **Each Output type:** 230 V single phase, 15 A as per IS-1- 2360 AC.
- **Output Details:** Three independent charging sockets.
- **Output Current:** 15 A current each for three vehicles charging simultaneously, with IEC: 60309 connectors.

BEVC-DC001: - This standard gives all the specifications for low voltage *DC EV* charging station [6]. This *DC* charger works with 3- ϕ *AC* input voltage, 415 V. In this, the requirements of digital communication between charging station and EV for controlling the charging has also been specified. This standard is referred to the IEC: 61851 Part 1, 23 and GB/T: 20234.

General Requirements

- **EVSE:** Dual- connector DC EVSE.
- **Energy Transfer Mode:** Conductive modes.
- **Charging Mode:** 4 charging modes.
- **Reliability and Serviceability:** Modularity, fault codes, self- diagnostic features, and easy field serviceability

Input Requirements

- **Input Supply System:** AC, 3- ϕ , 5 wire system (3P+N+E).
- **Input Voltage:** 415 V as per IS:12360.
- **Input Frequency:** 50 Hz (\pm 1.5 Hz).
- **AC Connector for Supply Side:** IEC: 62196 Type 2.
- **Input Supply Failure Backup:** For control system and billing unit minimum 1 hour battery backup.

Output Requirements

- **Output Details:** Apt for 48 V and 72 V vehicle battery configuration.
- **Charger Configuration Type:**
 - Type 1: 48 V or 72 V for single vehicle charging with maximum power of 10 KW, or charging at 48 V with maximum 3.3 KW of power for 2W EV.
 - Type 2: 48 V for single vehicle charging with maximum power of 10 KW and 72 V with 15 KW power.

- **Output Current:** 200 A Max.
- **Output Connector:** 2 connectors.
- **Compatibility of Output Connector:** One connector with GB/T: 20234.3.
- **Communication System:** Controlled area network (CAN) between EV-EVSE and open charge point protocol (OCPP) between EV-CMS.
- **Converter Efficiency:** At nominal output power ($> 92\%$)
- **Power Factor:** At full load (≥ 0.90).

2.6 SAFETY CONSIDERATION OF EV CHARGING STANDARDS IN INDIA

With regards to electrical safety, the standardization of charging infrastructure stays a vital challenge in a rigorously developing global regulatory landscape. In India, some safety regulations of international and national standard are picked up by Indian agencies like AISC for featuring the need of harmonization. The *AISC* is set up by *MoRT&H* (Ministry of Road Transport & Highways) under *CMVR*-Technical Standing Committee (*TSC*). This committee review about the design, operation safety, construction, and motor vehicle's maintenance.

Under National Electric Mobility Mission Plan (NEMMP), adoption and manufacturing of EV and HEV in India scheme is introduced by Department of Heavy Industry, Govt. of India. This will need infrastructure support for AC and DC charging stations [45]. Automotive EV application involves both consumer and automotive domains for high voltage electrical safety. For drafting the new standards, some of the existing standards are considered for the electrical safety around on-board as well as off board chargers' infrastructure. Chargers, power connectors the administrative structure concerning electrical and functional safety is grounded by the IS: 13252-2010 standard alongside the two later alterations published by the BIS as shown in Fig. 2.4(a) [40].

IS: 1271-1985	• Electrical insulation classification and thermal evaluation
IS/IEC: 60309 (Part 1 and Part 2)-2002	• Plugs, socket-outlets and couplers for industrial purposes
IS: 694-1990	• PVC insulated cables for rated voltages up to and including 1100 V
IS: 11000 (Part 2/Sec 2)-2008	• Testing for fire hazard
IS: 2824-2007	• Method for determination of proof and comparative tracking indices of insulating materials
IS: 15382 (Part 1)-2003	• Insulation coordination for equipment within low voltage
IS/IEC: 60990-1999	• Touch current and protective conductor current measurement methods.

(a)

AIS: 138 (PART2)	• EV conductive AC charging system
AIS: 138 (PART2)/DF/MAY 2017	• EV conductive DC charging system
AIS: 038 (REV.1)-2015	• Electric power train vehicles construction and functional safety requirements
AIS: 049 (REV.1)	• Electric power train vehicles - CMVR type

(b)

Fig.2.4. (a) Indian electrical safety regulations based on IS: 13252-2010.

(b) Indian standard for EV safety.

Safety standards are submitted to CMVR-TSC in the form of recommendation by AISC for approval. Then AISC recommendations are considered by CMVR-TSC. It may either approve or sends the recommendations for improvements to the AISC. The

MoRT&H takes final decision after CMVR-TSC submission of proposal with the recommendations of CMVR. After getting final approval, the test agency will allotment a certificate to developer. Some of the presently appropriate safety regulations of India are shown in Fig. 2.4(b).

2.7 CONCLUSION

The most preferable EV charging standards globally like SAE, IEEE, IEC, CHAdeMO and GB/T are summarized. Further, the EV charging standards followed by India has been discussed in detail. In 2015, faster adoption and manufacturing of HEVs & EVs in India was initiated. The program aimed at promoting research, development, and demonstration of projects on EVs. The Govt. of India, ministry of heavy industries & public enterprises and department of heavy industry constituted a committee and submitted its report on 11th October 2017. The committee has recommendations in the form of specifications for AC and DC chargers namely BEVC- AC001 and BEVC-DC001 for low voltage applications. The specifications of both the chargers are also discussed. The BEVC-AC001 is specified for charging up to 3 KW using standard 15 A industrial plug. However, BEVC-AC002 will sooner be specified for on-board EV charger. In BEVC-DC001, DC chargers with output less than 100 V/15 KW is specified but BEVC-DC002 will sooner be defined for higher voltages ranges (300 V-1000 V) and high-power ratings (30 KW and more). Furthermore, for high voltage applications, currently India is following the international standards like IEC 62196-2 for AC and CCS/ ChAdeMO for DC charging. Moreover, the safety standards for EV charging in India also summarized. In India, safety regulations are taken by AISC and safety standards for conductive EV charging are based on IS: 13252-2010.

Chapter 3

SYSTEM ARCHITECTURE AND PI BASED EV CHARGER CONTROLLER

3.1 INTRODUCTION

This chapter describes the overall *EV* charger control strategies. Due to high demand of pollution free environment and limited fuel reserves, electric vehicles (*EVs*) are taken more into consideration by automotive companies. *EVs* are popular because being one of the most effective solutions to reduce reliance on oil and negligible flue gas emission. However, short driving range, battery life issues and charging are some of the major concerns in *EVs* [1].

Most important parts of *EVs* are battery and its charger [2]. Typically, there are two types of *EV* chargers i.e., on-board & off-board [3]. The off-board charger transfers higher power and charge battery pack in lesser time. For slow charging, on-board chargers are utilized. Generally, an *EV* charger has two conversion stages: *AC-DC* and *DC-DC*. The first stage is the *AC-DC* converter and is connected across grid and *DC-DC* converter in the second stage is connected across the battery pack.

As the trend of *EVs* is growing, their high penetration on power distribution grid can cause a significant issue such as: high fault current, induces harmonics, phase difference, deviation in frequency and voltage etc. *EVs* being nonlinear load for the grid, therefore difference between power generation and consumption can lead to the frequency deviation in grid. Moreover, the power converters present in *EV* for charging system can produce harmonics during operation. These emitted harmonics can cause additional power losses, device malfunction and induce instability in the system [4]. Therefore, in order to overcome the above-mentioned problems, some optimal control strategies are required to support the grid. These *EV* charger control strategies may help in maintaining grid quality and respond quickly in case of frequency deviation conditions with high accuracy. Moreover, the first stage *AC-DC* converter should be properly controlled as it is directly connected with grid and can help utility from

various issues.

In the literature, numerous types of EV charging controllers have been discussed [51]. Linear & non-linear controllers are well known among them. Sliding mode control (*SMC*) [51], feedback linearization control [52], model predictive control (*MPC*) [53], model reference control [54] and adaptive control [55] are some non-linear controllers. A high-quality current waveform and fast dynamic response may be achieved in non-linear controllers but their analysis and design are very complex [56-57]. Proportional integral (*PI*), proportional resonant (*PR*), hysteresis band (*HB*) and fuzzy logic controller (*FLC*) are some common controllers used for EV charging. Moreover, considering control accuracy, zero tracking for periodic signal can be possibly achieved in steady state using internal model principal (*IMP*) based controller [58]. Whereas, Resonant controller [59-60], Repetitive Controller (*RC*) [61-63] and hybrid controller [64] are some *IMP* based controllers designed for EV charging.

3.2 Operating Modes for EV Charger

Location (OFF board or ON board), topology (integrated or dedicated), connection type (conductive or inductive), supply type (AC or DC) and power flow direction (bidirectional or unidirectional) are all factors to consider when choosing an EV charger [65]. The operating modes of an EV charger are covered in this section. The overall construction of an on-board EV charger is shown in Fig.3.1.

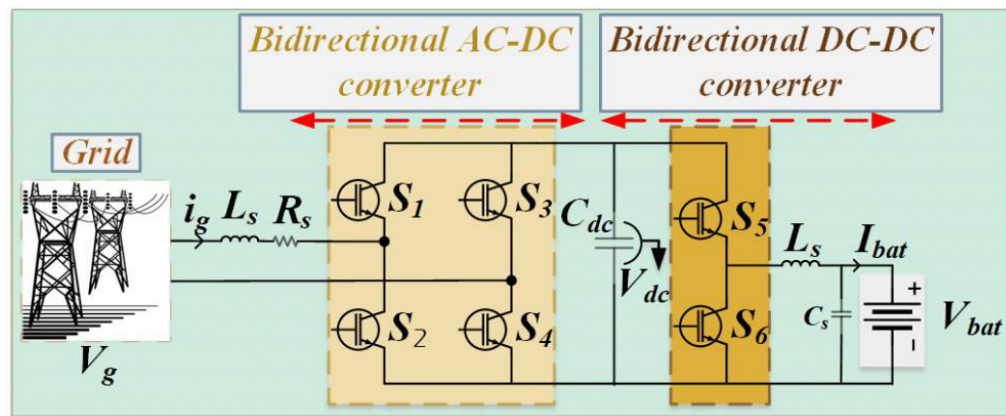


Fig.3.1 Architecture of two-stage On-board charger

The battery pack is usually charged using a two-stage on-board *EV* charger. The first step is *AC-DC* power conversion, and the second stage is *DC-DC* power conversion. Each of these stages is made up of a variety of active and passive components such as capacitors, inductors, and semiconductor devices.

On the basis of power flow. On-board charger can be divided into two types: (a) active power transfer (b) reactive power transfer. For a unidirectional charger, there is only one mode of operation i.e., active power transfer only. This indicates the charging mode or can be said grid to vehicle (*G2V*) mode only. For bidirectional type of charger, there is both active and reactive power transfer. For active power transfer, it performs grid to vehicle (*G2V*)/ vehicle to grid (*V2G*)/ discharging modes of operation. For reactive power transfer, it performs both inductive and capacitive operation.

3.2.1 Unidirectional EV Charger's Operation

Unidirectional topologies only transfer active power from the grid to the vehicle (*G2V*) with a power factor of about unity [66]. Battery charging active power command to charge the battery pack is also known as this mode. This is the most common sort of charger in today's electric vehicles, and it just enables you to regulate the active power command to charge the battery pack. The charger only operates on the right side of the x-axis of the P-Q plane, as illustrated in Fig. 3.2, since it does not enable control of reactive power.

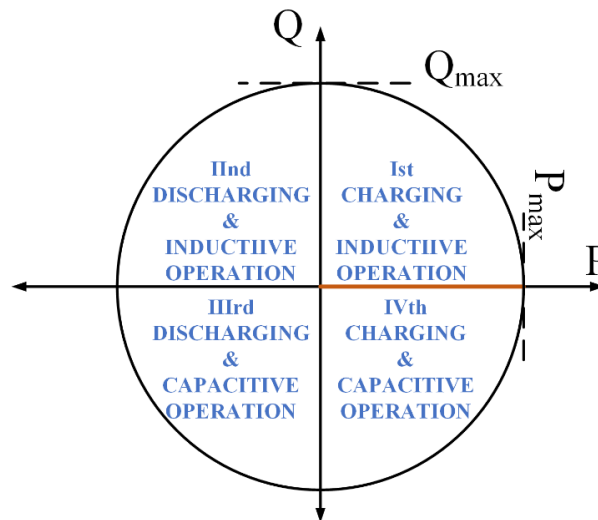


Fig.3.2. Operating mode for Unidirectional Charger

3.2.2 Bidirectional EV charger's Operation

The second sort of charger is bidirectional; it has the capacity to transmit active power in both ways, allowing it to operate in both $G2V$ and $V2G$ modes [66]. As demonstrated in Fig.3.3, it provides for the regulation of both active and reactive power. EV users can sell their battery energy to the distribution grid during peak hours or transfer it to other cars using $V2G$ technology. This process is known as vehicle-to-vehicle ($V2V$) ($V2V$). EV chargers' bi-directionality aids the grid in meeting peak load needs or providing immediate electricity during outages.

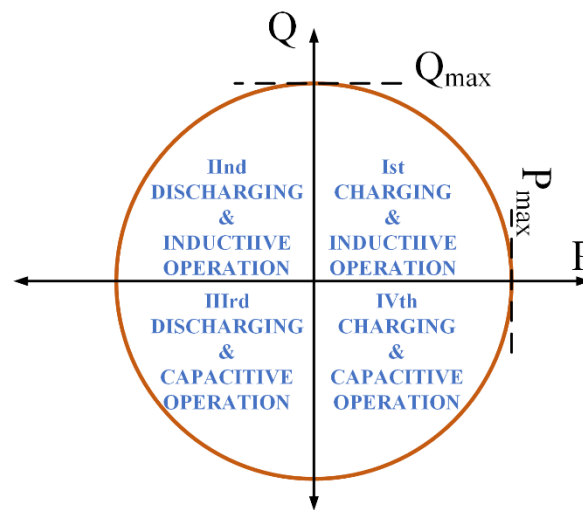


Fig.3.3. Operating mode for Bidirectional Charger

The primary goal of a bidirectional EV charger is to interchange active and reactive electricity between the grid and the automobile. As a result, the EV may contribute active electricity to the grid in the event of a sudden rise in demand, as well as absorb it if extra power is available. As a result, the huge number of EVs in the distribution network may be beneficial not just in absorbing demand-supply mismatches, but also in the wide-scale integration of intermittent renewables into the grid. Furthermore, reactive power regulation may deliver harmonic current within the charger's permitted limit. It's worth noting that only four modes of operation are accessible in four quadrant operation with active and reactive power exchange, as shown in Table V. On an active-reactive plane, Fig. 3.3 depicts the EV charger's operational modes.

Table V
 MODES OF CHARGING OPERATION

Mode	Active Power (W)	Reactive Power (VAR)	Operation	Power Factor
1	Positive	Zero	Charging	1
2	Negative	Zero	Discharging	-1
3	Zero	Positive	Inductive	0
4	Zero	Negative	Capacitive	0

3.3 Controller Design

A typical layout of a two-stage on-board electric vehicle charger is depicted in Fig.3.1.

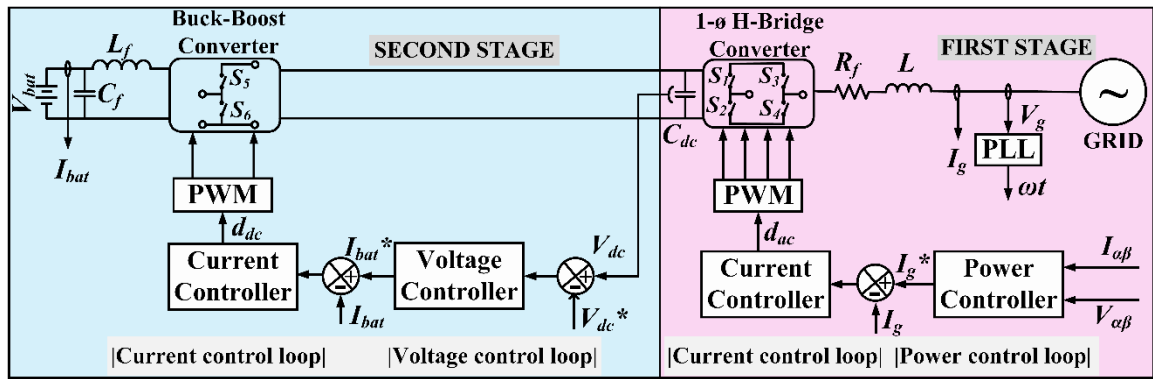


Fig.3.4 Overall Control Structure for two-stage EV charger

Fig. 3.4 depicts the on-board charger along with the overall control structure. Here, in the first stage, i.e., the AC-DC conversion stage, the converter is interfaced with the grid through the inductor (L) to minimize the ripple content in grid current, and the DC-link capacitor (C_{dc}) is connected at the second stage.

3.3.1 AC-DC Converter Control

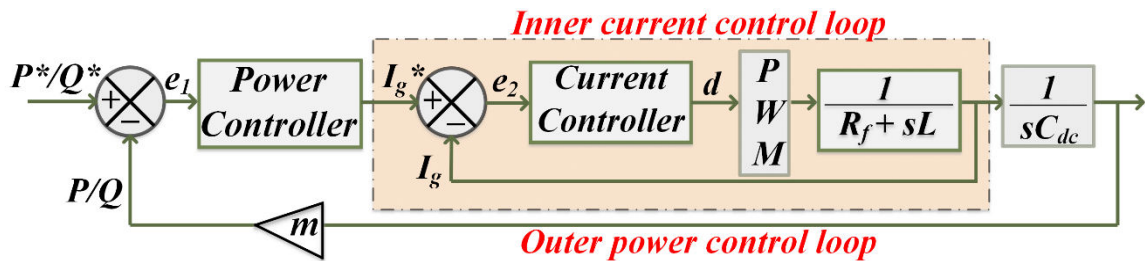


Fig.3.5. Dual-loop control for AC-DC converter

The dual-loop control structure is used for first stage converter where, the active (P)-reactive (Q) power is tracked in outer-power loop and grid side current is regulated in inner- current loop as shown in Fig.3.5 (where the m is factor of grid current, I_g). Two regular PI controllers are utilized in outer-power loop which generates the reference for inner-current loop. Further, the current reference is converted into periodic form and regulated by current controller in inner loop.

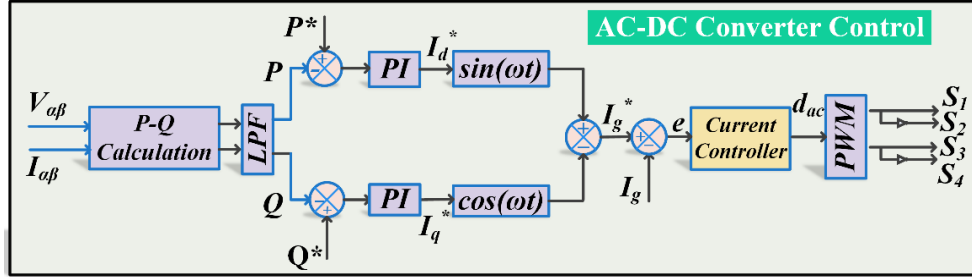


Fig.3.6. Control Architecture of AC-DC converter

The control architecture of first stage i.e., AC-DC converter has been shown in Fig.3.6. The controller performs three functions i.e., tracking of P - Q and grid current commands. The P - Q are calculated by $\alpha\beta$ quantities of grid-side current and voltage. Since, the P - Q are constant, they can be easily tracked by regular PI controllers. Therefore, two PI regulators are utilized to track P and Q 's reference commands. The PI regulators generates reference active (I_d^*) and reactive (I_q^*) current components,

$$I_d^* = K_{pd}(P^* - P) + K_{id} \int (P^* - P) dt \quad (3.1)$$

$$I_q^* = K_{pq}(Q^* - Q) + K_{iq} \int (Q^* - Q) dt \quad (3.2)$$

Here, k_{pd} , k_{id} , k_{pq} and k_{iq} are proportional and integral gains of P and Q . PI regulators. Further, the reference dq current quantity is transformed into periodic form (I_g^*) with the help of ωt generated by C .

$$I_g^* = I_d^* \sin \omega t + I_q^* \cos \omega t \quad (3.3)$$

3.3.2 DC-DC Converter Control

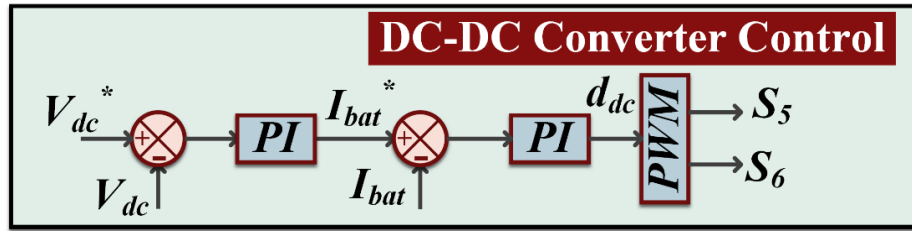


Fig.3.7. Control Architecture of DC-DC converter

Battery pack current (I_{bat}) and DC-link voltage are the values to be maintained in the EV charger's second stage (V_{dc}). Two PI regulators are used in this control arrangement. The PI controller regulates the DC link voltage in the outer loop by equating it to the appropriate reference value. The battery current is referenced and controlled in the inner control loop by this PI controller. Now, using the PWM approach [67], this inner loop controller generates the duty cycle and pulses.

$$I_{bat}^* = \left(K_{p1} + \frac{K_{i1}}{s} \right) (V_{DC}^* - V_{DC}) \quad (3.4)$$

$$d_{dc} = \left(K_{p2} + \frac{K_{i2}}{s} \right) (I_{bat}^* - I_{bat}) \quad (3.5)$$

Since, the primary focus of work focuses on the design of control structure for the inner loop control of AC-DC stage.

3.4 PI- Based EV Charger Control Structure

On- board EV charger structure has been depicted in Fig.3.5. and its controller has been illustrated in Fig.3.8. For a two-stage on-board EV charger, the controller is based on ordinary PI regulators. A completely regulated three-phase AC-DC converter is followed by a bidirectional buck boost DC-DC converter in the charger.

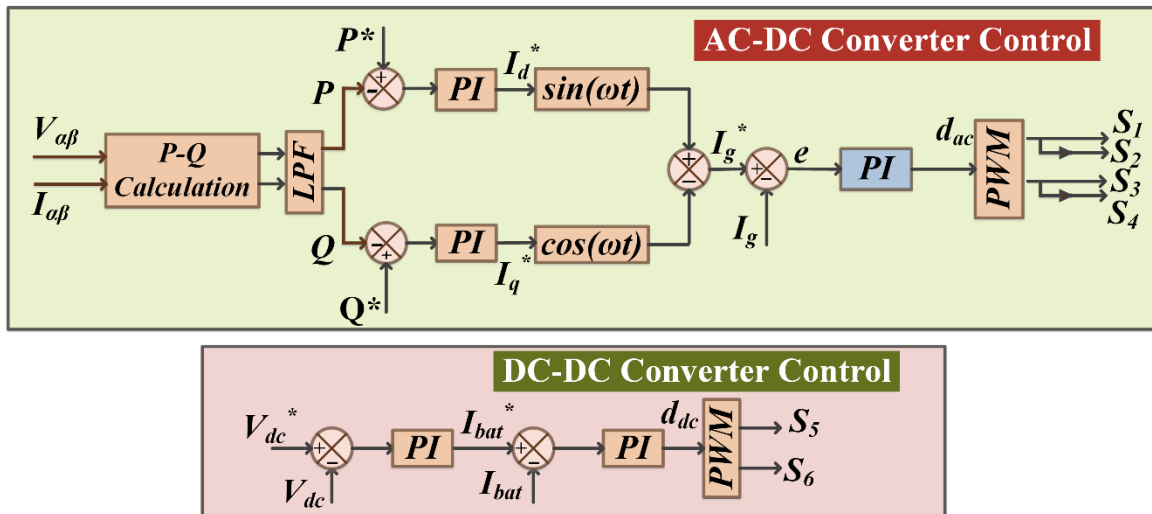


Fig.3.8 PI based control algorithm for EV charger

Both conversion stages can operate on the positive and negative sides of the $P-Q$ power plane. Five parameters are managed in the described control strategy: active-reactive power ($P-Q$), grid current (I_g), battery current (I_{bat}), and DC link voltage (V_{dc}). As a result, for each level, two distinct controllers have been incorporated. The control of an AC-DC converter consists of two loops, one for grid side current control and the other for outer (P and Q) control. Two independent PI controllers are used to control active and reactive power in the outer loop. The active (I_d^*) and reactive current component (I_q^*) references will be generated by the outputs of the outer power loop, respectively. The dq domain is used to describe these reference currents. Furthermore, two PI controllers are used to reduce the discrepancy between these two current components and the real active and reactive current components of grid current in the inner current control loop.

Two parameters, battery current (I_{bat}) and DC-link voltage, are regulated in the control architecture of the DC-DC (second stage) converter (V_{dc}). The reference DC link voltage (V_{dc}^*) is compared to the real in the outer loop, and the PI controller minimizes the error. The outer loop creates the reference battery current (I_{bat}^*), which is compared to the real battery current in the inner loop and regulated by the PI controller. In this EV charger control, a total of five values, P , Q , I_g , V_{dc} , and I_{bat} , are directed to the control.

3.5 RESULTS

The simulation and hardware results of the PI-based control architecture are presented in

this part, with simulation and hardware parameters reported in Tables VI. The *MATLAB 2020a* software is used to simulate the *EV* charger and *OPAL-RT (4510)* for controller in real time.

3.5.1 Simulation Results

A simulation scenario with various P and Q instructions has been built to claim the controller's performance, as shown in Table V. The first two modes are concerned with the charge-discharge cycle of an electric vehicle battery. In mode 1, the battery is charged at 7.2 kW and discharged at the same rate in mode 2. The next two modes demonstrate reactive power operation without the use of an electric vehicle's battery. The charger compensates the inductive reactive power and capacitive reactive power in mode-4 without exchanging power with the battery in mode-3. In the event of an on-board *EV* charger, a 400 V *DC*-link voltage reference is used, and the nominal voltage of the *EV* battery pack is set to 350 V.

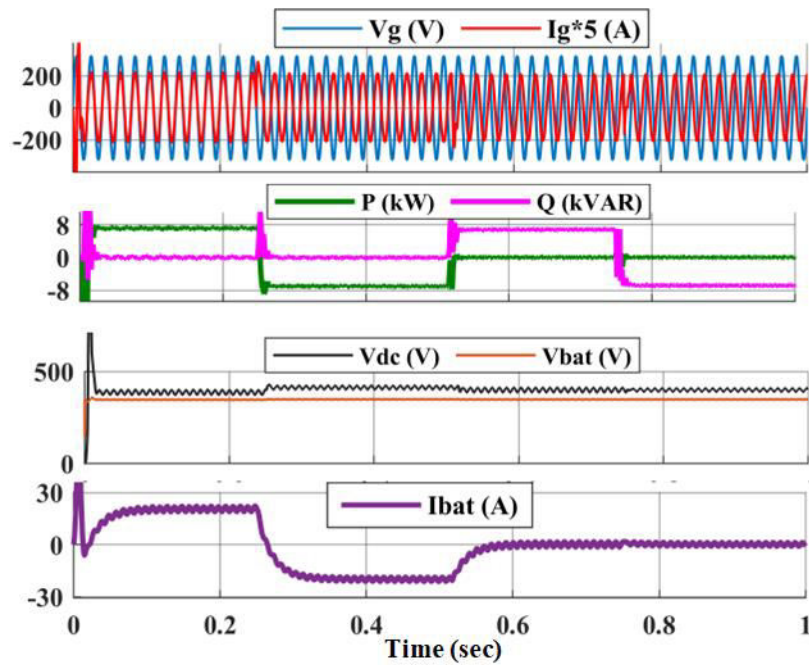


Fig.3.9. Simulation results of measured P - Q , grid current (I_g), *DC*-link voltage (V_{dc}), battery voltage (V_{bat}), battery current (I_{bat})

During all modes, the active (P)-reactive (Q) powers, grid side current (I_g), *DC*-link voltage (V_{dc}), Battery voltage (V_{bat}), and Battery current (I_{bat}) displayed in Fig 3.9. Each operational

mode takes 0.25 seconds to complete. While battery voltage is always positive, the negative value of battery current indicates charging and the positive value indicates discharge. The battery current in modes 3 and 4 is zero since there is no active power activity during these modes. Because the EV charger runs at full load for best efficiency, the grid side current remains constant throughout all modes, i.e., 30A. (rms). Throughout all operating modes, the DC connection voltage is maintained at 400 V.

Fig. 3.10 depicts the shift from one mode to another of active-reactive power and three-phase grid current with phase a voltage (for better clarification grid current is multiplied by factor of 5). The current and voltage of phase an are in phase during mode 1. Current I_g gets totally out of phase with grid voltage V_g when the charger switches from mode 1 to mode 2, as shown in Fig.3.10 (a).

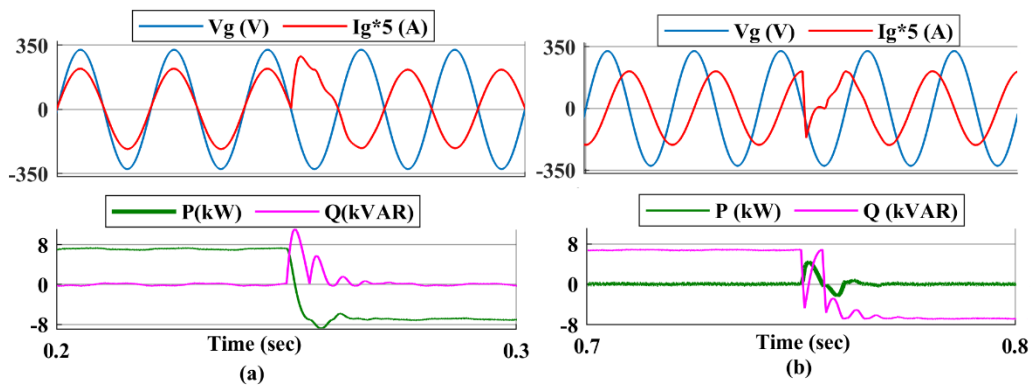


Fig.3.10 Transition of active-reactive power and grid current from (a) Mode-1 to 2, (b) Mode-3 to 4.

As demonstrated in Fig.3.10 (b), upon switching from mode 3 to 4, current I_g shifts from 90 degrees lagging behind voltage V_g to 90° leading. THD in grid current is in the permissible range in all four modes as depicted in Fig.3.11.

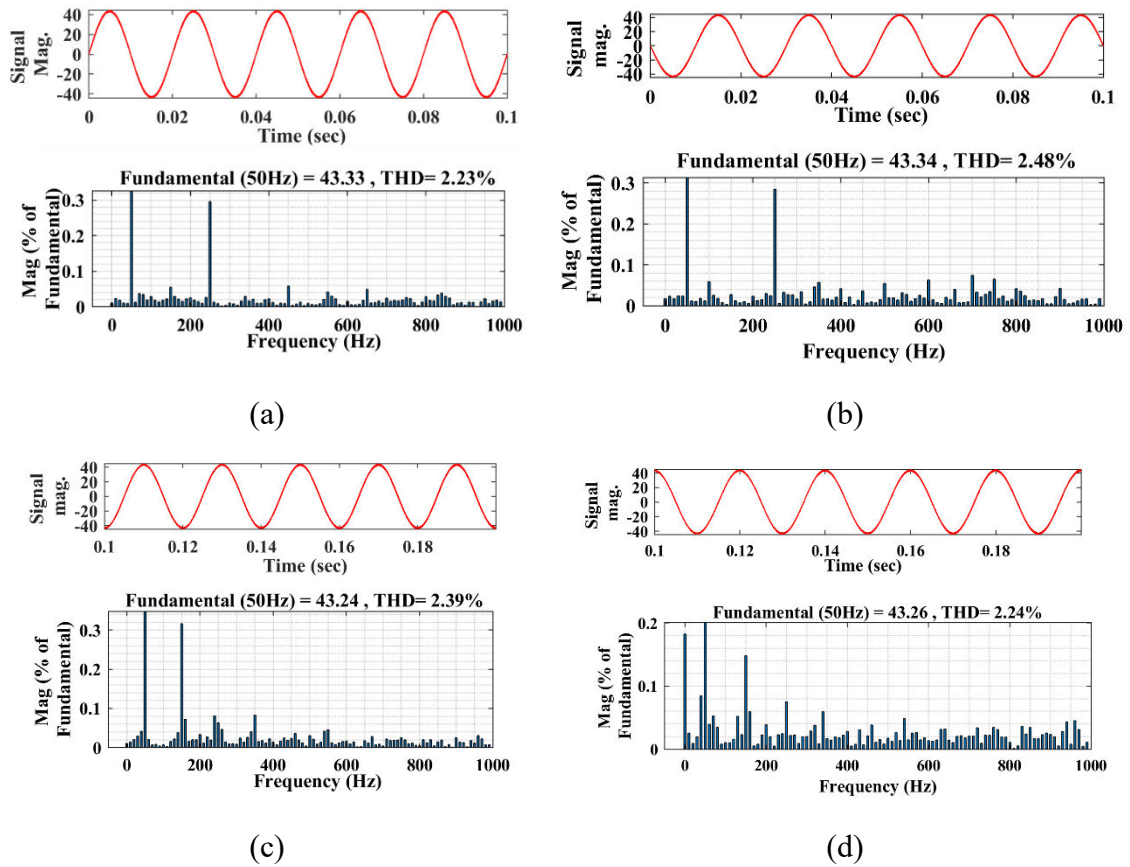
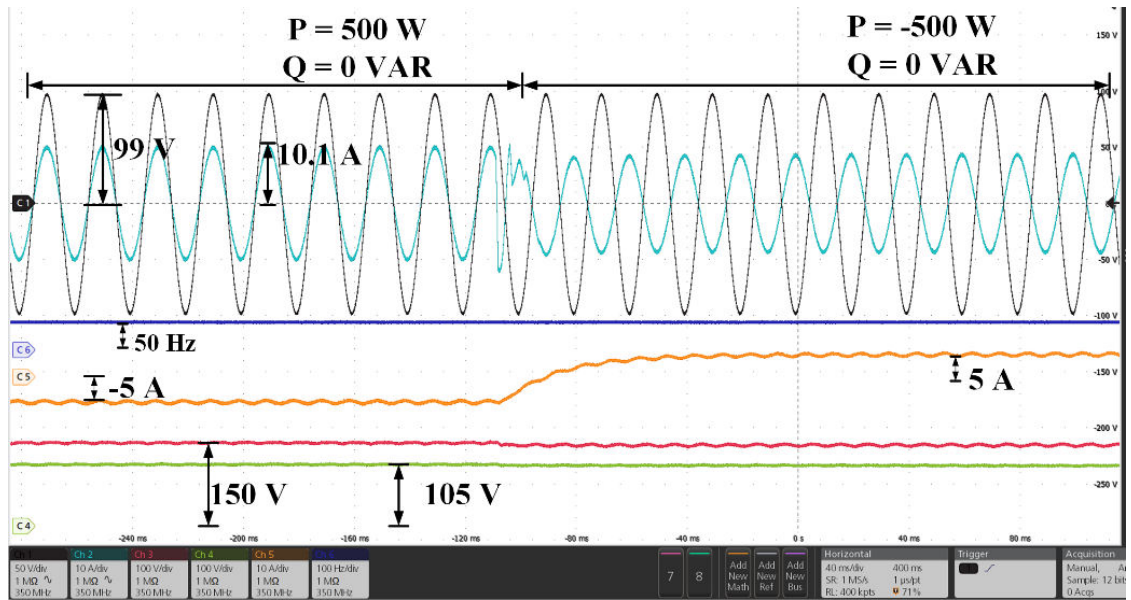


Fig.3.11. THD in grid- current (a) Mode 1 (b) Mode 2 (c) Mode 3 (d) Mode 4

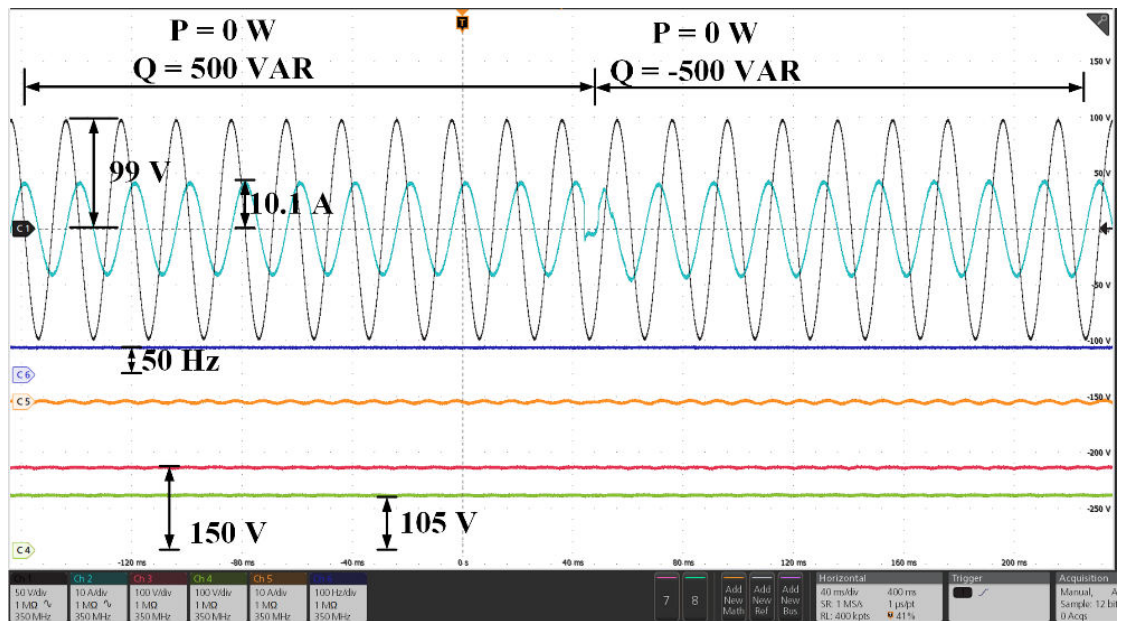
3.5.2 Experimental Results

The controller performance has been validated in laboratory using OPAL-RT (4510). The hardware prototype results of the above-mentioned controller are shown in Fig.3.1, together with the modifications stated in Table VIII. A four-mode hardware scenario identical to simulation has been built. Table IV lists the specifications for the hardware prototype, which is rated at 500 VA. Eight 12 V, 7 Ah batteries are connected in series to make a 96 V battery pack. During modes 1 and 2, the charger charges and discharges the battery pack at a rate of 500 W. The following two modes, 3 and 4, are related with reactive power operation and compensate 500 VA of inductive and capacitive reactive power, respectively.

Both converters are made up from IGBT Semikron legs, and a battery pack of 96 V has been designed by combining eight 12 V/7 Ah batteries in series.



(a)



(b)

Fig.3.12. Transition between (a) Mode 1-2, (b) Mode 3-4: grid voltage-current, DC-link voltage, and battery current, battery voltage & frequency.

The experimental results are taken on an eight-channel Tektronix mixed signal oscilloscope (series 5) with a total of eight signals: grid voltage (V_g), grid current (I_g), DC-link voltage (V_{dc}), and battery current (I_{bat}). Because the grid voltage is 70V (rms), the grid

peak voltage is roughly 98.99 V. Throughout all working modes, the full charger rating (500 VA) is used for cost-effective operation and optimal use. As a result, the EV charger's AC side current remains consistent throughout all working modes, at 7.1 A (rms).

Modes 1 and 2 depict the charging-discharging operation of the battery at the same rate, i.e., 500 W, and the transition between them is depicted in Fig. 3.12. (a). In modes 1 and 2, the phase angle is zero and 180° , respectively. Because the battery pack voltage is roughly 105 V, the battery charging current in mode 1 is $500/100 = 5$ A, and the discharging current in mode 2 is likewise the same because the discharging power command is the same as the charging active power command. In mode 3, the charger just compensates for inductive reactive power, and the grid current shifts from out of phase to 90° lagging, as illustrated in Fig. 3.12. (b). In the transition from mode-3 to 4, the phase angle changes from precisely 90° trailing to leading due to reactive power operation, as shown in Fig. 3.12.(b). As a result, during this transition, the battery current is zero.

3.6 CONCLUSION

The architecture of two-stage on board has been shown in this chapter with the detail description of the controller design. The EV charger works in 4 modes. The operating modes for unidirectional and bidirectional EV charger has been explained in detail. PI based control topologies for a two-stage off-board EV charger were given in this chapter. The first is based on a standard PI controller, while the second is based on ANFIS. Each AC-DC and DC-DC converter has its own controller in the overall EV charger controller. There are two control loops in the AC-DC converter. Four PI regulators are used in the PI-based controller, two for the outer loop and two for the inner loop. Tuning four PI regulators for a single controller, especially for inner loop, might be tricky at times. In compared to the outer loop, the inner loop is significantly faster and more difficult to adjust. The outside loop PI regulators are used to track the active/reactive power command, while the inner ones are used to track the active/reactive power command. At DC-DC stage, two PI controllers have been utilized to maintain the DC- link voltage and battery current.

Chapter 4

FUNDAMENTALS OF REPETITIVE CONTROL

4.1 INTRODUCTION

With the development of fast switching power devices, microcontrollers, digital signal processors (*DSPs*), and control strategies in the *EVs*, various control strategies have been developed such as synchronous-frame proportional integral (*PI*) [4], sliding mode control [5], predictive control [6] and hysteresis control [7]. Synchronous-frame *PI* controller is best suited for three phase converters and can only regulate sinusoidal fundamental frequency signals. The performance of a predictive controller is extremely sensitive to uncertainties and disturbances, and it is entirely reliant on an accurate model. Sliding mode and hysteresis control's erratic switching patterns can make low-pass filtering difficult and switching devices and microprocessors might be stressed.

Considering the control accuracy, by the internal model principle (*IMP*) [5], zero-tracking error of any periodic signal can be achieved, as long as generator of the reference is included in a stable closed control loop. For grid-connected inverters, many *IMP*-based controllers have been developed, including repetitive controllers (*RC*) [6-9], resonant controllers (*RES*) [10,11], and hybrid controllers [12]. Other control systems, such as those provided in [13-14], can selectively compensate the harmonic distortion by altering modulation algorithms. Internal models of desired harmonics are incorporated into the control loop of the aforementioned *IMP*-based controllers, resulting in relative precise control of periodic signals. Even with the fact that harmonic distributions are unequal, optimal harmonic mitigation by such controllers is difficult to obtain [15]. To provide high-quality feed-in current, a large number of parallel *RES* are necessary since the *RES* can only track one sinusoidal signal at a given resonance frequency [16]. Multiple resonant controllers (*MRESs*) will enhance processing burden and design complexity significantly. The conventional *RC* (*CRC*) approach, which includes internal models for all harmonics, may simultaneously eliminate all harmonics and provide a promising precise current control solution for *PWM* inverters [17]. *CRC* with the recursive form reduce design

complexity and calculation overhead when compared to *MRESs*, however they impede transient response and take up additional data memory. The odd-harmonic RC (*OHRC*) strategy has been proposed to improve the dynamic performance of *RC* systems [18], which not only boosts the error convergence rate but also utilizes less data memory than the *CRC* scheme. To improve the transient response, a series of *RC* schemes were developed by changing the internal model of *RC*, such as the $(6k \pm 1)$ order harmonic *RC* ($6k \pm 1$) scheme [19], general parallel structure *RC* scheme [20] dual-model *RC* scheme [21], and $(nk \pm m)$ order harmonic *RC* scheme [22]. The plug-in structure, constitute of a plug-in *RC* with a state-feedback controller, is used in almost all of the aforementioned *RC* schemes. The idea of *RC* is to eradicate fundamental harmonics, whilst the state feedback controller's objective is to improve *RC* systems' transient response.

4.2 RC CONTROLLER BASED EV CHARGER

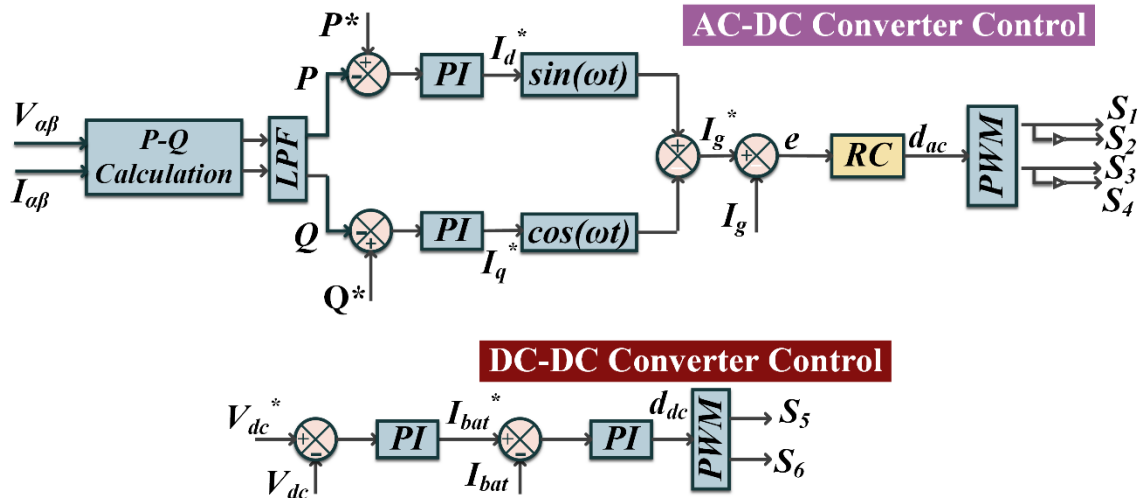


Fig.4.1 RC based control algorithm for EV charger

RC based *EV* charger for the inner loop control of the AC- DC stage has been developed in this chapter. Fig.3.1 depicts the structure of an on-board *EV* charger, whereas Fig.4.1 depicts the control architecture. The suggested charger controller comprises two control loops: the outer one controls active (P) and reactive (Q) power, while the inner one controls grid current. The P and Q can be controlled by a *PI* controller since they are constant in nature. The outer loop serves as a reference for the

inner current loop, and it is periodic in this case. The reference current is compared to the real grid current, and the PWM approach is used to create pulses for the *AC-DC* converter. The overall control strategy for the outer loop control of the *AC-DC* stage has been elaborated in Section 3.3.1. For the inner loop control of the *AC-DC* stage RC control has been employed. The regular *PI* controller has been utilized for both inner and outer loop control of the second stage i.e., *DC-DC* stage.

The main focus of this research work is on the development of the inner control for the *AC-DC* stage. So, in this chapter *RC* control has been utilized.

4.3 FUNDAMENTALS OF REPETITIVE CONTROL

4.3.1 INTERNAL MODEL PRINCIPLE

The internal model principle asserts that if an exact realisation (model) of the reference/disturbance generator is incorporated in a stable closed-loop system, the output may track/reject the reference/disturbance signal with zero steady-state error. In control theory, the realisation or model of the reference/disturbance signal is referred to as the "internal model."

An integrator can be used to model signals having a dc content. The steady-state error for constant reference and/or disturbances is virtually nil thanks to an integral action in the feedback loop. As demonstrated in Fig.4.2 [42, 66], a discrete-time integrator can be described as a unit delay with positive feedback. In other words, the integral value may be stored in only one memory location.

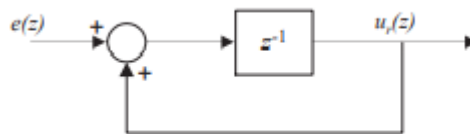


Fig.4.2. Block diagram of discrete-integrator

Additionally, periodic signals can be represented by a memory loop which thus generates an output at frequencies $k\omega$, where $k = 0, 1, 2, 3$ and ω is the periodic signal's angular frequency [42, 66]. A signal with period $T = 2\pi/\omega$ is stored in a First in First Out (*FIFO*) buffer in a memory loop. The number of memory locations required is

determined by the ratio of signal period T to sampling period T_s . For example, if the reference signal has a duration of 0.02 s (i.e., $T = 0.02\text{s}$, $f = 50\text{ Hz}$) and a sampling period of 0.1 ms ($f_s = 10\text{ kHz}$), the reference signal will need $T/T_s = 200$ memory locations. In the steady-state, no input is required to create an output with time period T if positive feedback is formed from the *FIFO* buffer's output to its input. The discrete frequency spectrum of the periodic signal at the output of the *FIFO* buffer exhibits peaks at k . Fig.4.3 shows a block design of a basic memory-loop in discrete domain with time period T . A conventional memory loop's transfer function, as shown in Fig.4.3, is:

$$\frac{U_r(z)}{e(z)} = \frac{z^{-N_0}}{1 - z^{-N_0}} \quad (4.1)$$

Where, $N_0 = T/T_s \in \mathbb{N}$.

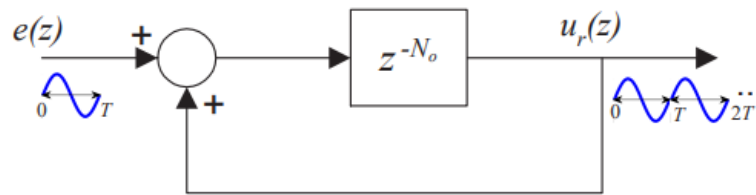


Fig.4.3 Block diagram of standard memory-loop (discrete domain).

Notice how (4.1) includes poles in the vicinity of $k2\pi/f$, where $k \in \mathbb{N}$. If the closed-loop system is stable, then there will be no tracking error.

4.3.2 REPETITIVE CONTROLLER

For periodic signals, the *CRC*, as shown in Fig.4.4, has proven to be an effective harmonic controller. The *CRC* is often used to improve control performance in terms of harmonic compensations [24], with the I_g 's total harmonic distortion (*THD*) typically being less than 5%.

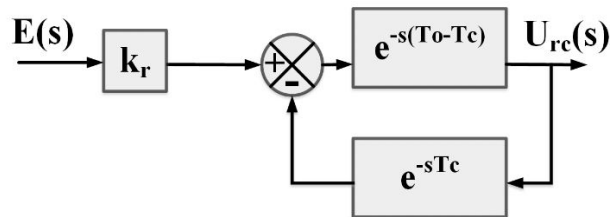


Fig.4.4. Conventional RC

The CRC can be expressed as [24],

$$G_{CRC} = \frac{U_{rc}(s)}{E(s)} = \frac{k_r \cdot e^{-sT_0}}{1 - e^{-sT_0}} \cdot e^{-sT_c} \quad (4.2)$$

The control gain is k_r , the fundamental period of the signal is $T_0 = 1/f_0 = 2\pi/\omega_0$, the fundamental angular frequency is ω_0 , and the compensation time is T_c .

It can be seen from eq. (4.2) that CRC is recursive, thus when implemented consumes a little computational effort. The G_{CRC} can further be expanded as:

$$G_{CRC} = k_r \left[-\frac{1}{2} + \frac{1}{T_0 s} + \frac{2}{T_0} \sum_{n=1}^{+\infty} \frac{s}{s^2 + (n\omega_0)^2} \right] \quad (4.3)$$

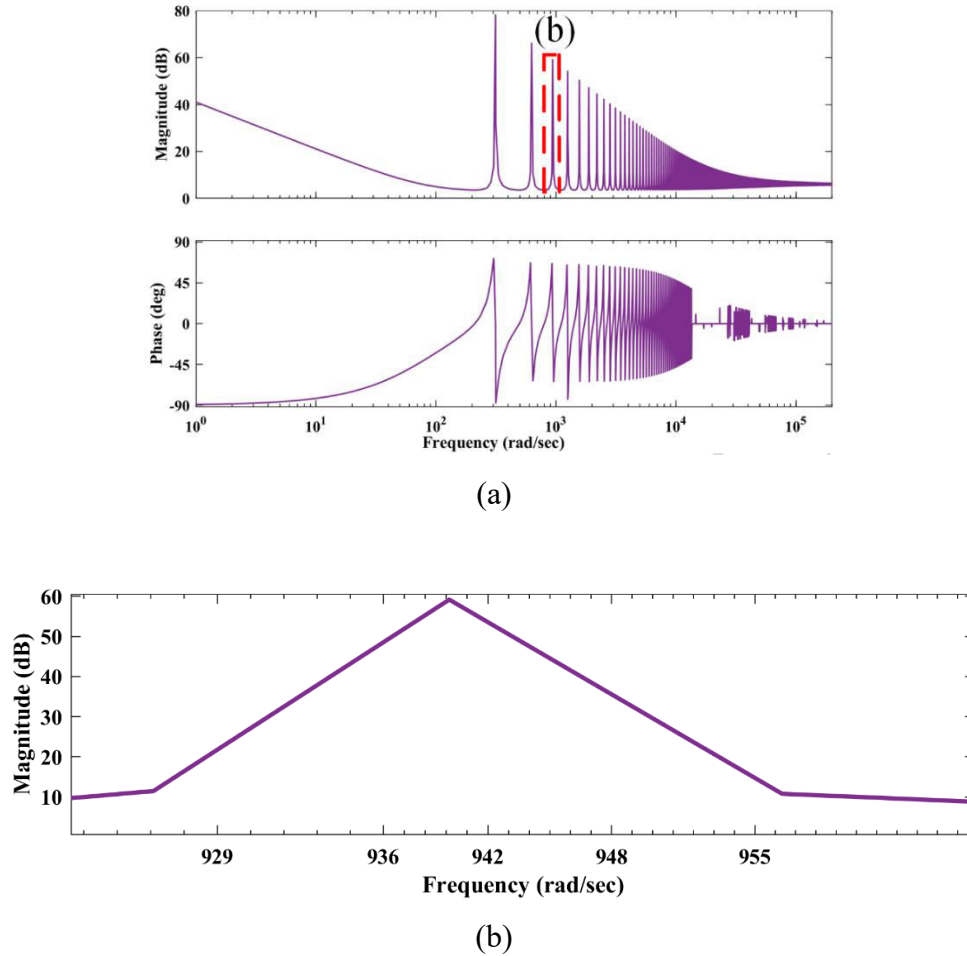


Fig.4.5. Frequency response of RC (a) within the range of angular frequency of 1 rad/sec to 10^5 rad/sec (b) frequency sensitivity illustration at 3rd harmonics

The eq. (4.3) illustrates that for all harmonic frequencies (i.e., all harmonic signals and internal model of DC), the CRC is analogous to the amalgam of proportional controller (i.e., $-k_r/2$), numerous parallel RES, and an integrator (i.e., $k_r/(sT_0)$). According to IMP , at harmonic frequencies $n\omega_0$ (including DC signal), the RES components approach infinity, and hence the CRC described in (1) can compensate for all harmonic distortions as explained in [24]. It is worthy to note that a RES with a high control gain at corresponding harmonic frequency has a fast transient response [26,27]. Since the control gains of CRC are identical for all RES controllers i.e., k_r/T_0 in eq. (4.3). Therefore, at each harmonic frequency, CRC cannot improve its transient response through setting the control gain independently. As discussed in [28-29], the CRC provides sluggish selective harmonic compensation performance. Fig.4.5 depicts the frequency response of RC . As it is clearly demonstrating that the controller has high gain at numerous fundamental frequencies, allowing it to eliminate respected associated noises.

The Repetitive controller consists of three main parts: the internal model $\left(\frac{z^{-N_0}}{1-z^{-N_0}}\right)$, (where, $N_0 = fs/f$; fs : sampling frequency and f : frequency of the signal), a phase-lead compensator, $G_c(z)$ and a low pass filter, $Q(z)$. The internal model is principally responsible for achieving zero steady-state error, while the low-pass filter improves system robustness and the compensator ensures closed-loop system stability. The literature has employed three distinct structures to implement RC (conventional RC structure, feed-forward RC structure, and plug-in RC structure). The repetitive controller is used to supplement a traditional feedback controller that already exists. The feedback controller is intended to stabilize the plant $G_p(z)$ and offer broad-spectrum disturbance attenuation.

(a) CONVENTIONAL RC STRUCTURE (CRC)

The three main parts i.e., internal model, phase-lead compensator, and low-pass filter $Q(z)$ is same for all the three structures. The only difference is in the implementation and performance (i.e., parameters values, RC gain and the stability). The entire control system is modified to incorporate RC ($G_{rc1}(z)$) in the case of CRC structure, and the RC controller adapts the instruction to a feedback control system as illustrated in Fig.4.6.

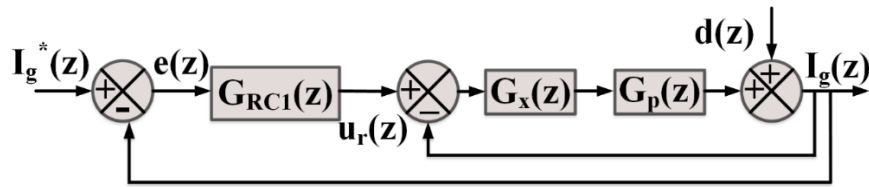


Fig.4.6 Conventional Repetitive Controller Structure

(b) FEED-FORWARD RC STRUCTURE

The entire control system has been modified to include the feed-forward command signal and the $G_{rc2}(z)$, RC controller as illustrated in Fig.4.7.

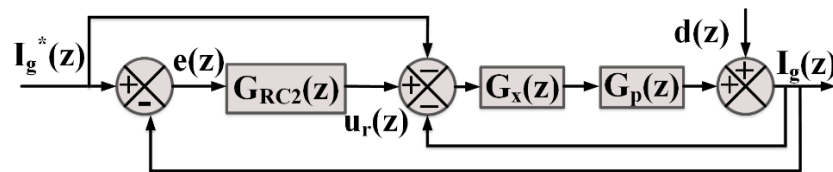


Fig. 4.7 Feed-forward Repetitive Controller Structure includes feed-forward command signal

(c) Plug-in type RC Structure

Fig.4.8 depicts the most often used plug-in repetitive control system. Plug-in RC control structures are simple to integrate into a robust, already operational closed-loop control system. Fig.4.8 depicts the RC, represented by $G_{rc3}(z)$, may be plugged in or out at any moment. When the signal input to the conventional feedback controller $G_x(z)$ is investigated, it can likewise be shown in that feed-forward and plug-in RC architectures achieve the same outcome.

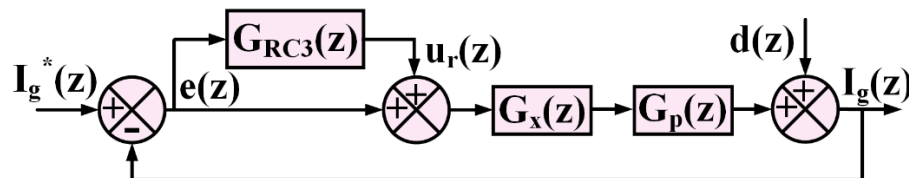


Fig.4.8 RC with plug-in structure

The discrete time RC with plug-in structure in expanded form has been shown in Fig.4.9. The three main parts has been shown here.

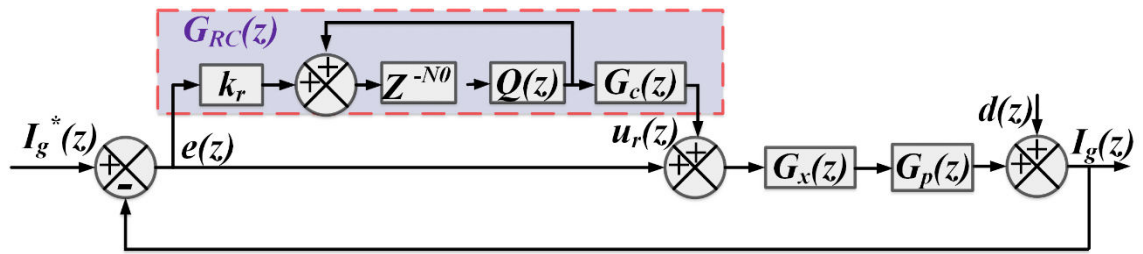


Fig.4.9. Block Diagram of discrete time RC structure

INTERNAL MODEL

The internal model's direct implementation is generally unstable. As a result, the internal model must first be stabilized. A pole-zero plots of an internal model for $N_0 = 200$ is shown in Fig.4.10. The placement of all 100 poles can be shown to be on the unity circle. As a result, the internal model is critically stable on its own, and little modifications in parameters result in unstable operations. It is frequently unstable in real applications.

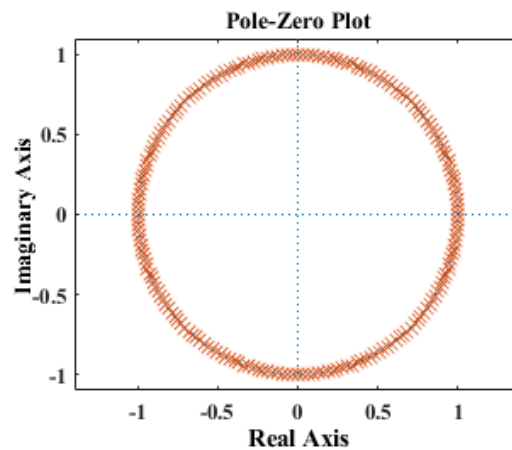


Fig.4.10: Pole zero plot of an internal model $\left(\frac{z^{-200}}{1-z^{-200}}\right)$, illustrating all the poles on the boundary of unity circle.

Various adjustments to the internal model have been proposed in the literature to stabilize it. A low-pass filter in series with the delay line z^{-N_0} is one approach to do this, but it reduces the rejection of higher-order harmonics. However, employing an internal model to stabilize the entire system (plant and controller) is unfeasible. As a result, the plant is stabilized across an extensive large frequency range using a traditional feedback controller,

represented by $G_x(z)$.

LOW-PASS FILTER

A linear phase first-order low-pass filter ($Q(z)$) of the type $\alpha_1 z^{-1} + \alpha_0 + \alpha_1 z^1$ where $2\alpha_1 + \alpha_0 = 1$ is widely used to suppress higher-order harmonics rejection and achieve internal model stability. To increase the system's stability, the low-pass filter's frequency response should be unity in the low-frequency region, where signal tracking is critical, and almost zero outside the filter's bandwidth (internal model and low-pass filter). The frequency response of different $Q(z)$ filters is shown in Fig.4.11. The obvious is that the filter's bandwidth is directly proportional to α_0 .

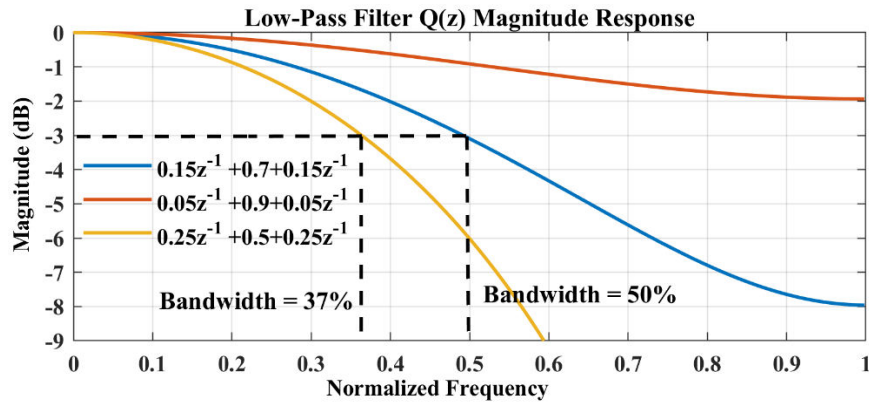
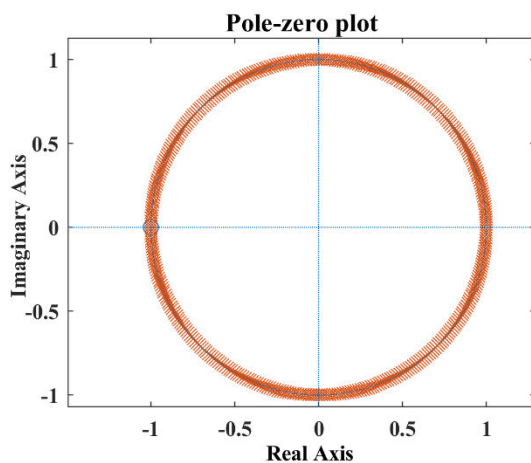
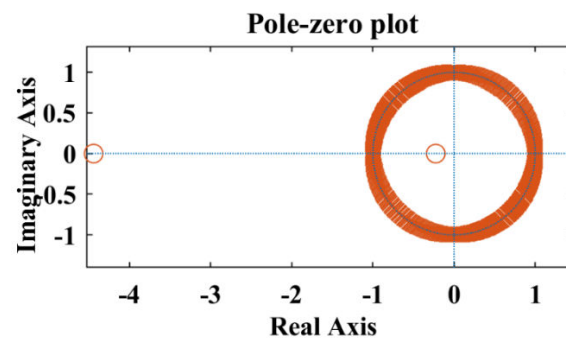


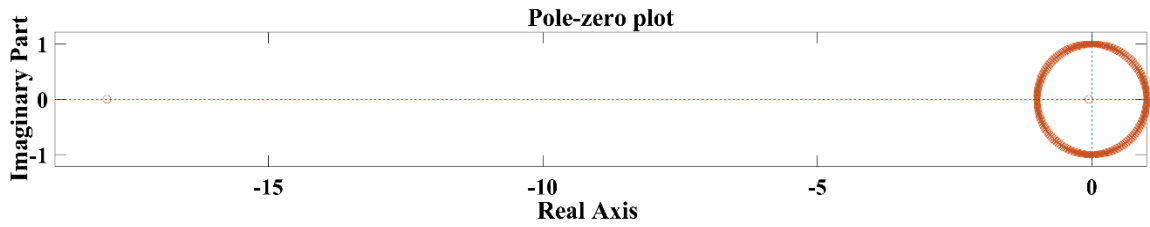
Fig.4.11. Magnitude response of different $Q(z)$; low-pass filter



(a)



(b)



(c)

Fig.4.12. Pole-zero plot of internal model $\left(\frac{z^{-400}}{1-z^{-400}}\right)$, along with different $Q(z)$ filters: (a) $Q(z) = 0.25z^{-1} + 0.5 + 0.25z^1$ (b) $Q(z) = 0.15z^{-1} + 0.7 + 0.15z^1$ (c) $Q(z) = 0.05z^{-1} + 0.9 + 0.05z^1$

Fig.4.11. depicts the pole-zero plot of internal plot of the internal model with different low-pass filters. $\left(\frac{z^{-400}}{1-z^{-400}}\right)Q(z)$ is the system shown in Fig.4.12. From Fig.4.11 and Fig.4.12, it may be deduced that a low-pass filter trades stability with higher-order harmonic rejection. The $Q(z) = 0.05z^{-1} + 0.9 + 0.05z^1$ among all the three low-pass filters which are taken into consideration has highest stability. Therefore, it brings the least stability to the overall considered system, as it can be seen that the poles of the system lies close to the boundary of unit circle.

COMPENSATOR

The zero-phase error tracking controller is implemented through the compensator $G_c(z)$. To accomplish zero phase error tracking in an RC system, $G_c(z)$ should be chosen as the inverse of the system model. However, because the plant model $G_p(z)$ comprises unmodeled dynamics and parameter uncertainties, the inverse model of the converter system is hard to construct. As a result, achieving zero phase error tracking control is difficult.

Using a lead step c as a compensator in the repeating control law, [45, 71] presented a basic phase-lead approach. Experimentation is frequently used to determine the appropriate value of lead step m . As a result, $G_c(z)$ is modelled as:

$$G_c(z) = z^c \quad (4.4)$$

A lead step c provides a phase lead in the frequency domain to compensate for phase lag, especially at high frequencies. It also can compensate for unknown time delays that

have not been predicted. A linear phase lead will result from such a lead step c .

$$\theta = c \frac{\omega}{\omega_N} 180^\circ \quad (4.5)$$

4.3.3 TRANSFER FUNCTION FOR RC CONTROLLER

Fig.4.7 depicts the overall closed loop system. The transfer function from $I_{gref}(z)$ and $d(z)$ to $I_g(z)$ is

$$\frac{I_g(z)}{I_g^*(z)} = \frac{(1 + G_{RC}(z)) + G_x(z)G_p(z)}{1 + (1 + G_{RC}(z))G_x(z)G_p(z)} \frac{\{1 - z^{-N} (Q(z)(1 - k_r G_c(z)))\} H_z(z)}{1 - z^{-N} \{Q(z)(1 - k_r G_c(z)H(z))\}} \quad (4.6)$$

$$\frac{I_g(z)}{d(z)} = \frac{(1 + G_x(z))G_p(z)^{-1} (1 - z^{-N} Q(z))}{1 - z^{-N} Q(z)(1 - k_r G_c(z)H(z))} \quad (4.7)$$

Here,

$$H(z) = \frac{G_x(z)G_p(z)}{1 + G_x(z)G_p(z)} = \frac{M(z)}{A(z)} \quad (4.8)$$

Here the known delay steps are represented by $d \in \mathbb{R}$, $A(z)$ is the system characteristic equation and all the roots lies inside the unit circle. The $M^+(z)$ & $M^-(z)$ are cancelable and non-cancelable parts of the numerator and $M(z)$, respectively. $M^-(z)$ contains roots outside or on the unit circle and have undesired roots in the unit circle, and $M^+(z)$ contains roots of $M(z)$, that are not in $M^-(z)$. The $G_c(z)$ must be an exact inverse of $H(z)$, so that zero-phase compensation may be achieved. However, due to parameter uncertainty and unmodeled system dynamics, achieving the precise inverse of the system is unachievable. Hence, $G_c(z)$ has been selected as,

$$G_c(z) = \frac{z^c A(z^{-1})M^-(z^{-1})}{M^+(z^{-1})b} \quad (4.9)$$

Here, the phase lead step i.e., $c = d$ and $b \geq \|M^-(z^{-1})\|^2$. For practical applications, the delay step can be determined by experiments.

4.3.4 STABILITY: RC SYSTEM

From the eq. (4.5) – (4.8), closed loop system illustrated in Fig.7 can be stable only if constraints mentioned subsequently are satisfied:

- (i) $H(z)$ will be asymptotically stable implies that the poles of $H(z)$ lie inside the unit circle.

$$H(z) = \frac{G_x(z)G_p(z)}{1 + G_x(z)G_p(z)}$$

As if the roots of characteristic equation of $H(z)$ i.e., $1 + G_x(z)G_p(z) = 0$ should lie inside the unit circle. This ensures that for the closed loop system consisting conventional feedback controller and plant is stable.

- (ii) For, $1 - z^{-N}\{Q(z)(1 - k_r G_c(z)H(z))\} = 0$, roots should be inside the unit circle and $Q(z)(1 - k_r G_c(z)H(z)) < 1 \forall z = e^{j\omega}$

Fig.4.5(b) depicts that, if fundamental frequency varies from 50 Hz (344 rad/sec) to 50 ± 0.2 Hz, the magnitude corresponding at the third-order harmonic frequency i.e., 942rad/sec will drop down from 52.07dB to 35.19dB. This demonstrates that fractional order harmonics are not compensated by the RC controller. Hence, we need a frequency adaptive RC scheme.

4.4 RESULTS

4.4.1 Simulation Results

AT FUNDAMENTAL FREQUENCY

The system architecture of an on-board EV charger has been modelled in the MATLAB toolbox, as shown in Fig.3.1. A two-stage 7.2kVA on-board electric vehicle charger is in the works. In Table IV, you'll find a list of simulation parameters. To test the controller's performance, a simulation with various values of P and Q was created, as given in table V. To get the most out of the EV charger, the full charger rating is utilized in all working modes. The first and second modes are used to charge and discharge batteries, respectively, while the third and fourth modes are used to rectify reactive power. If the grid requires it during modes 3 and 4, the charger can adjust reactive demand within its authorized limitations. In mode 1, the grid voltage & current being perfectly in phase when battery pack is charging from grid. However, grid side current is perfectly out of phase with voltage of grid while discharging in mode 2.

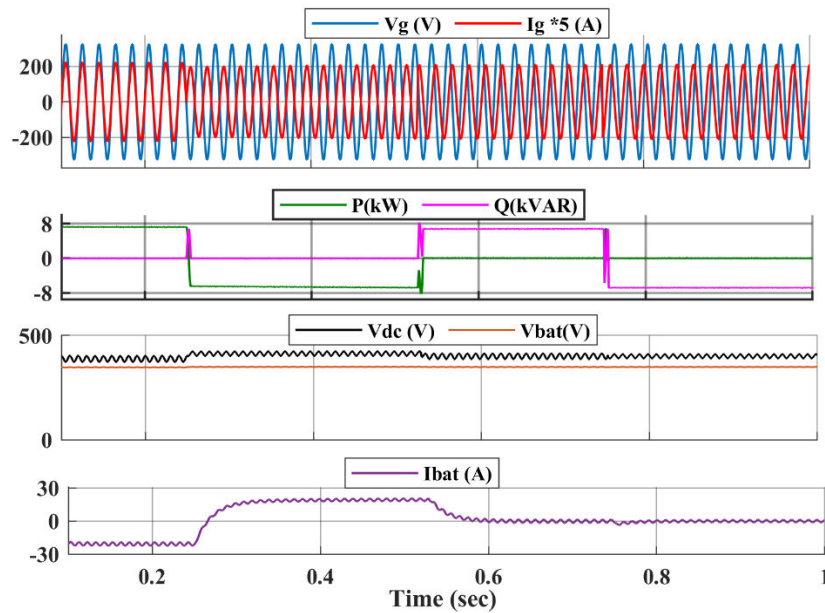


Fig.4.13 Measured grid-voltage (V_g), grid-current (I_g), active (P) - reactive (Q) power, DC-link voltage (V_{dc}), battery-voltage (V_{bat}) and battery-current (I_{bat}).

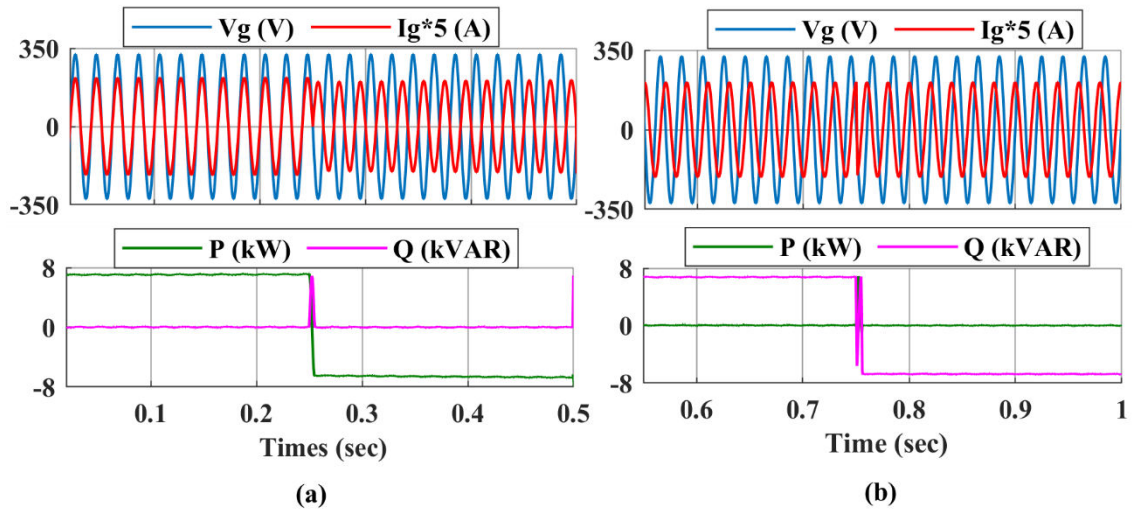


Fig.4.14 Measured grid-voltage (V_g) and grid-current (I_g) during transition from (a) Mode 1 to Mode 2 (b) Mode 3 to Mode 4

Fig. 4.14(a) depicts the shift from mode 1 to mode 2 for 0-0.5 sec. Moreover, the reactive power operation has been carried out only in modes 3 and 4. In modes 3 and 4, from 0.5-0.8 sec the current is 90° behind the voltage and 90° ahead of the voltage, respectively, as seen in Fig.4.14(b).

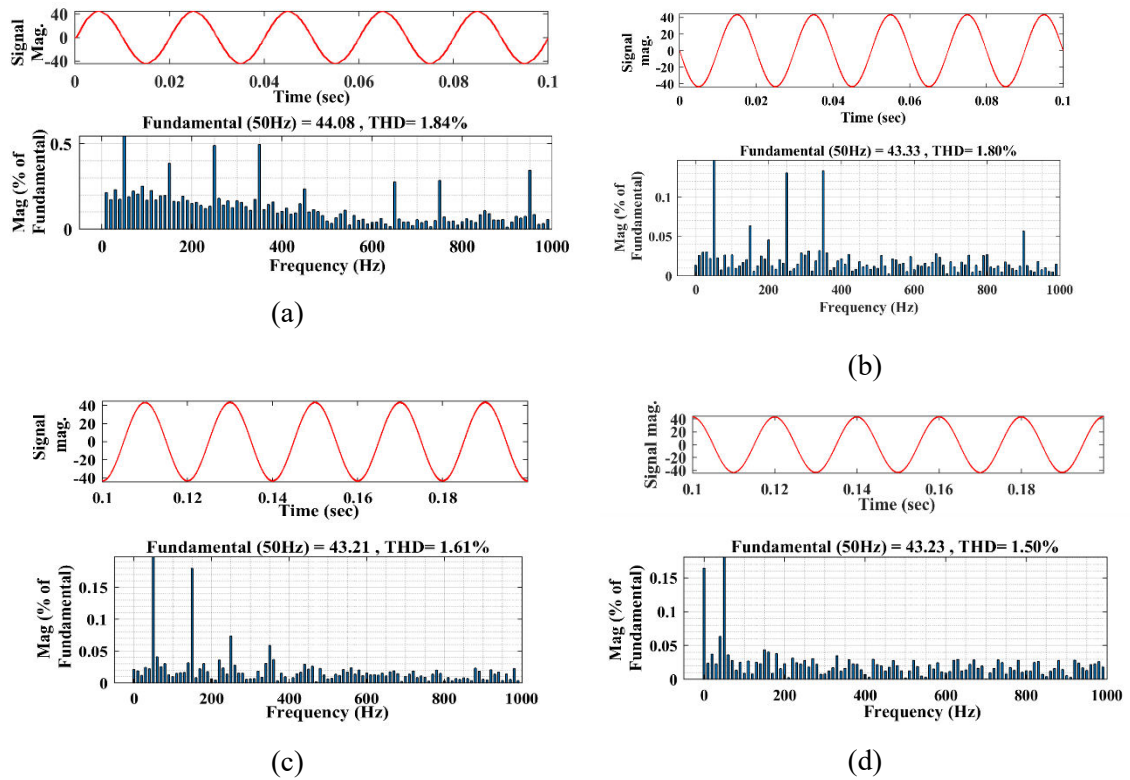


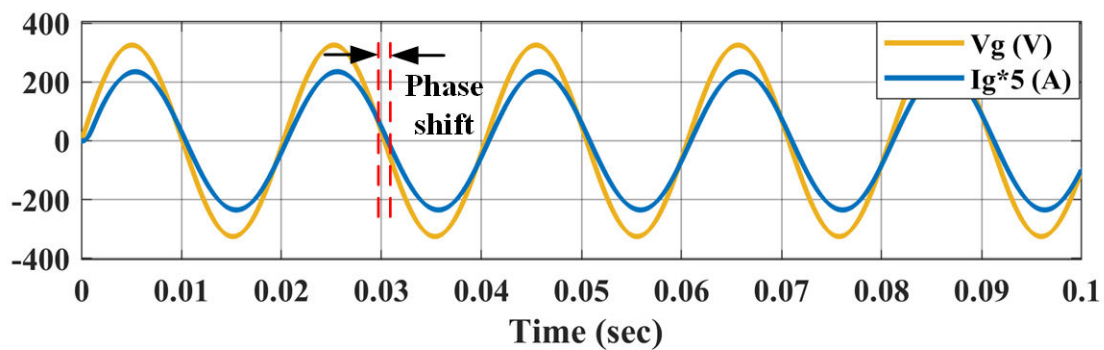
Fig.4.15 THD in I_g (a) Mode 1 (b) Mode 2 (c) Mode 3 (d) Mode 4.

UNDER VARYING GRID CONDITION

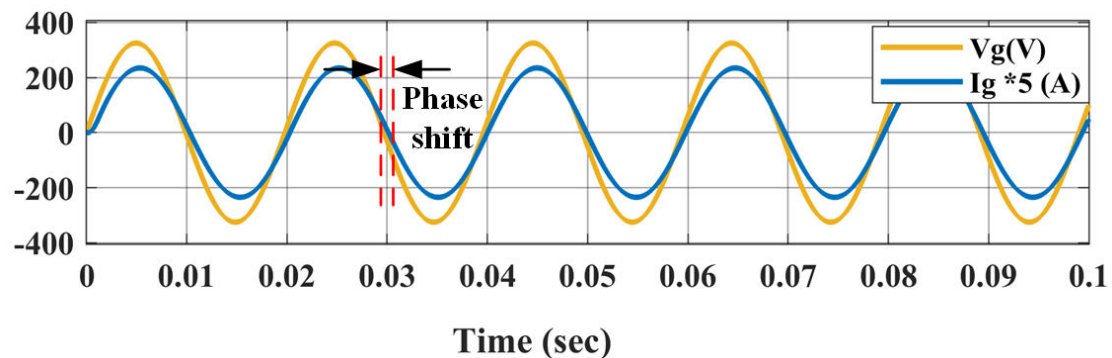
The frequency of the signal to be tracked/rejected (reference signal) must be well known and invariant for repetitive control to work. In practice, however, keeping the frequency of the reference signal constant is not always practicable. Because the EV is a non-linear demand, it will generate ongoing power system disruptions. The difference between instantaneous generation and loading plus losses leads the synchronous machine generators to speed up or slow down, resulting in frequency fluctuation. The kinetic energy of the spinning machine is used to store or extract the balance between generated and consumed power. Frequency maintaining generators detect this shift in frequency and modify their real power output to compensate for it. The magnitude of the frequency fluctuation is determined by the system's inertia and hence its size. Power electronic inverters must be able to operate correctly and fulfil performance standards (such as harmonic levels) in small networks due to the substantial variance in system frequency.

The produced dc energy is fed into the ac utility system through grid linked inverters. At the point where the inverter is linked to the utility system, the ac electric energy from the inverter must be compatible with the energy inside the ac utility system. As a result, the inverter must be able to monitor the grid's fluctuating frequency signal. An RC controlled EV charger has been developed to test the performance of repetitive control under varied frequency settings.

The controller has been tested at 49.5 Hz and 50.5 Hz in Mode 1 operation. A phase shift between the grid current and grid current has been noticed.



(a)



(b)

Fig.4.16 Phase difference between I_g and V_g due to frequency deviation (a) at 49.5Hz (b) at 50.5Hz.

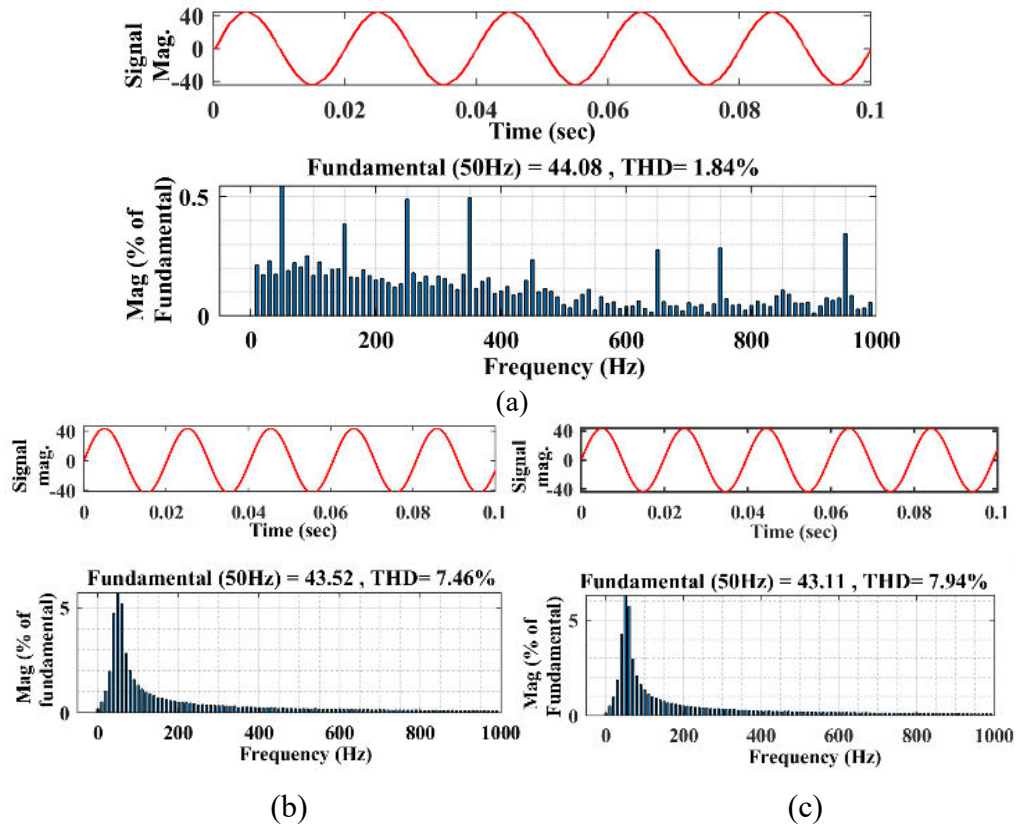


Fig.4.17. THD in grid I_g without frequency adaptability when grid frequency (a) 50 Hz (b) 49.5 Hz and (c) 50.5 Hz

THD in grid current during mode 1 under grid varying condition is shown in Fig.4.16. When the frequency of grid is exactly 50 Hz, the *THD* is 1.84% as illustrated in Fig.4.16(a). However, the *THD* rises drastically while a small change in grid frequency, as depicted in Fig.4.17 (b) & (c). The *THDs* during 49.5 Hz and 50.5 Hz grid frequencies are 7.46% and 7.94%, respectively. Furthermore, this is unacceptable since it exceeds the *THD* limit of 5% set by *IEEE-519* standard.

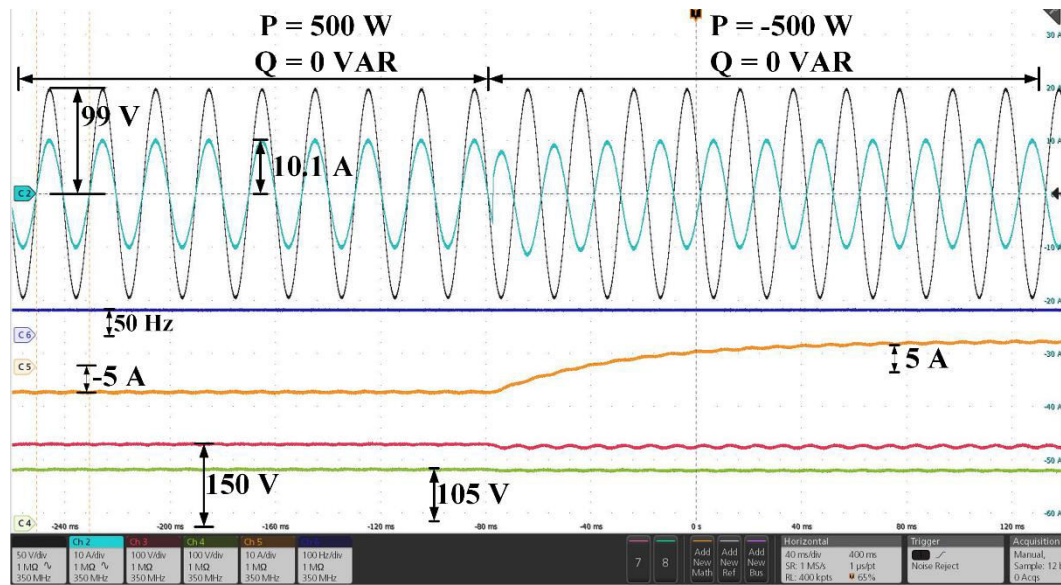
4.4.2 Experimental Results

The performance of the RC has been evaluated in a real time 500 VA experimental, setup whose detail has been shown in chapter 6. The experimental parameters are enumerated in Table IV.

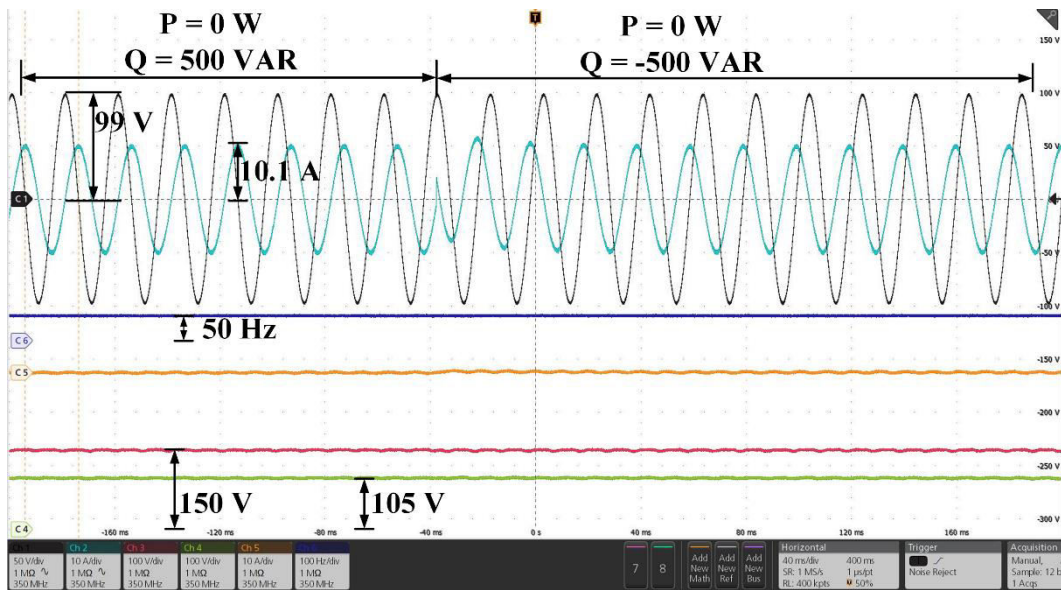
Under Fundamental Frequency

The controller's performance has also been verified in real time using four modes relating to battery charging/discharging and reactive power correction. However, in real-

time configuration, the EV charger's operational rating is limited to 500 VA in all working modes.



(a)



(b)

Fig.4.18. Transition with RC from (a) Mode 1 to 2 and (b) Mode 3 to 4.

Fig. 4.18 (a) and (b), shows the transitions from mode 1 to mode 2 & from mode 3 to mode 4 respectively. The charging and discharging of a battery pack are depicted in Fig.4.18 (a), with the battery current being negative during charging and positive during

discharging. In mode 1, the AC side current and voltage are perfectly in phase, whereas they are out of phase in mode 2. Similarly, during the changeover from mode 3 to 4, the phase difference of 90° lagging and leading, as shown in Fig.4.19 (b). Furthermore, during all four operating modes the DC-link voltage has been maintained at 150 V. THD in all four modes has been under the permissible range as shown in Fig. 4.19

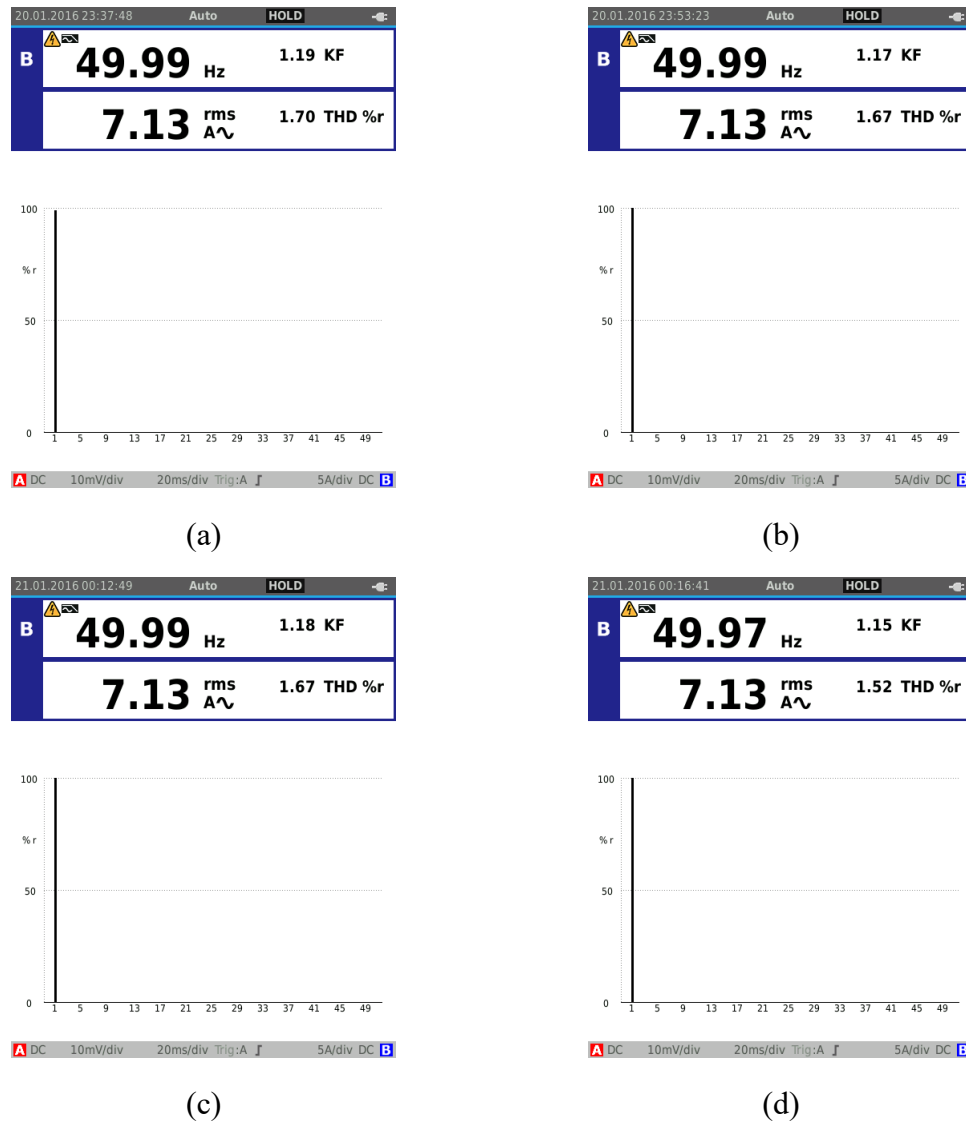
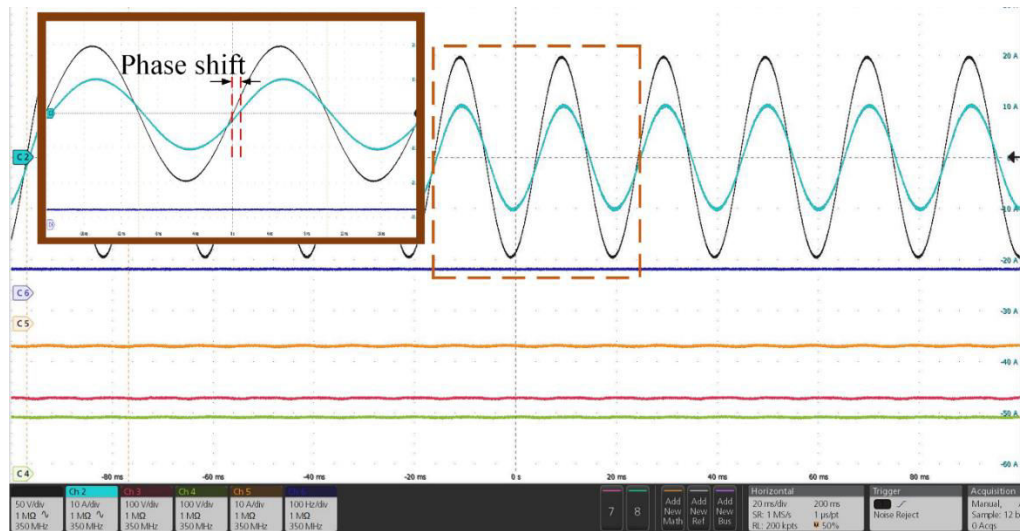


Fig.4.19. THD in I_g in all operating modes (a) Mode 1 (b) Mode 2 (c) Mode 3 (d) Mode 4

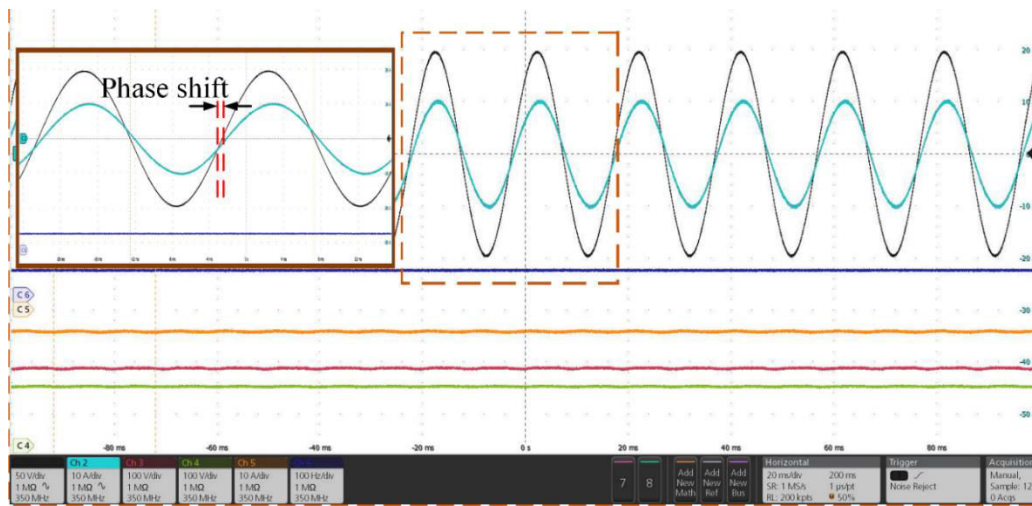
Under variable frequency Condition

RC has been tested under the grid varying conditions and evaluated during charging mode only. Fig.4.20 (a) and (b) exhibit the experimental results of an EV charger controller

under variable grid condition. When the supply frequency changed, the controller's performance deteriorated resulting in a phase shift between the grid-current & voltage, as illustrated in Fig.4.20 (a). When the AC side frequency is 50.5 Hz, as illustrated in Fig.4.20 (b), a phase shift may also be noticed. In addition, as indicated in the simulation results, changes in AC side frequency increase THD in grid current.



(a)



(b)

Fig.4.20 Phase difference between I_g and V_g due to frequency deviation (a) at 49.5Hz (b) at 50.5Hz.

4.5 CONCLUSION

This chapter introduces RC controllers and examines the performance of digital repetitive control systems with time-varying period reference signals. As RC has been employed in the inner loop of the AC- DC controller. RC controller performance has been tested using MATLAB 2020a in all the four operation modes. The influence of a changing frequency reference signal on the performance of the RC control system was demonstrated using an on-board EV charging application. This demonstrates that the CRC method performs poorly under varied frequency settings. When dealing with a changing frequency reference signal, advanced repeated control procedures are required.

Chapter 5

FRACTIONAL ORDER REPETITIVE CONTROLLER: DESIGN AND ANALYSIS

5.1 INTRODUCTION

In the previous chapter, it can be seen that the RC controller are not capable of working under grid varying conditions. The literature on frequency variations leading to a non-integer ratio (N_o) between the sampling frequency (f_s) and the fundamental frequency of the reference signal (f) can be divided into two categories: using a variable sampling time RC controller whose sampling time varies according to the reference/disturbance signal period to maintain an integer ratio N_o , and using frequency adaptive RC control schemes with fixed sampling time.

In terms of the control accuracy, by the internal model principle (*IMP*) [5], zero-tracking error of any periodic signal can be achieved as long as a reference generator is included in a stable closed control loop. For grid-connected inverters, numerous *IMP*-based controllers have been developed, including repetitive controllers (*RC*) [6-9], resonant controllers (*RES*) [10,11], and hybrid controllers [12]. Other control systems, such as those provided in [13-14], can selectively compensate for the harmonic distortion by altering modulation algorithms. Internal models of desired harmonics are incorporated into the aforementioned *IMP*-based controller's control loop, resulting in the periodic signal's precise relative control of. Even though harmonic distributions are unequal, optimal harmonic mitigation by such controllers is challenging to obtain [15]. Many parallel *RES* is necessary to provide a high-quality feed-in current since the *RES* can only track one sinusoidal signal at a given resonance frequency [16]. Multiple resonant controllers (*MRESs*) will significantly enhance the processing burden and design complexity. The conventional *RC* (*CRC*) approach, which incorporates internal models for all harmonics, may eliminate all harmonics simultaneously and provide a promising precise current-control solution for *PWM* inverters [17]. *CRC* with the recursive form reduces design complexity and calculation overhead compared to *MRESs*. However, they impede transient

response and take up additional data memory. The odd-harmonic RC (*OHRC*) strategy to improve the dynamic performance of RC systems has been proposed [18], which boosts the error convergence rate and utilizes less data memory than the *CRC* scheme. To improve the transient response, RC systems such as the $(6k \pm 1)$ order harmonic RC $(6k \pm 1)$ scheme were developed by modifying the internal model of RC. [19], general parallel structure RC scheme [20] dual-model RC scheme [21], and $(nk \pm m)$ -order harmonic RC scheme [22]. The plug-in structure constituted a plug-in RC with the state-feedback controller, which is used in almost all of the aforementioned RC schemes. The idea of RC is to eradicate fundamental harmonics, whilst the state feedback controller's objective is to advance RC systems' transient response.

All the RC, as mentioned earlier, are very sensitive to the grid frequency variations. As in most applications, RC has been implemented in the discrete domain. Considering the example of *CRC*, any periodic signal (reference signal) having an integer period of $N = f_s/f$ (f_s : sampling frequency, f : grid frequency) can be tracked. In practice, grid frequency varies within a specific range, i.e., 49 Hz to 50 Hz; considering fixed sampling rate, N may be fractional. In a digital control system with integer N , however, just delay elements may be employed. However, only delay elements in a digital control system with integer N may be implemented; hence N is frequently rounded to the nearest integer. As a result, the resonant frequency of the RC will diverge from the desired harmonic frequency. Therefore, the harmonic rejection performance of RC systems will be considerably impacted due to this variation. To improve the frequency adaptability of RC, a variable sampling rate technique is used to assure the same integer period of N under grid frequency fluctuations [23]. However, this method is seldom used as the real-time implementation and control complexity increases [24]. Therefore, a fixed sampling rate strategy has been proposed. In this, a repetitive control scheme based on a fractional delay scheme has been adopted. The Lagrange-interpolation approach is used to create a fractional delay low-pass filter. The internal model of fractional-period signals will be approximated.

The fractional delay filter is optimized in this chapter to implement adjustments to the *FORC* controller architecture. The suggested design technique includes an improved *FD* filter that delivers a unity magnitude response and a constant fractional delay across the

FD filter's bandwidth for any order ($n = 1, 2, 3$). It also explains the tools created with the goal of assessing the stability of a *FORC*-controlled system operating at a fixed sampling rate and with a variable frequency reference signal.

5.2 STATE OF ART REASEARCH

Many controllers for grid connected converters have been developed based on the Internal Model Principle (*IMP*), such as repetitive controllers [55] resonant controllers [46, 60] and hybrid controllers [49]. Because the internal model of the reference signal is incorporated in the stable closed-loop, *IMP*-based controllers provide correct control of periodic signals. However, achieving optimal harmonic mitigation remains a difficult task. Conventional *RC* methods, for example, incorporate a model of the reference signal at the fundamental frequency as well as all harmonic frequencies below the Nyquist frequency. However, because the control gain is the same at fundamental and all harmonic frequencies, these control techniques fail to suppress specific harmonic frequencies optimally. Multiple parallel structure resonant controllers (*MRSC*) and Discrete Fourier Transform based *RC* (*DFT-RC*) at specified harmonic frequencies with separate control gains offer fast transient response at the cost of high computational cost when considering the harmonic distribution.

An *IMP*-based Selective Harmonic Control (*IMP-SHC*), also known as $(n \pm km)$ -order harmonic *RC*, is utilized to avoid the significant computational load of *MRSC* and *DFT-RC*. Internal models of $(n \pm km)$ order harmonics ($m \leq n/2$ and n are the pulse number) are used to best attenuate chosen harmonics [47, 51]. Grid-connected converters have also been controlled using a dual-mode *RC* control technique, which is a specific instance of *DFT-RC*. All of these approaches, however, are susceptible to frequency fluctuations, meaning that the harmonic frequencies of the controller and reference signal do not match, resulting in more tracking error, increased *THD*, and poor performance.

The literature has studied two approaches to dealing with frequency variations: one is to utilize variable sample rates, and the other is to use *FD* filters. Variable sampling time approaches are seldom employed because of their implementation complexity, the controller's time-varying structure, and other difficulties such as stability [53, 54]. Controlling converters, shunt active power filters, and front ends with *FD* filter-based *RC* control methods has recently become popular.

5.3 REPETITIVE CONTROL SCHEMES BASED ON FRACTIONAL DELAY FILTER

5.3.1 Optimal Designing of Fractional Delay Filter

Any fractional delay z^{-N_o} may be well approximated by *FD* filters with integer delays, according to the Lagrange interpolation-based *FD* filter design. The order $N_o = f_s/f$, like *CRC*, represents *FORC*'s control resolution. Higher sampling frequencies usually imply more control precision.

The *FORC* method assumes that $z^{-N_o} = z^{-(N_i + F)}$, with $N_i = \text{int}[N_o]$ representing the integer portion of N_o and $F = N_o - N_i$, $0 < F < 1$ representing the fractional component of N_o . A Lagrange interpolation polynomial can estimate the fractional delay z^{-F} as follows [54]:

$$z^{-F} \approx \sum_{l=0}^L H_l z^{-l} \quad (5.1)$$

Here l being the degree of the polynomial and the Lagrange coefficients H_l can be calculated as:

$$H_l = \prod_{\substack{i=0 \\ i \neq l}}^L \frac{F-i}{l-i}, \quad l = 0, 1, 2, \dots, L \quad (5.2)$$

Linear interpolation between two samples is represented by the instance $n = 1$. For all frequencies, the optimal magnitude response of z^{-F} is unity. For various fractional delay values $F = 0-0.9$, Fig.5.1 demonstrates the magnitude response of first, second, and third order filter based on Lagrange-interpolation. For $n = 1$, $n = 2$, and $n = 3$, the bandwidth of (5.1) is 50%, 63%, and 75% of the Nyquist frequency, respectively, indicating that higher-order fractional delay filters provide benefit from greater and better approximation of fractional delay z^{-F} in the low frequency range.

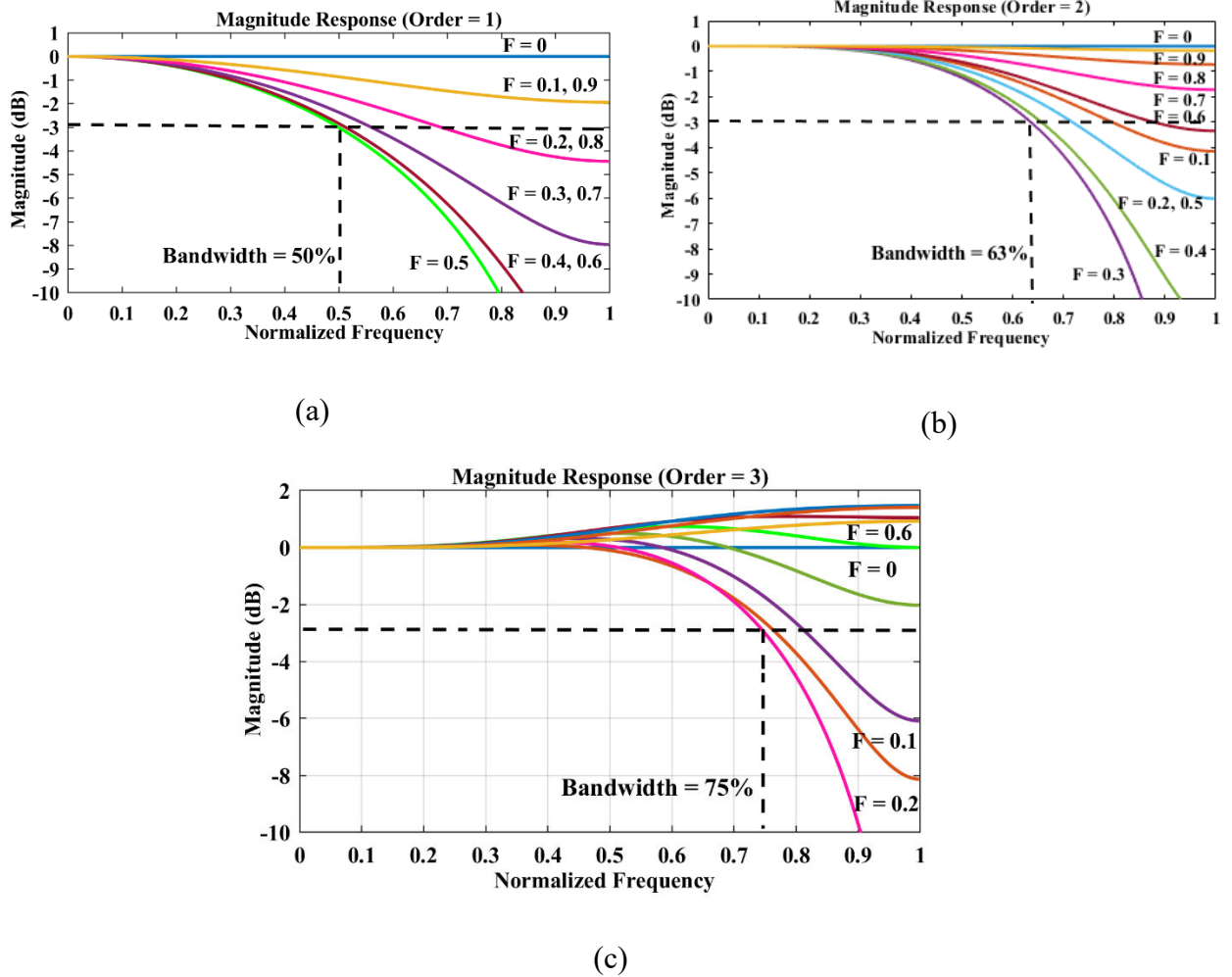


Fig.5.1. For fractional delay range ($F = 0:0.1:0.9$) magnitude response plot of Lagrange-interpolation based FD filter (a) $L = 1$ (b) $L = 2$, (c) $L = 3$

For the FD filter, its magnitude response for a wide range of frequency should possess an all-pass behavior. As per the literature, the fractional delay should be in the optimal range for good stability along with least approximation. In section 5.3.3, the effect of having non-optimal filter has been discussed. If the magnitude of FD filter is unity, then the stability of fractional order repetitive controller (FORC) also becomes easier. Fig.5.1. For fractional delay range ($F = 0:0.1:0.9$) magnitude response plot of Lagrange-interpolation based FD filter (a) $L = 1$ (b) $L = 2$, (c) $L = 3$

The design procedure for optimal designing is as follows:

- Calculate the order of FORC i.e., N_o , and $N_o = f_s/f$.

- Select order of the FD filter i.e., L . For most converter control and signal processing applications, first, second, or third order filters are generally appropriate.
- Estimate the value of F

$$F = N_0 - \left(\text{int}[N_0] - \frac{L}{2} \right), \quad \text{If } L \text{ is even} \quad (5.3)$$

$$F = N_0 - \left(\text{int}[N_0] - \frac{L}{2} \right) \quad \text{If } L \text{ is odd} \quad (5.4)$$

- Determine the necessary integer delay $N_i = N_0 - F$
- Using (5.2), determine the co-efficient of FD filter.
- Equation (5.1) can be used to implement the FD filter.

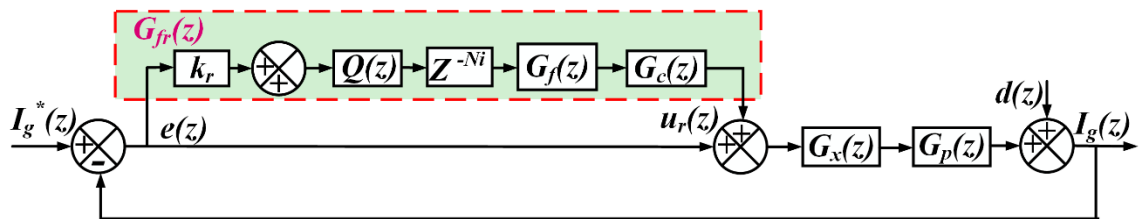
Figure 5.3 depicts the Lagrange interpolation-based FD filter construction, which may be represented as:

$$G_f(z) = H_0 + H_1 z^{-1} + H_2 z^{-2} + \dots + H_L z^{-L} = \sum_{l=0}^L H_l z^{-l} \quad (5.5)$$

5.3.2 Designing and analysis of Fractional Order Repetitive Controller

A plug-in repetitive controller has been implemented which has been discussed in the previous chapter. Under all the circumstances, in a traditional plug-in RC, the order must always be integer, i.e. N_o must always be integer. However, in fact, the grid frequency, which serves as a reference signal for grid-connected converters, fluctuates unpredictably.

In chapter 4, it has already been explained, that $N_o = f_s/f$ integer delays can be used to realize or internal model a periodic reference signal with period $T = 1/f$ at a given sampling frequency f_s . The non-integer value of N_o can be divided into the integer part i.e., N_i and the fractional part i.e., F , therefore, $z^{-N_o} = z^{-(N_i + F)}$



(a)

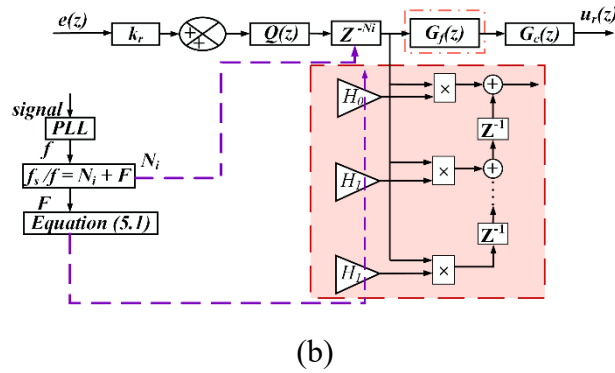


Fig.5.2 a) Fractional order repetitive control (b) Block diagram of the frequency adaptive RC.

As shown in Fig.5.2 (b), by incorporating an FD filter i.e., $G_f(z)$ inside the RC loop, along with the z^{-N_i} . The transfer function of FORC controller as shown in the Fig.5.1. is given as :

$$G_{fr}(z) = \frac{k_r Q(z) G_f(z) z^{-N_i}}{1 - k_r Q(z) G_f(z) z^{-N_i}} G_c(z) \quad (5.6)$$

Substituting (5.5) into (5.6), we get,

$$G_{fr}(z) = k_r \frac{z^{-N_i} \left(\sum_{l=0}^L H_l z^{-l} Q(z) \right)}{1 - z^{-N_i} \left(\sum_{l=0}^L H_l z^{-l} Q(z) \right)} \quad (5.7)$$

Here, H_l has been defined in (5.2). If F becomes zero, the FORC will become equivalent to the conventional RC. As a result, the FORC provides a generic method for tracking or eliminating any periodic signal with any fundamental frequency, resulting in an integer or non-integer value of N_o .

In Fig. 5.2(a), I_g can be given as

$$I_g(z) = \frac{I_g^*(z) (1 + G_{fr}(z)) G_x(z) G_p(z) + d(z)}{1 + (1 + G_{fr}(z)) G_x(z) G_p(z)} \quad (5.7)$$

From Fig.5.2 (a), transfer function from $I_g^*(z)$ and $d(z)$ to $I_g(z)$ is given as:

$$\frac{I_g(z)}{I_g^*(z)} = \frac{\left((1 + G_{fr}(z))G_x(z)G_p(z) \right)}{1 + (1 + G_{fr}(z))G_x(z)G_p(z)} \quad (5.8)$$

$$= \frac{\left\{ 1 - z^{-Ni} \left(\sum_{l=0}^L H_l z^{-l} \right) \left(Q(z)(1 - k_r G_c(z)) \right) \right\} H_z(z)}{1 - z^{-Ni} \left\{ Q(z) \left(\sum_{l=0}^L H_l z^{-l} \right) (1 - k_r G_c(z) H(z)) \right\}}$$

$$\frac{I_g(z)}{d(z)} = \frac{\left(1 + G_x(z) \right) G_p(z)^{-1} \left(1 - z^{-Ni} \left(\sum_{l=0}^L H_l z^{-l} \right) Q(z) \right)}{1 - z^{-Ni} \left(\sum_{l=0}^L H_l z^{-l} Q(z) \right) (1 - k_r G_c(z) H(z))} \quad (5.9)$$

Here,

$$H(z) = \frac{G_x(z)G_p(z)}{1 + G_x(z)G_p(z)} = \frac{z^d M^+(z^{-1})M^-(z^{-1})}{A(z)b} \quad (5.10)$$

Here the known delay steps are represented by $d \in \mathbb{R}$, $A(z^{-1})=0$ is the system characteristic equation and all the roots lies inside the unit circle. The $M^+(z)$ & $M^-(z)$ are cancelable and non-cancelable parts of the numerator and $M(z)$, respectively.

So, the $G_c(z)$ has been chosen in a way to achieve zero-phase compensation

$$G_c(z) = \frac{z^d A(z^{-1})M^-(z^{-1})}{M^+(z^{-1})b} \quad (5.11)$$

Here $b \geq \|M^-(z^{-1})\|^2$. In practical applications, d has been determined by experiments.

5.3.3 FORC: Stability Criteria

There are several approaches for examining a system's stability, but FORC pushes each approach to its limit due to its high degree of polynomial equation. Calculating the pole locations, for example, is the most frequent way for stability studies, but FORC has a very high N_0 value (200 when $f = 50$ Hz and $f_s = 10$ k Hz), making root-finding extremely difficult for any root-finding algorithm. Using the classic Nyquist stability criteria (5.7) – (5.11), the entire closed-loop system may be determined to be stable if the following two requirements are met:

1. The closed-loop system $H(z)$ (provided in (5.10)) is asymptotically stable without the FORC controller. That is, the roots of $1 + G_x(z)G_p(z) = 0$ are contained within the unit circle.
2. The roots of $1 - z^{-Ni} \left\{ Q(z) \left(\sum_{l=0}^L H_l z^{-l} \right) (1 - k_r G_c(z) H(z)) \right\} = 0$ should lie

inside the unit circle

$$\text{Therefore, } |Q(z)| \left| \sum_{l=0}^L H_l z^{-l} \right| \left| (1 - k_r G_c(z) H(z)) \right| < 1 \quad \forall z = e^{j\omega} \quad (5.12)$$

In real applications, both N_i and F change slowly with grid frequency variation; nevertheless, because N_i can only have an integer number, the magnitude response of z^{-N_i} is always unity for all frequencies. If the value of F is within the ideal fractional delay range of the FD filter, proper division of N_o into its two components (N_i and F) ensures that the magnitude response of the FD filter is always unity within the bandwidth of the filter. In real applications, if the proposed FD filter's bandwidth is greater than the bandwidth of the low pass filter $Q(z)$, then

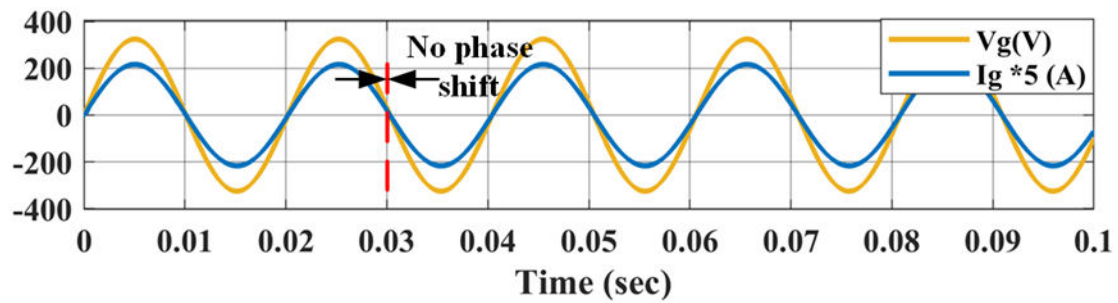
$$\left| \sum_{l=0}^L H_l z^{-l} \right| \rightarrow 1 \quad \& \quad |Q(z)| \rightarrow 1$$

within the pass band of $Q(z)$. The initial stability requirement of *FORC* systems is identical to that of *CRC* systems, and the stability criteria of (5.12) for *FORC* systems becomes similar to that of *CRC* systems inside the pass band of $Q(z)$. The stability range for the *FORC* gain is $0 < k_r < 2$ when $G_c(z)$ of (5.11) is used to accomplish zero-phase compensation. It is evident that *FORC* systems may be synthesized in a similar way to well-known *CRC* systems.

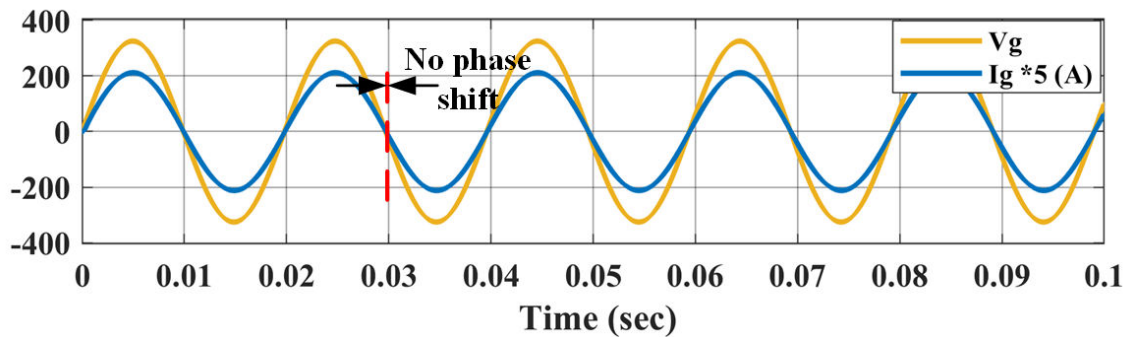
5.4 RESULTS

5.4.1 SIMULATION RESULTS

As discussed in chapter 4, the performance of the RC system has been deteriorates under varying grid frequency. But using the LaGrange interpolation-based FD filter, it has been overcome. The results have been validated under variable grid frequency. It has been depicted in Fig.5.3 (a) during the charging i.e., Mode 1, under 49.5 Hz and 50.5 Hz, no phase shift can be seen between the grid current and the grid voltage. *THD* in grid current during mode 1 using frequency adaptability approach has depicted in Fig.5.4. The grid-current's *THD* is in the allowable limit and does not change considerably when the frequency. With 49.5 Hz and 50.5 Hz, grid frequencies, *THD* being 1.86% and 1.99%, respectively



(a)



(b)

Fig.5.3. No phase difference between I_g and V_g with frequency adaptability due to frequency deviation (a) at 49.5Hz (b) at 50.5Hz.

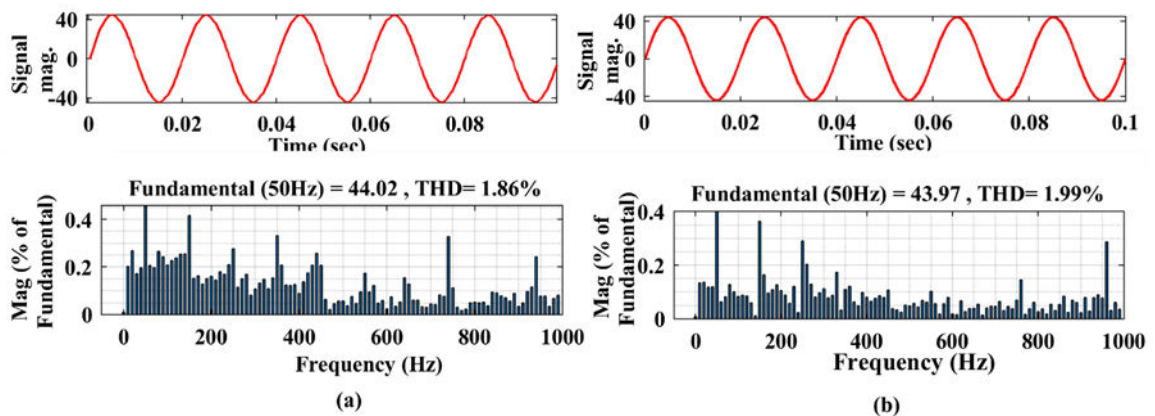
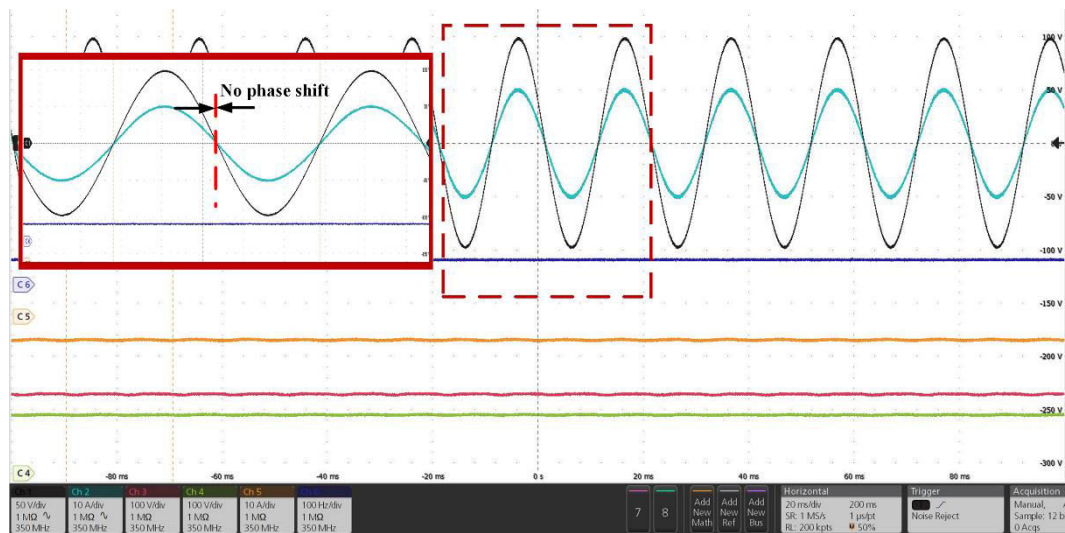


Fig.5.4. THD in grid I_g with frequency adaptability when grid frequency (a) 49.5 Hz and (b) 50.5 Hz.

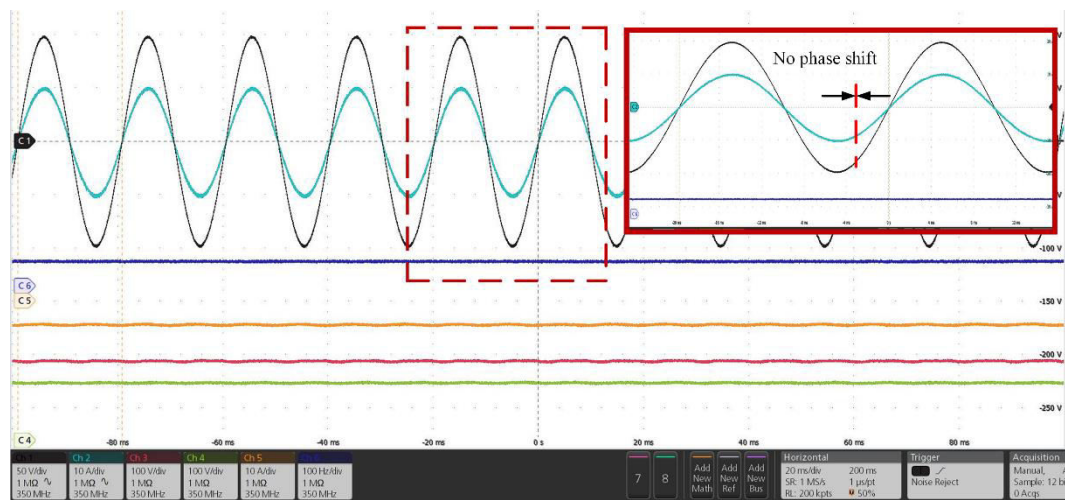
5.4.2 EXPERIMENTAL RESULTS

RC system with frequency adaptability scheme has been examined in real time using OPAL-RT (4510). The parameters have been enumerated in Table IV. When the supply

frequency changed, the controller's performance deteriorated resulting in a phase shift between the grid-current & voltage, as illustrated in Fig.5.5 (a). When the AC side frequency is 50.5 Hz, as illustrated in Fig.5.5(b), a phase shift may also be noticed. In addition, as indicated in the simulation results, changes in AC side frequency increase THD in grid current.



(a)



(b)

Fig.5.5. Steady-state performance of the frequency adaptive RC controller at (a) 49.5 Hz

(b) 50.5 Hz

5.5 CONCLUSION

This chapter outlines a method for designing and analyzing a FORC control scheme that uses a constant sample rate to adjust for periodic signals of varying frequency. A design improvement has been presented, as well as stability criteria for the proposed FORC systems. A well-designed FORC control system is totally compatible with a CRC system, according to extensive experimental data. It also demonstrates that, in the presence of frequency changes, the sampling frequency has no substantial influence on the tracking error performance of the FORC controller, but the performance of the CRC controller is very sensitive to sample frequencies. In general, the suggested FORC approach provides a simple, efficient, and high-performance real-time control solution for power converters dealing with periodic signals of variable fundamental frequency.

Chapter 6

RESULTS: SIMULATION AND EXPERIMENTAL

6.1 SIMULATION RESULTS

In the MATLAB toolbox, the system architecture, as illustrated in Fig.3.1, of an on-board EV charger has been simulated. A two-stage 7.2kVA on-board EV charger is being developed. The simulation parameters have been enumerated in Table II. A simulation with varied values of P and Q was developed to validate the controller's performance, as shown in table III. During all operating modes, the complete charger rating is used to get the most out of EV charger. The first and second modes are for charging and discharging of batteries, respectively, while the latter two modes just indicate reactive power correction. During mode 3 and 4, if the grid requests, the charger can compensate reactive demand within its permissible limits.

Table VI
System Parameters

PARAMETERS	SYMBOL	Simulation	Experimental
Grid Voltage	V_g	230 V	70 V
Grid Frequency	f	50 Hz	50 Hz
Switching frequency	f_s	20 kHz	20 kHz
DC link Capacitor	C_{dc}	330 μ F	330 μ F
Line Inductor	L	1 mH	2.5 mH
Battery Voltage	V_{bat}	350 V	96V
DC link voltage	V_{dc}	400 V	150 V
DC-DC Converter Inductor	L_f	2 mH	4mH
DC-DC Converter Capacitor	C_f	330 μ F	47 μ F

For all four modes of operation, voltage of the grid (V_g), current in the grid (I_g), measured

active (P) and reactive (Q) power, dc-link voltage (V_{dc}), battery voltage (V_{bat}), and battery current (I_{bat}) as depicted in Fig. 6.1. The I_{bat} is negative during charging and positive while discharging. During modes 3 and 4, the I_{bat} is zero, indicating that no active power operation has been performed. In all four operating modes, V_{dc} has been maintained at 400 V.

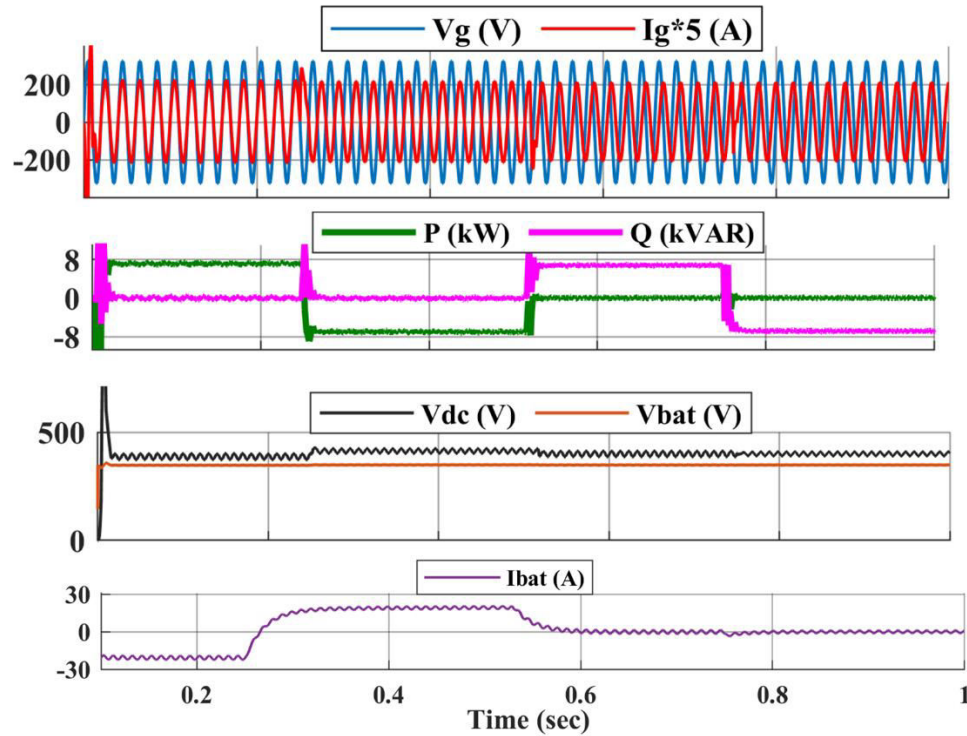


Fig.6.1. Measured grid-voltage (V_g), grid-current (I_g), active (P) - reactive (Q) power, DC-link voltage (V_{dc}), battery-voltage (V_{bat}) and battery-current (I_{bat}) using RC.

TABLE VII

Modes of Operation

Mode	P(kW)	Q(kVAR)	S (kVA)	Time(sec)
1	7.2	0	7.2	0 - 0.25
2	-7.2	0	7.2	0.25 - 0.5
3	0	7.2	7.2	0.5 - 0.75
4	0	-7.2	7.2	0.75 - 1

In mode 1, the grid voltage & current being perfectly in phase when battery pack is charging from grid. However, grid side current is perfectly out of phase with grid voltage while discharging in mode 2. Fig.6.2(a) depicts the shift from mode 1 to mode 2 using RC control approach. Moreover, only in modes 3 and 4, reactive power operation has been performed. In modes 3 and 4, the current is 90° behind the voltage and 90° ahead of the voltage, respectively, as seen in Fig.6.2(b).

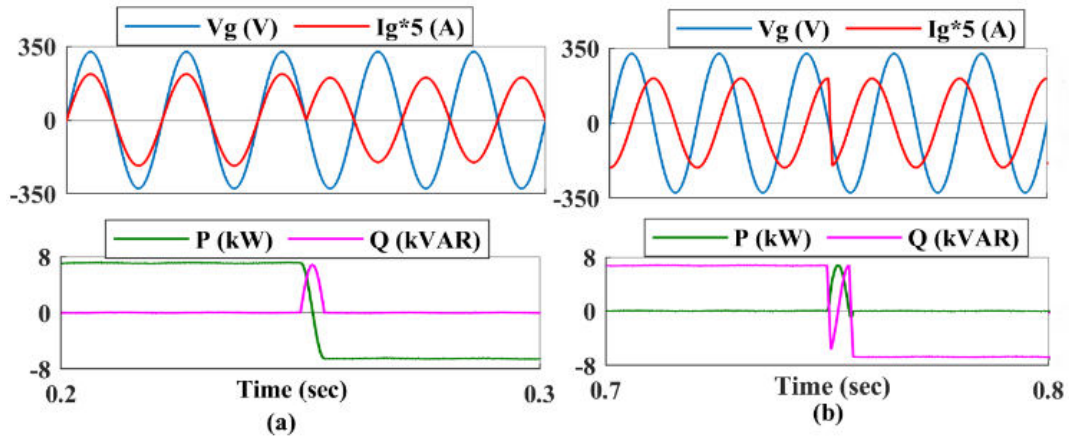


Fig.6.2. Measured grid-voltage (V_g) and grid-current (I_g) during transition using from (a) Mode 1 to Mode 2 (b) Mode 3 to Mode 4

Fig. 6.2(a) shows the transition from mode 1 to 2 using RC control scheme in the inner loop of AC-DC converter. Fig.6.3 shows the same operation for EV charging infrastructure using PI based controller. On comparing Fig.6.2(a) and Fig.6.3 it can be clearly concluded that transition from mode 1 to 2 using RC controller. It can be clearly seen in Fig.6.2(a) that with RC controller the transition is smooth and gives no overshoot, but there is an overshoot in grid current with regular PI controller and takes more time to settle.

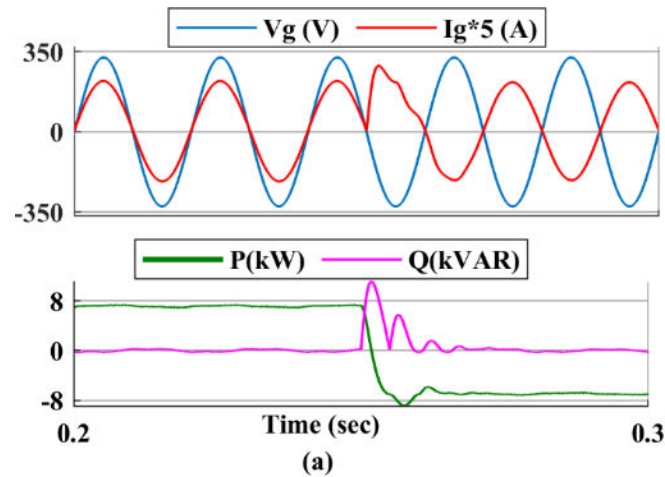


Fig.6.3 Transition from mode 1 to 2 with RC controller

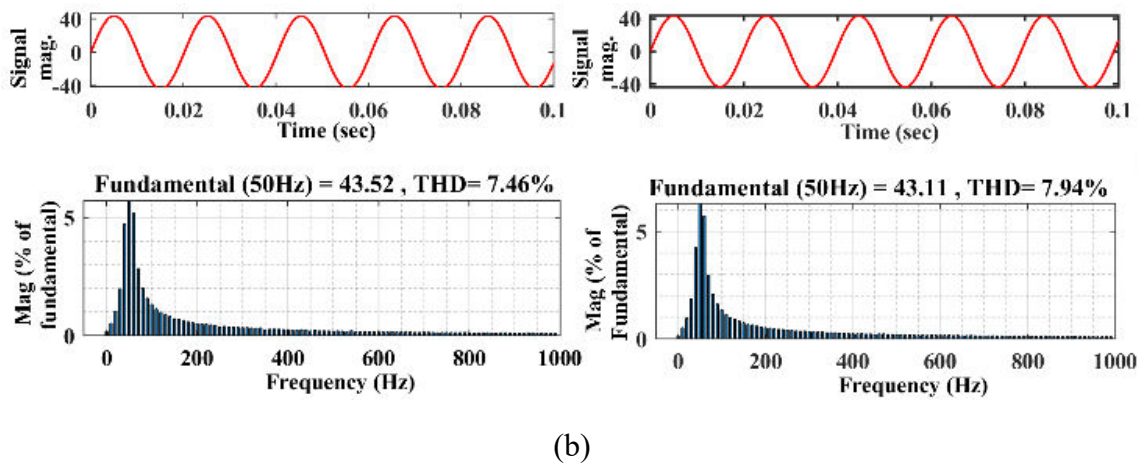
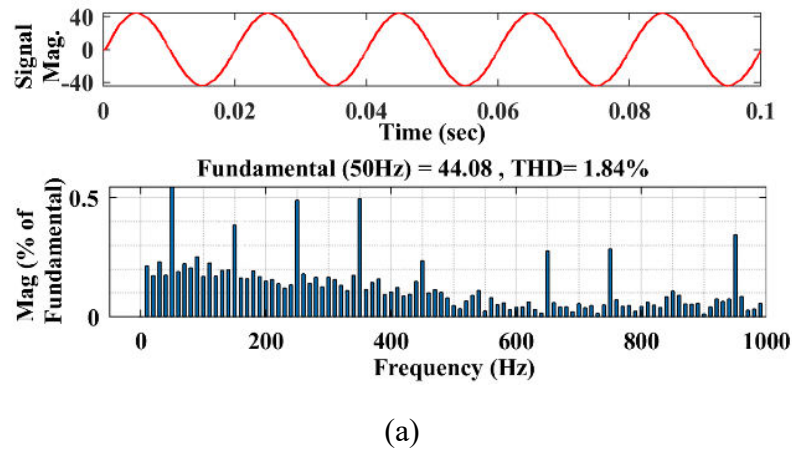
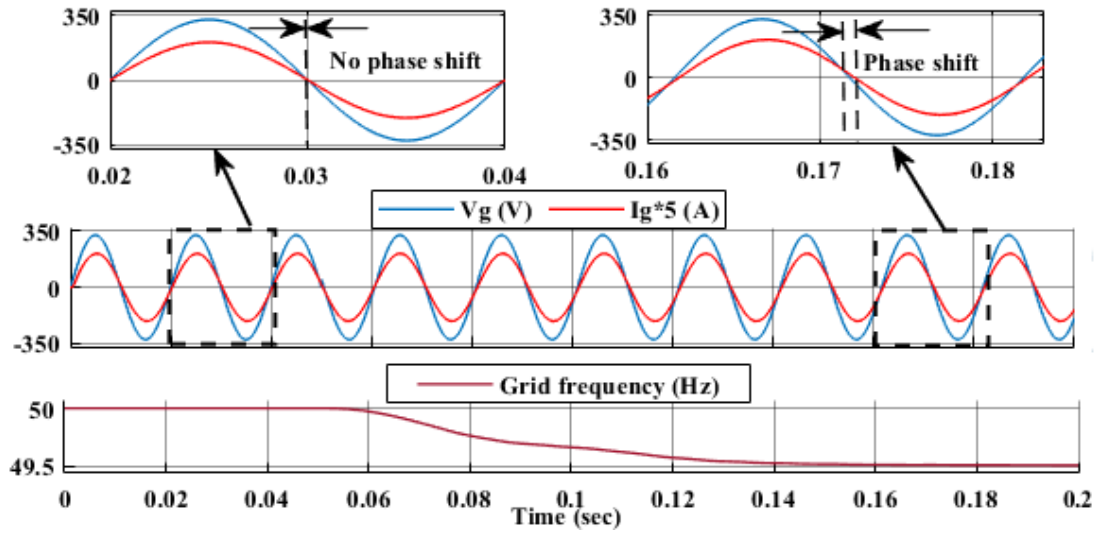


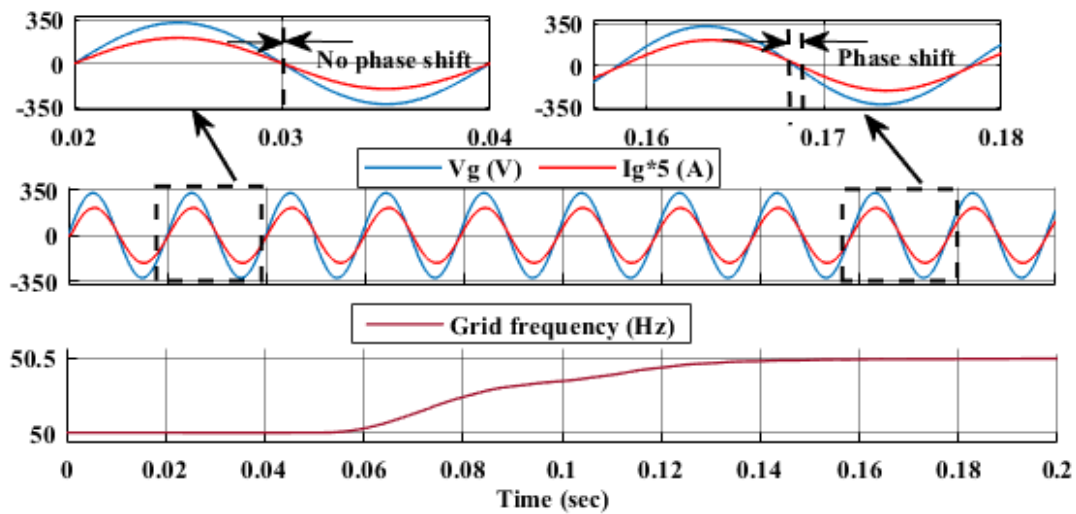
Fig.6.4. THD in grid I_g without frequency adaptability when grid frequency (a) 50 Hz (b) 49.5 Hz and (c) 50.5 Hz.

THD in grid current during mode 1 without frequency adaptation approach is shown in Fig.6.4. When the frequency of grid is exactly 50 Hz, the *THD* is 1.84% as illustrated in Fig.6.4 (a). However, the *THD* rises drastically while a small change in grid frequency, as depicted in Fig.6.4(b) & (c). The *THDs* during 49.5 Hz and 50.5 Hz grid frequencies are 7.46% and 7.94%, respectively. Furthermore, this is unacceptable since it exceeds the *THD* limit of 5% set by *IEEE-519* standard. Furthermore, during grid frequency variations, there is a phase-shift between current and even in charging operation as can be visible in Fig. 15.

Fig.6.5 (a) depicts the steady-state response of an *RC* controlled rectifier with a grid frequency of 50 Hz (i.e., $N_o = 20k / 50 = 400$), with a power factor of unity. The value of N_o (samples per period) is integer, it indicates that the *RC* controller is working properly. The frequency (f) was altered from 50 Hz to 49.5 Hz to evaluate the behavior of the repeated controlled converter in the presence of grid frequency changes. The sampling frequency remained constant at 20 kHz, resulting in a non-integer number of samples per period ($N_o = f_s / f$) ($N_o = 404.046$). Similarly, when the frequency varies from 50 to 50.5 Hz as shown in Fig 6.5 (b), number of samples per period ($N_o = f_s / f$) ($N_o = 396.03$). Because the *CRC* technique can't handle non-integer values, N_o is rounded to the nearest integer value, which is $N_o = 400$. When the samples per period become non-integer and are rounded off to the nearest integer to operate with *CRC* schemes, the peak-to-peak current tracking error considerably rises due to grid frequency variance. As a result, the *THD* value in grid current will be high. The frequency of the grid in *AC-DC* converters is an uncontrollable parameter, and based on the simulations presented in this section, it has been determined that when the samples per period become non-integer and the sampling frequency is fixed, the performance of *RC* control declines dramatically. As a result, the *FORC* technique was created to deal with fractional period periodic signals, as discussed in Chapter 5.



(a)



(b)

Fig.6.5. Phase difference between I_g and V_g without frequency adaptability due to frequency deviation (a) at 49.5Hz (b) at 50.5Hz.

The experiments have been carried out using FORC to compare the performance in the present of variable frequency. It can be clearly seen that the FD filter based FORC is capable of tracking periodic signal under variable grid frequency. *THD* in grid current during mode 1 using frequency adaptability approach has depicted in Fig.6.6. The grid-current's *THD* is in the allowable limit and does not change considerably when the frequency changes. With 49.5 Hz and 50.5 Hz, grid frequencies, *THD* being 1.86% and

1.99%, respectively. Furthermore, when employing the frequency adaptation approach as indicated in Fig.6.7, there is no phase difference between grid current & voltage.

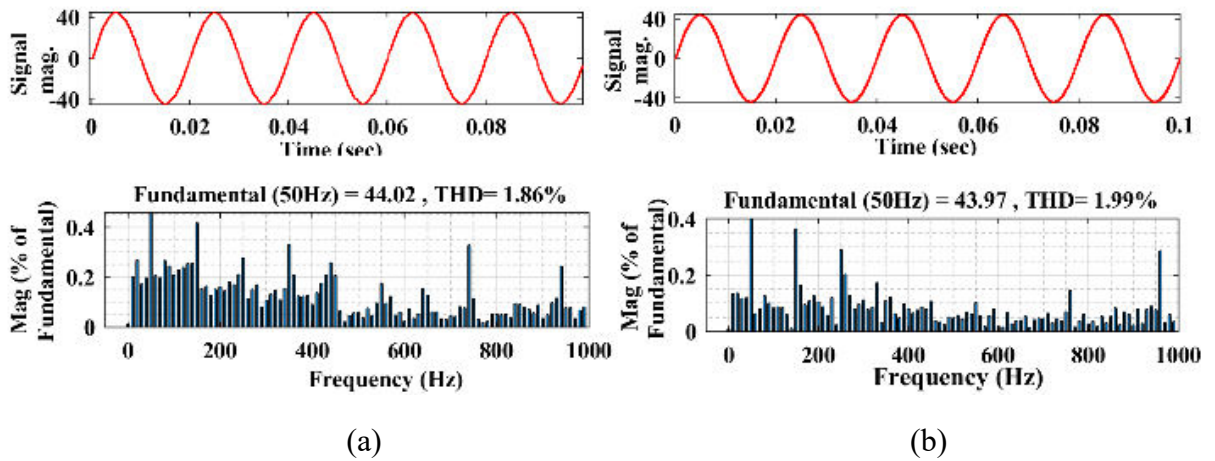
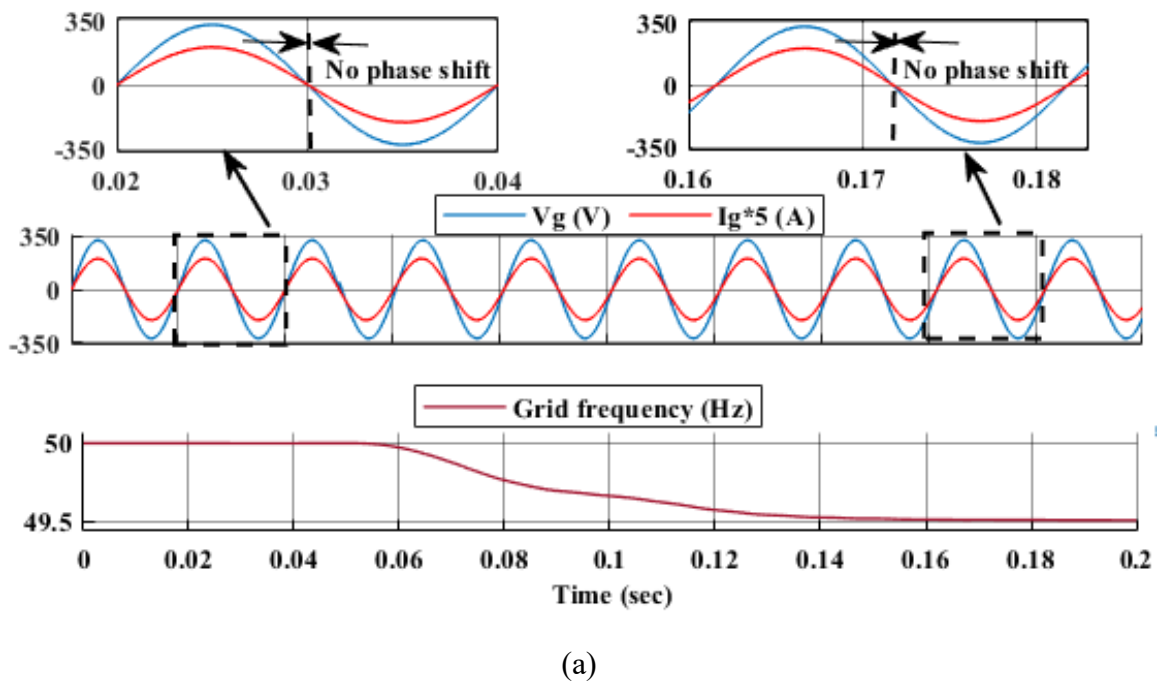
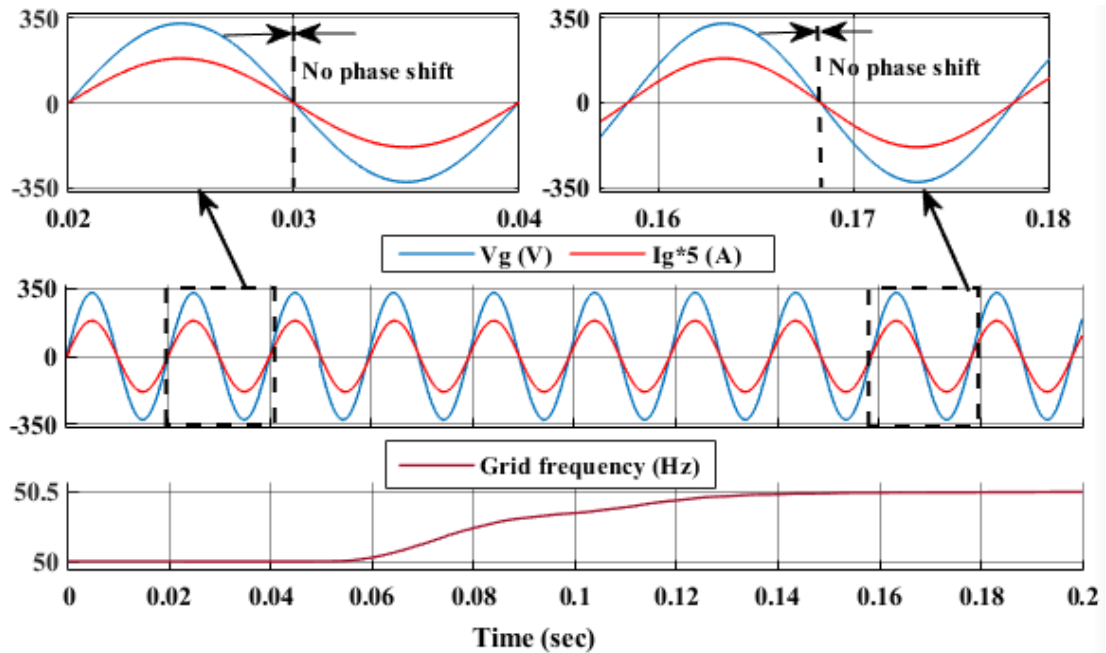


Fig.6.6. THD in grid I_g with frequency adaptability when grid frequency (a) 49.5 Hz and (b) 50.5 Hz.





(b)

Fig.6.7. No phase difference between I_g and V_g with frequency adaptability due to frequency deviation (a) at 49.5Hz (b) at 50.5Hz.

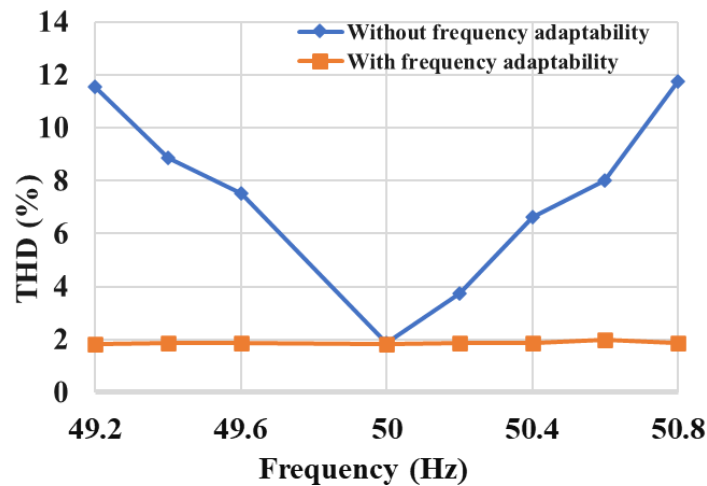
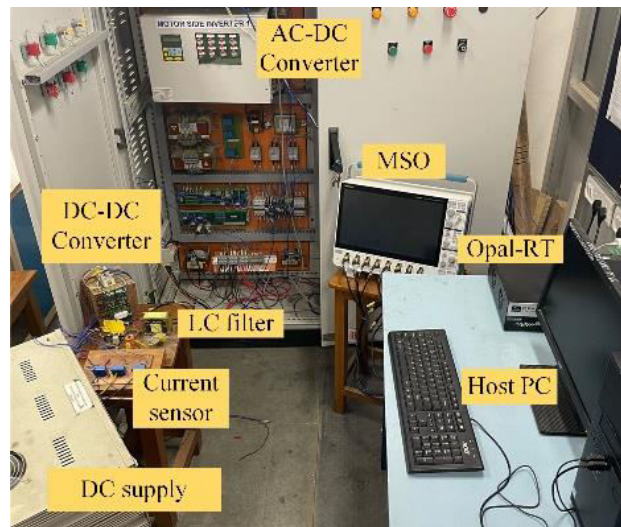


Fig.6.8. THD comparison

The grid-current THD is compared in Fig.6.8 without and with frequency adaptability technique. It can be noted that with frequency adaptability technique, almost constant THD has been maintained even after variations in the grid frequency.

6.2 Experimental Results

The performance of the proposed control approach is evaluated in a real-time 500 VA experimental setup, as shown in Fig.6.9. Both converters are made up from IGBT Semikron legs, and a battery pack of 96 V has been designed by combining eight 12 V/7 Ah batteries in series.



(a)



(b)

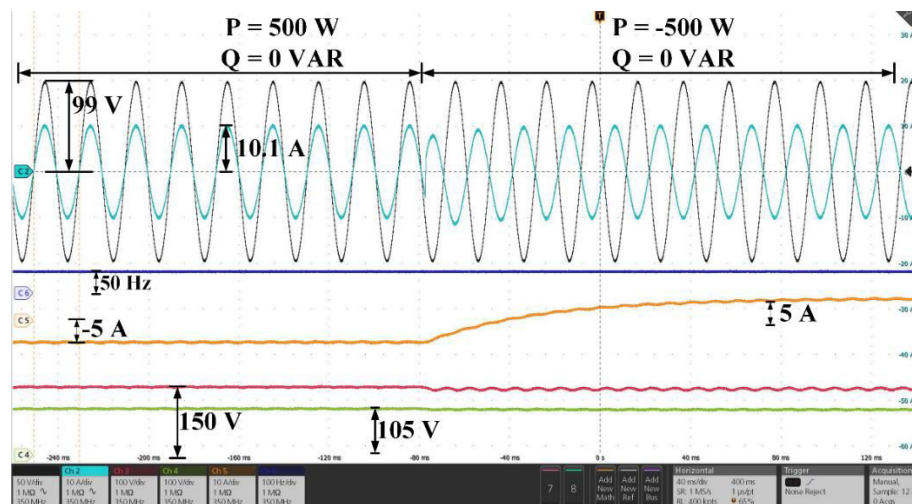
Fig.6.9 Hardware setup (a) Hardware Setup (b) Battery bank.

The experimental parameters are enumerated in Table II. The DC link voltage has been maintained at 150 V, and the controller's performance has also been verified in real time using four modes relating to battery charging/discharging and reactive power correction. However, in real-time configuration, the EV charger's operational rating is limited to 500 VA in all working modes.

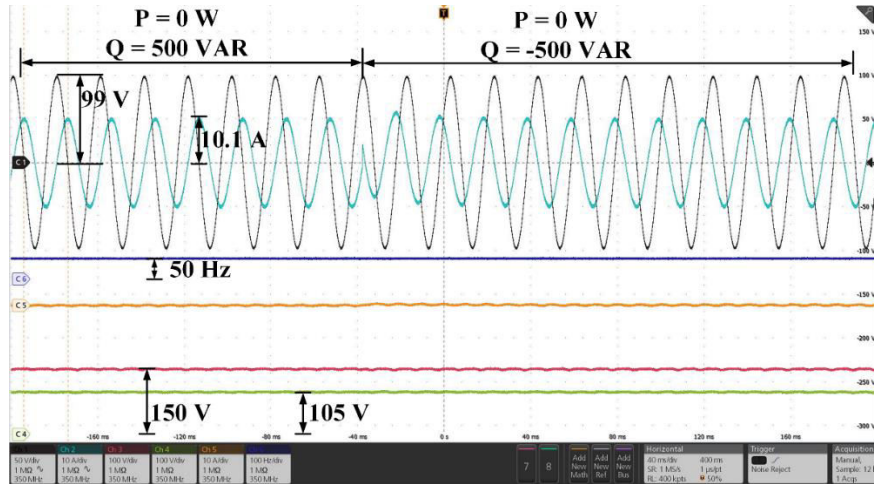
Table VIII
Modes of Operation

Mode	P(W)	Q (VAR)	S (VA)
1	500	0	500
2	-500	0	500
3	0	500	500
4	0	-500	500

Fig.6.10 (a) and (b), shows the transitions from mode 1 to mode 2 & from mode 3 to mode 4 respectively. The charging and discharging of a battery pack are depicted in Fig.6.10 (a), with the battery current being negative during charging and positive during discharging. In mode 1, the AC side current and voltage are perfectly in phase, whereas they are out of phase in mode 2. Similarly, during the changeover from mode 3 to 4, the phase difference of 90° lagging and leading, as shown in Fig.6.10 (b). Furthermore, during all four operating modes the DC-link voltage has been maintained at 150 V.

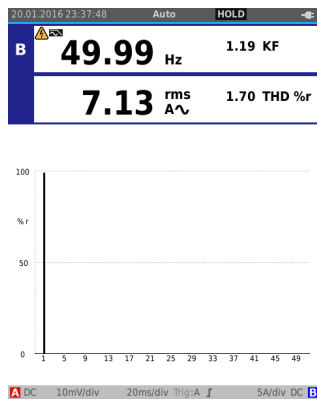


(a)

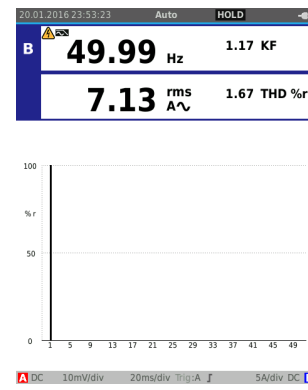


(b)

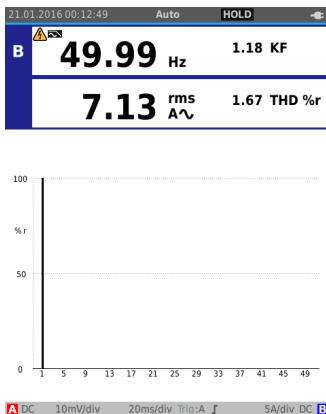
Fig.6.10. Transition with RC from (a) mode 1 to 2 and (b) mode 3 to 4.



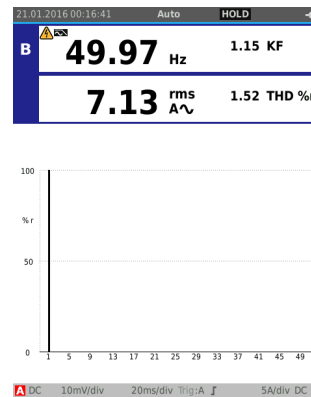
(a)



(b)



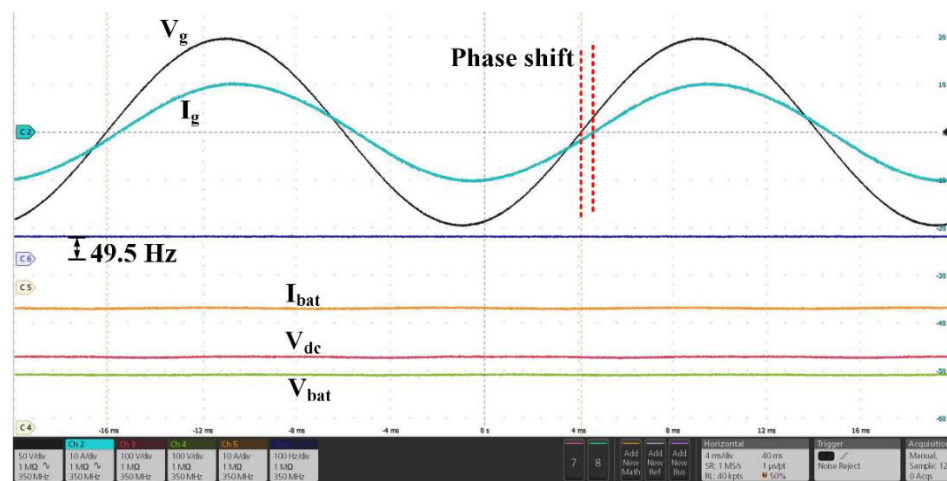
(c)



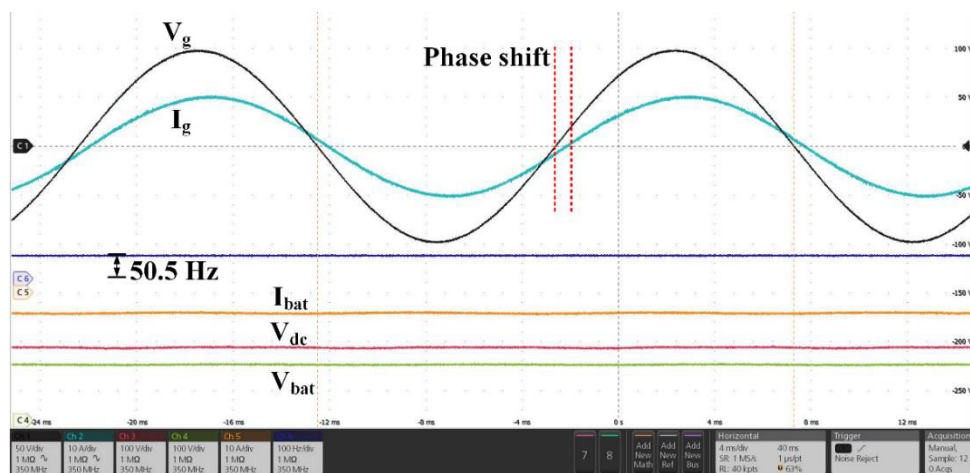
(d)

Fig.6.11. THD in I_g at 50 Hz (a) Mode 1 (b) Mode 2 (c) Mode 3 (d) Mode 4

The frequency adaptability of the proposed controller was evaluated during charging mode. By varying the supply frequency to 49.5 Hz and 50.5 Hz, Fig.6.12 (a) and (b) exhibit the experimental results of an EV charger controller without frequency adaptability. When the supply frequency changed, the controller's performance deteriorated resulting in a phase shift between grid-current and grid-voltage, as illustrated in Fig.6.12(a). When the AC side frequency is 50.5 Hz, as illustrated in Fig.6.12(b), a phase shift may also be noticed. In addition, as indicated in the simulation results, changes in AC side frequency increase THD in grid current.



(a)

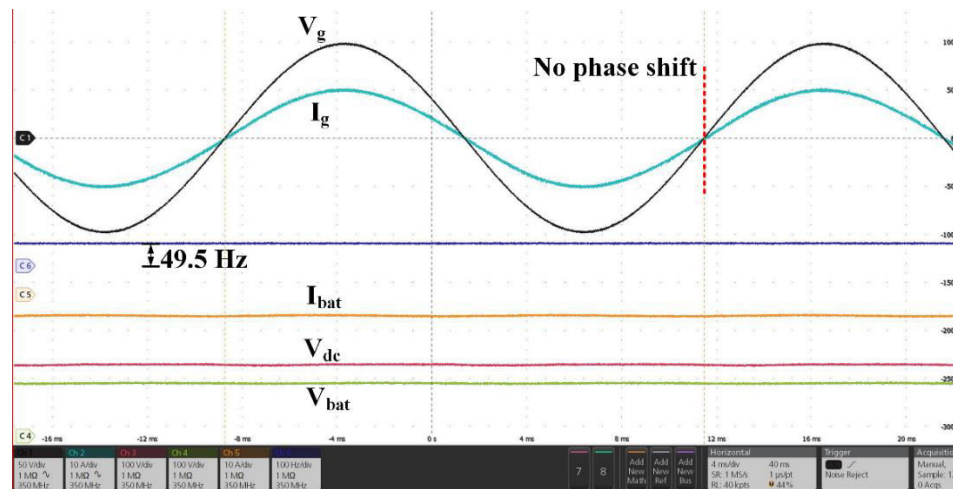


(b)

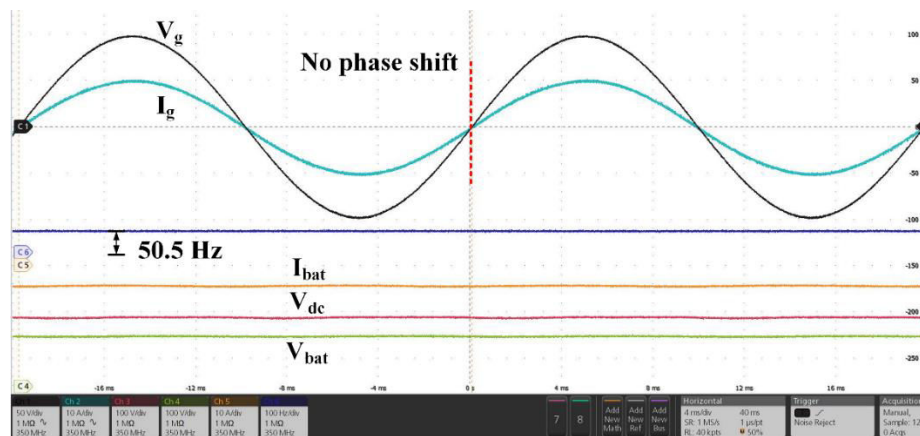
Fig.6.12. Steady-state performance of the RC without frequency adaptability scheme at

(a) 49.5 Hz (b) 50.5 Hz

Fig.6.13. illustrates the results of an EV charger controller in charging mode with frequency adaptability when the supply frequency has been slightly varied between 49.5 Hz and 50.5 Hz. Even when the AC side frequency varies, there is no phase shift between the voltage and current on the AC side. As a result, the controller aids in keeping THD in AC side current within the allowable limit of 5%.



(a)

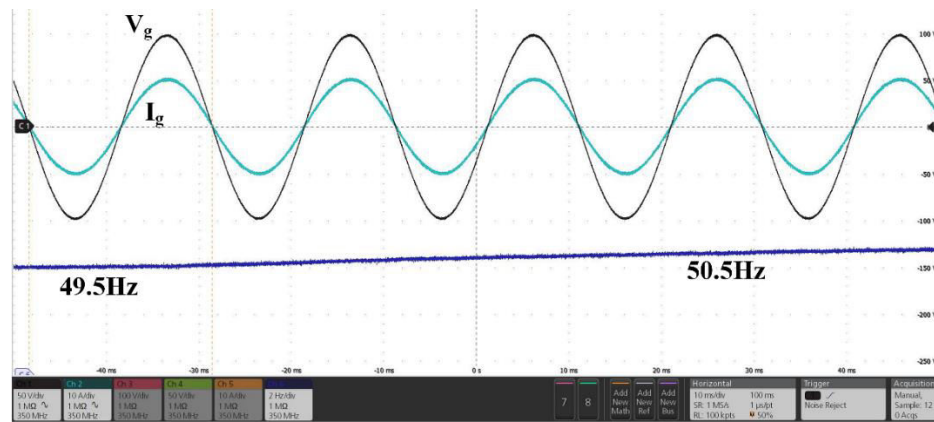


(b)

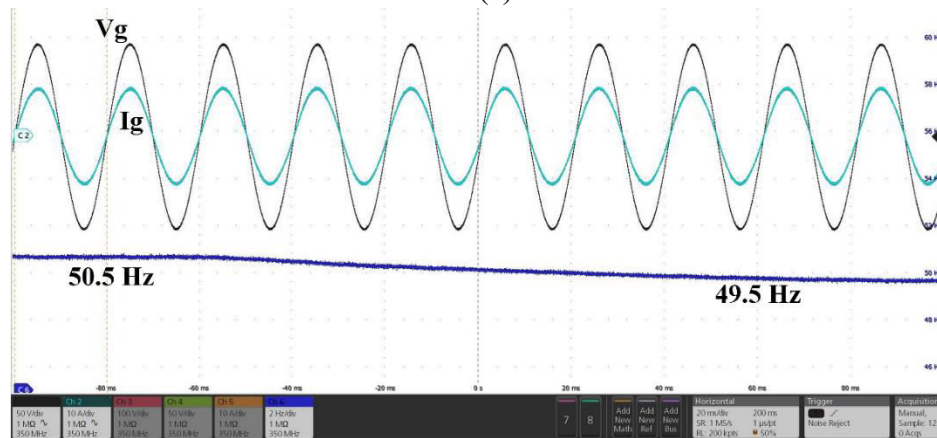
Fig.6.13. Steady-state performance of the frequency adaptive RC controller at (a) 49.5 Hz
(b) 50.5 Hz

More experiments have been carried out in order to better assess the frequency adaptive RC controller's dynamic performance. Fig. 6.14 shows the dynamic performance of the frequency adaptability RC controller under frequency step changes. The frequency

adaptability RC controller method is shown to be resistant to grid frequency fluctuations. As a result, the proposed controller provides excellent tracking accuracy.



(a)



(b)

Fig.6.14. Dynamic performance of the frequency adaptive technique under grid frequency step changes (a) 49.5 Hz – 50.5 Hz (b) 50.5 Hz – 49.5 Hz

Chapter 7

CONCLUSION AND FUTURE SCOPE

7.1 CONCLUSION

The development of various electric vehicle (EV) charger controllers is the subject of this effort. The EV charger has two conversion stages: AC-DC (first) and DC-DC (second). These two converters are the most important parts of an electric vehicle charger. The EV charger is intended to charge and discharge the battery pack while also compensating for reactive power. Both converters are intended to work in both directions for this reason. IGBT switches with an anti-parallel diode are used to create the converters. The EV charger can both charge the battery pack and transmit battery power to the grid or a local load.

On-board EV charger and its controller has been developed in this project. The two-stage EV charger needs two different controllers, one for each conversion step (AC-DC and DC-DC). The major goal of this project is to provide control algorithms for first-stage AC-DC converters in order to address numerous EV charging issues. In all EV charger controllers, however, the generic control technique is employed for the second stage DC-DC converter. All EV charger controllers are built to follow any active/reactive power command within the range of the EV charger's rating.

The active/reactive power, grid side current, DC link voltage, and battery current are all managed in an EV charger controller. The proposed controller regulates three quantities: active/reactive power, grid side current, and AC-DC converter control. The remaining two values, DC link voltage and battery current, are controlled by the DC-DC converter. In this scenario, three references are provided, with the remaining two being produced by them. The control of an AC-DC converter is divided into two loops, the outer and inner loops. The outer loop creates the inner control loop's reference. The active/reactive power is tracked in the outer loop, which creates the grid current reference for the inner current control loop.

In this work, Frequency adaptive RC has been suggested to provide optimal control scheme to track or eliminate harmonics under normal or varying grid frequency for the EV charger. The controller's performance was evaluated in various modes and found to be satisfactory in terms of steady-state performance along with fast dynamic response. The RC controller's analysis and synthesis have been thoroughly examined. Furthermore, by approximating the fractional delay with a Lagrange-interpolating polynomial, the RC's frequency adaptability is improved. The controller has been successfully installed on the first stage of an on-board electric vehicle charger, and its performances has been evaluated using MATLAB/Simulink and a real-time experimental setup. The THD has been maintained in the permissible limit. In the results, it has been found that the proposed control technique is very advantageous for EV charging applications and helps to maintain the quality of grid current while small variation in grid frequency or PLL estimation error. The claims are verified by both simulation and experimental results.

7.2 FUTURE SCOPE

- Under variable or uncertain frequency reference/disturbance signal situations, an Advanced Repetitive Controller (ARC) is utilized to improve repetitive control performance. It incorporates a fractional delay filter based on Taylor series expansion to provide the required non-integer delay.
- Throughout this research, only first order RC controllers have been studied, and a higher order RC controller within the ARC could improve the system's tolerance to reference frequency alterations while also affecting the stability range. As a result, future work could include comparing the performance of the two controllers for the same plant by substituting first order RC with a higher order RC within ARC.

APPENDIX A

MODELING OF EV CHARGER

A.1 AC-DC Converter Modeling (Single-phase)

Mathematical modelling of single-phase AC-DC converter has been done in this section. A switching model of AC-DC converter has been shown in the Fig.A.1.

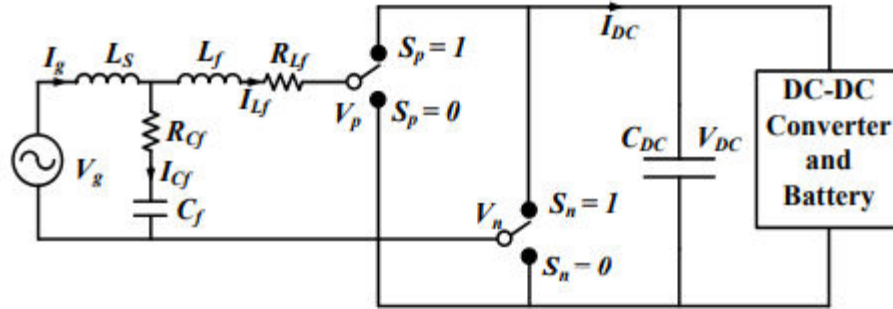


Fig.A.1. AC-DC converter switching model

Figure 3.2 depicts the switching model of a single-phase AC-DC converter. A single pole double throw switch represents each leg of Fig. 3.1. The grid voltage is represented by V_g , the grid side inductor is L_s , the AC side filter inductance and capacitance are L_f and C_f , respectively, and the equivalent series resistance (ESR) of filter inductance and capacitance is R_{Lf} and R_{Cf} . The on states of switches S_1 and S_3 are represented by $S_p = 1$ and $S_p = 0$ correspondingly. $S_n = 1$ and $S_n = 0$ denote the on and off states of switch S_2 and S_4 , respectively.

$$\begin{aligned} V_{pn} &= V_p - V_n \\ &= S_p \cdot V_{DC} - S_n \cdot V_{DC} = (S_p - S_n)V_{DC} \\ &= S_{pn} \cdot V_{DC} \end{aligned} \quad (A.1)$$

$$\text{Here} \quad S_{pn} = S_p - S_n \quad (A.2)$$

$$\text{Also,} \quad I_{DC} = (S_p - S_n)V_{DC} = S_{pn} \cdot I_{Lf} \quad (A.3)$$

Applying KVL in the outer loop. Neglect the capacitor ESR,

$$\begin{aligned} V_g &= V_{L_s} + V_{C_f} \\ \frac{dI_g}{dt} &= \frac{V_g}{L_s} - \frac{V_{C_f}}{L_s} \end{aligned} \quad (A.4)$$

Applying KVL, in the inner loop, we get

$$\begin{aligned} V_{Cf} &= V_{Lf} + I_{Lf} \cdot R_{Lf} + V_{pn} \\ \frac{dI_{Lf}}{dt} &= \frac{V_{Cf}}{L_f} - \frac{I_{Lf} \cdot R_{Lf}}{L_f} - \frac{V_{pn}}{L_f} \end{aligned} \quad (\text{A.5})$$

At junction. Applying KCL, will get

$$\begin{aligned} I_g &= I_{Lf} + I_{Cf} \\ \frac{dV_{Cf}}{dt} &= \frac{I_g}{C_f} - \frac{I_{Lf}}{C_f} \end{aligned} \quad (\text{A.6})$$

A.1.2 AC-DC Converter: Average Model

Applying the averaging operator to the switching model across one switching period yields the average model of the system. For a time-varying variable y , the averaging operator is defined as,

$$\tilde{y} = \frac{1}{T} \int_0^T y(\tau) d\tau \quad (\text{A.7})$$

\tilde{y} is the average value. Hence, by using averaging operator to (A.4- A.6), following equations can be deduced:

$$\frac{d\tilde{I}_g}{dt} = \frac{\tilde{V}_g}{L_s} - \frac{\tilde{V}_{Cf}}{L_s} \quad (\text{A.8})$$

$$\frac{d\tilde{I}_{Lf}}{dt} = \frac{\tilde{V}_{Cf}}{L_f} - \frac{\tilde{I}_{Lf} \cdot R_{Lf}}{L_f} - \frac{d_{pn} \cdot V_{DC}}{L_f} \quad (\text{A.9})$$

Here,

$$d_{pn} = \tilde{S}_{pn} \quad (\text{A.10})$$

$$\frac{d\tilde{V}_{Cf}}{dt} = \frac{\tilde{I}_g}{C_f} - \frac{\tilde{I}_{Lf}}{C_f} \quad (\text{A.11})$$

d_{pn} represents the average value for S_{pn} and V_{DC} is DC link's average voltage.

A.1.2 AC-DC Converter: Small Signal Model

Applying the averaging operator to the switching model across one switching period yields

the average model of the system. For a time-varying variable y , the averaging operator is defined as,

$$\frac{d\tilde{I}_g}{dt} = \frac{\tilde{V}_g}{L_s} - \frac{\tilde{V}_{Cf}}{L_s} \quad (\text{A.12})$$

$$\frac{d\tilde{I}_{Lf}}{dt} = \frac{\tilde{V}_{Cf}}{L_f} - \frac{\tilde{I}_{Lf} \cdot R_{Lf}}{L_f} - \frac{\tilde{d}_{pn} \cdot V_{dc}}{L_f} \quad (\text{A.13})$$

$$\frac{d\tilde{V}_{Cf}}{dt} = \frac{\tilde{I}_g}{C_f} - \frac{\tilde{I}_{Lf}}{C_f} \quad (\text{A.14})$$

Taking Laplace Transform, we get,

$$S\tilde{I}_g = \frac{\tilde{V}_g}{L_s} - \frac{\tilde{V}_{Cf}}{L_s} \quad (\text{A.15})$$

$$S\tilde{I}_{Lf} = \frac{\tilde{V}_{Cf}}{L_f} - \frac{\tilde{I}_{Lf} \cdot R_{Lf}}{L_f} - \frac{\tilde{d}_{pn} \cdot V_{dc}}{L_f} \quad (\text{A.16})$$

$$S\tilde{V}_{Cf} = \frac{\tilde{I}_g}{C_f} - \frac{\tilde{I}_{Lf}}{C_f} \quad (\text{A.17})$$

From (A.15)
$$\tilde{I}_g = \frac{\tilde{V}_g}{L_s} - \frac{\tilde{V}_{Cf}}{L_s} \quad (\text{A.18})$$

Putting the (A.18) into (A.17), we get,

$$\begin{aligned} S\tilde{V}_{Cf} &= \frac{1}{C_f} \left(\frac{\tilde{V}_g}{SL_s} - \frac{\tilde{V}_{Cf}}{SL_s} \right) - \frac{\tilde{I}_{Lf}}{C_f} \\ \tilde{V}_{Cf} &= \frac{\tilde{V}_g}{S^2L_sC_f + 1} - \frac{\tilde{I}_{Lf} \cdot SL_s}{S^2L_sC_f + 1} \end{aligned} \quad (\text{A.19})$$

Now, put (A.19) into (A.16)

$$\begin{aligned} S\tilde{I}_{Lf} &= \frac{1}{L_f} \left(\frac{\tilde{V}_g}{S^2L_sC_f + 1} - \frac{\tilde{I}_{Lf} \cdot SL_s}{S^2L_sC_f + 1} \right) - \frac{\tilde{I}_{Lf} \cdot R_{Lf}}{L_f} - \frac{\tilde{d}_{pn} \cdot V_{dc}}{L_f} \\ \tilde{I}_{Lf} &= \frac{\tilde{V}_g}{S^3L_fL_sC_f + S^2L_sC_fR_{Lf} + S(L_f + L_s) + R_{Lf}} \\ &\quad - \tilde{d}_{pn} \cdot V_{dc} \left(\frac{S^2L_sC_f + 1}{S^3L_fL_sC_f + S^2L_sC_fR_{Lf} + S(L_f + L_s) + R_{Lf}} \right) \end{aligned} \quad (\text{A.20})$$

If the grid voltage disturbance is considered to be zero, the final relationship is as continues to follow:

$$\widetilde{I}_{L_f} = -\widetilde{d}_{pn} \cdot V_{dc} \left(\frac{S^2 L_S C_f + 1}{S^3 L_f L_S C_f + S^2 L_S C_f R_{L_f} + S(L_f + L_S) + R_{L_f}} \right) \quad (\text{A.21})$$

(A.21) approaches to the equation shown below at high frequencies,

$$\widetilde{I}_{L_f} = \frac{-\widetilde{d}_{pn} \cdot V_{dc}}{S L_f + R_{L_f}} \quad (\text{A.22})$$

It can be seen from the above equation that with reduction in \widetilde{I}_{L_f} , d_{pn} increases because of the negative sign. Hence the transfer function of plant become

$$G_{pac} = V_{dc} \cdot \frac{1}{S L_f + R_{L_f}} \quad (\text{A.23})$$

A.2 Battery Pack Modelling

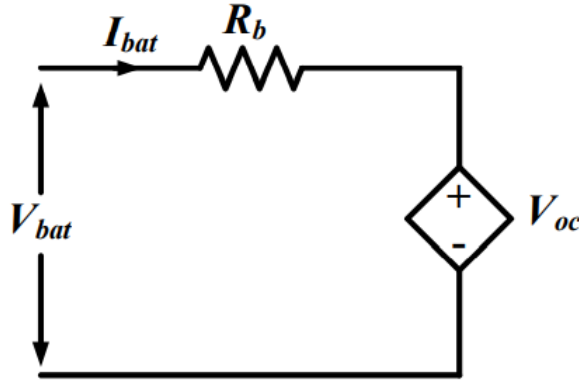


Fig.A.2. Battery pack equivalent model

The Li-ion cell is utilized to build the battery pack because of its well-known benefits. At the lowest SOC value of 20%, the cut off voltage of a Li-ion cell is 2.95 V for a nominal cell voltage of 3.3 V. When the SOC reaches 90%, the maximum output voltage is 3.6 V. Each cell's nominal current capacity is 18 Ah. The number of cells required in each string linked in series to create the 350 V battery pack is $350/3.3 = 106.06$. 107 cells are the closest integer value. As a result, this battery pack's maximum voltage is $107 \cdot 3.6 = 385.2$ V, and its lowest voltage is $107 \cdot 2.95 = 315.65$ V. Each string has a nominal capacity of 18 Ah $350 \text{ V} = 6.3 \text{ kWh}$. The capacity of the battery pack, on the other hand, may be extended by attaching another string in parallel. Fig.A.3 depicts the similar battery pack model. The internal resistance of the battery is R_b , while the open circuit voltage of the

battery pack is V_{oc} . For 1KHz AC battery charging current, the initial internal resistance is less than 4mohm, according to the battery manufacturer's data sheet. This internal resistance, however, is valid for a charging rate of 0.55 C, or 10 A. Internal resistance of Li-ion batteries is often higher since it is related to charging current. As a result, 10mOhm per cell is chosen. The total internal resistance is 10mohm * 107 ohm since each string has 107 cells linked in series. Furthermore, the battery open circuit voltage fluctuates with the present state of charge.

A.3. DC-DC Converter Modeling

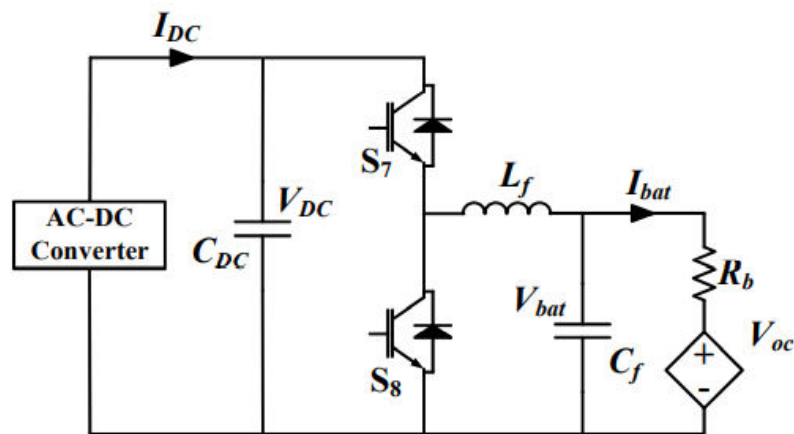


Fig.A.3. DC-DC Converter

Fig.A.3. It is made up of two IGBT switches that operate in both directions. It operates in buck mode when a battery is present and boost mode when active power is sent to the grid.

- Switch S_7 is on & S_8 is off

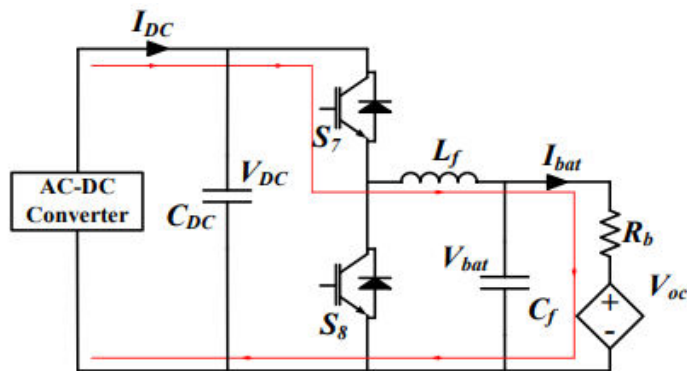


Fig.A.4. Buck Operation State: ON

Apply KVL, we get,

$$V_{dc} = V_{lf} + V_{bat} \quad (A.24)$$

$$\frac{dI_{L_f}}{dt} = \frac{V_{DC}}{L_f} - \frac{V_{bat}}{L_f} \quad (A.25)$$

Here, V_{bat} and V_{lf} are the voltage across the battery/ capacitance C_f and inductance L_f .

At battery side, applying KCL gives,

$$\begin{aligned} I_{L_f} &= I_{C_f} + I_{bat} \\ \frac{dV_{bat}}{dt} &= \frac{I_{L_f}}{C_f} - \frac{I_{bat}}{C_f} \end{aligned} \quad (A.26)$$

Here, the current through capacitor C_f is I_{C_f} . now apply KCL at DC- link capacitor gives,

$$\begin{aligned} I_{DC} &= I_{CDC} + I_{L_f} \\ \frac{dV_{DC}}{dt} &= \frac{I_{DC}}{C_{DC}} - \frac{I_{L_f}}{C_{DC}} \end{aligned} \quad (A.27)$$

- Switch S7 OFF and S8 ON

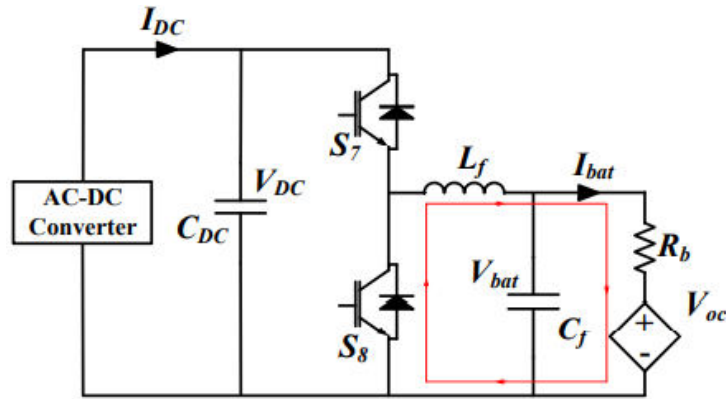


Fig.A.5 Buck Operation State: OFF

Apply KVL in battery loop,

$$\begin{aligned} 0 &= V_{L_f} + V_{bat} \\ \frac{dI_{L_f}}{dt} &= -\frac{V_{bat}}{L_f} \end{aligned} \quad (A.28)$$

At battery side, apply KCL,

$$\begin{aligned} I_{L_f} &= I_{C_f} + I_{bat} \\ \frac{dV_{bat}}{dt} &= \frac{I_{L_f}}{C_f} - \frac{I_{bat}}{C_f} \end{aligned} \quad (A.29)$$

Now, at DC link capacitor side, apply KCL,

$$\begin{aligned} I_{DC} &= I_{CDC} \\ \frac{dV_{DC}}{dt} &= \frac{I_{DC}}{C_{DC}} \end{aligned} \quad (A.30)$$

Duty cycle d and $(1-d)$ can be used to average the on and off states. The duty cycle for switch S_7 is denoted by d . When the KVL equations (A.25) and (A.28) are averaged, the result is

$$\begin{aligned} \frac{d\tilde{\Gamma}_{L_f}}{dt} &= d \left(\frac{\tilde{V}_{DC}}{L_f} - \frac{\tilde{V}_{bat}}{L_f} \right) + (1-d) \left(-\frac{\tilde{V}_{bat}}{L_f} \right) \\ \frac{d\tilde{\Gamma}_{L_f}}{dt} &= \frac{d \cdot \tilde{V}_{DC}}{L_f} - \frac{\tilde{V}_{bat}}{L_f} \end{aligned} \quad (A.31)$$

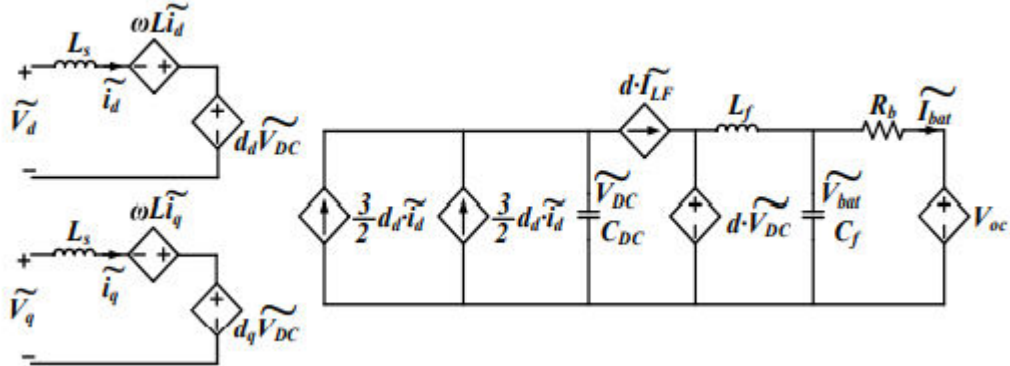


Fig.A.6. Two-stage bidirectional EV charger's average model

Now, averaging of KCL equation given in (A.26) – (A.29), results in

$$\begin{aligned} \frac{d\tilde{V}_{bat}}{dt} &= d \left(\frac{\tilde{I}_{L_f}}{C_f} - \frac{\tilde{I}_{bat}}{C_f} \right) + (1-d) \left(\frac{\tilde{I}_{L_f}}{C_f} - \frac{\tilde{I}_{bat}}{C_f} \right) \\ \frac{d\tilde{V}_{bat}}{dt} &= \frac{\tilde{I}_{L_f}}{C_f} - \frac{\tilde{I}_{bat}}{C_f} \end{aligned} \quad (A.32)$$

Now, after averaging the KVL of (A.27) – (A.30), we get,

$$\begin{aligned}\frac{d\widetilde{V}_{DC}}{dt} &= d \left(\frac{\widetilde{I}_{DC}}{C_{DC}} - \frac{\widetilde{I}_{Lf}}{C_{DC}} \right) + (1-d) \left(\frac{\widetilde{I}_{DC}}{C_{DC}} \right) \\ \frac{d\widetilde{V}_{DC}}{dt} &= \frac{\widetilde{I}_{DC}}{C_{DC}} - \frac{d \cdot \widetilde{I}_{Lf}}{C_{DC}}\end{aligned}\tag{A.33}$$

Average expression for the model of DC-DC converter has been shown in (A.31), (A.32) and (A.33).

Fig.A.6 depicts the equivalent circuit of both conversion stages is shown in Fig.A.6. For the sake of simplicity, this averaged model does not account for converter losses. However, for efficiency analysis, the non-idealities of converter switches, inductors, and capacitors are necessary, which is not the case here. This model's main goal is to show the dynamic behavior of a designed EV charger.

APPENDIX B

COMPONENT CALCULATION

This section encompasses the design of both on-board and off-board electric vehicle chargers. Rating and operating voltage are the main differences between on-board and off-board EV chargers, and the values of EV charger components are determined by these values. Based on a literature review, it was discovered that on-board EV charger ratings range from 3.3 to 9.4 kW, therefore it was built and simulated in MATLAB for 7.2 kW.

B.1. DC Link Voltage

DC link voltage, for the proper rectification should be more the peak line to line voltage and the battery voltage. As the battery voltage is 350V, also it varies as per SOC. Hence the DC link voltage has been selected as 400V.

Minimum value for the DC link voltage can be calculated as:

$$\begin{aligned} V_{DC \min_on} &> \sqrt{2} \cdot V_{ph} \\ &> \sqrt{2} \cdot 230 > 325.26V \end{aligned} \quad (B.1)$$

B.2. DC Link Capacitance

$$C_{dc} = \frac{2k_1 V_{ph} \alpha I_{ph} t}{(V_{dc}^2 - V_{dcmin}^2)} \quad (B.2)$$

Here, V_{dc} being dc link voltage, V_{dc_min} being the min. DC-link voltage, and overloading factor i.e., α is taken as 1.2. During dynamics, the energy dynamic constant (k_1) is 0.1. t being the time that DC link Voltage takes to recover.

$$= \frac{2 \times 0.1 \times 230 \times 1.2 \times 30 \times 0.015}{(400^2 - 325.26^2)} = 475.46\mu F$$

Therefore, DC link capacitor selected as 500 μ F.

B.3 Grid Side Inductor

$$L_{s_on} = \frac{\sqrt{3} \cdot m \cdot V_{DC}}{12 \cdot \alpha \cdot f_s \cdot I_{crpp}} \quad (B.3)$$

$$= \frac{\sqrt{3} \times 1 \times 400}{12 \times 1.2 \times 20000 \times 3} = 0.8\text{mH}$$

The grid side inductor selected as 1mH.

B.4 DC- DC Converter Filter

The bidirectional DC-DC converter may operate in both buck and boost modes. The initial duty cycle in buck and boost mode is computed as follows to determine the filter inductor and capacitor. V_{dc} denotes the DC link voltage, whereas V_{bat} denotes the battery voltage.

$$D_{\text{buck}} = \frac{V_2}{V_1} = \frac{350}{600} = 0.875 \quad (\text{B.4})$$

$$D_{\text{boost}} = 1 - \frac{V_2}{V_1} = 1 - \frac{350}{600} = 0.125 \quad (\text{B.5})$$

To calculate the filter inductance and capacitance:

$$L_f = \frac{V_2 \times D_{\text{boost}}}{\Delta I_L \times f_s} = \frac{350 \times 0.4167}{3.5 \times 20 \times 10^3} = 2.1\text{mH} \quad (\text{B.6})$$

$$C_f = \frac{1 - D_{\text{buck}}}{8 \cdot L_f (\Delta V_2 / V_2) f_s^2} = \frac{1 - 0.5833}{8 \times 2.1 \left(\frac{35}{350}\right) \times (20 \times 10^3)^2} = 6.2\mu\text{F} \quad (\text{B.7})$$

LIST OF PUBLICATIONS

1. S. Chalia, A. K. Seth and M. Singh, "Electric Vehicle Charging Standards in India and Safety Consideration," 2021 IEEE 8th Uttar Pradesh Section International Conference on Electrical, Electronics and Computer Engineering (UPCON), 2021, pp. 1-6, doi: 10.1109/UPCON52273.2021.9667649.
2. S. Chalia, A. K. Seth and M. Singh, "Frequency Adaptive First Order Periodic Current Controller for Electric Vehicle Charger," in IEEE Transactions on Transportation Electrification. (Communicated)
3. S. Chalia, A. K. Seth and M. Singh, Frequency Adaptive Discrete Repetitive Controller Design for Electric Vehicle Charger, International Journal of Electrical Power & Energy Systems. (Communicated)

BIBLIOGRAPHY

- [1] L. Wang, Z. Qin, T. Slangen, P. Bauer and T. van Wijk, "Grid Impact of Electric Vehicle Fast Charging Stations: Trends, Standards, Issues and Mitigation Measures - An Overview," in *IEEE Open Journal of Power Electronics*, vol. 2, pp. 56-74, 2021.
- [2] S. S. Williamson, A. K. Rathore and F. Musavi, "Industrial Electronics for Electric Transportation: Current State-of-the-Art and Future Challenges," in *IEEE Transactions on Industrial Electronics*, vol. 62, no. 5, pp. 3021-3032, May 2015.
- [3] D. Sahu and P. S. R. Nayak, "A Substantial Modelling and Analysis of Solar Powered e-Rickshaw Drive System," *2021 International Conference on Sustainable Energy and Future Electric Transportation (SEFET)*, 2021.
- [4] Aakash Kumar Seth, Mukhtiar Singh, "Unified adaptive neuro-fuzzy inference system control for OFF board electric vehicle charger," *International Journal of Electrical Power & Energy Systems*, Vol. 130, 2021.
- [5] Chan, C.C., Bouscayrol, A, Chen, K., "Electric, hybrid, and fuel-cell vehicles: architecture and modeling," *IEEE Trans. Veh. Technol.*, vol. 59, no. 52, pp. 589-598, 2010
- [6] SETHI, A. K. (2021). *CONTROL STRATEGIES FOR ELECTRIC VEHICLE CHARGING INFRASTRUCTURE* (Doctoral dissertation, DELHI TECHNOLOGICAL UNIVERSITY).
- [7] F. Zhang, X. Zhang, M. Zhang and A. S. E. Edmonds, "Literature review of electric vehicle technology and its applications," in *2016 5th International Conference on Computer Science and Network Technology*, Changchun, 2016.
- [8] Krein, M. Yilmaz and P. T., "Review of Battery Charger Topologies, Charging Power Levels, and Infrastructure for Plug-In Electric and Hybrid Vehicles," *IEEE Transactions on Power Electronics*, vol. 28, no. 5, pp. 2151-2169, 2013.
- [9] J. G. Pinto, V. Monteiro, H. Gonçalves and J. L. Afonso, "Onboard Reconfigurable Battery Charger for Electric Vehicles With Traction-to-Auxiliary Mode," *IEEE Transactions on Vehicular Technology*, vol. 63, no. 3, pp. 1104- 1116, 2014.
- [10] F. K. a. S. Hattori, "Single stage AD-DC full-bridge converter for battery charger,"

- in IEEE International Telecommunications Energy Conference (INTELEC), Osaka, 2015.
- [11] M. Kesler, M. C. Kisacikoglu and L. M. Tolbert, "Vehicle-to-Grid Reactive Power Operation Using Plug-In Electric Vehicle Bidirectional Offboard Charger," *IEEE Transactions on Industrial Electronics*, vol. 61, no. 12, pp. 6778- 6784, 2014.
- [12] C. Shi and A. Khaligh, "A Two-Stage Three-Phase Integrated Charger for Electric Vehicles With Dual Cascaded Control Strategy," *IEEE Journal of Emerging and Selected Topics in Power Electronics*, vol. 6, no. 2, pp. 898-909, 2018.
- [13]] Frede Blaabjerg, Ke Ma, and D. Zhou. Power electronics and reliability in renewable energy systems. *IEEE Int. Symp. Ind. Electron.*, pages 19–30, 2012.
- [14] Frede Blaabjerg, Florin Iov, T. Terekas, Remus Teodorescu, and Ke Ma. Power electronics - key technology for renewable energy systems. *2nd Power Electron. Drive Syst. ans Technol. Conf.*, pages 445–466, 2011.
- [15] Yilmaz Sozer and David a. Torrey. Modeling and control of utility interactive inverters. *IEEE Trans. Power Electron.*, 24(11):2475–2483, 2009.
- [16] Toshihisa Shimizu, Masaki Hirakata, Tomoya Kamezawa, and Hisao Watanabe. Generation control circuit for photovoltaic modules. *IEEE Trans. Power Electron.*, 16(3):293–300, 2001.
- [17] Yongheng Yang, Enjeti Prasad, Frede Blaabjerg, and Huai Wang. Suggested grid code modifications to ensure wide-scale adoption of photovoltaic energy in distributed power generation systems. In *IEEE-IAS Annu. Meet.*, pages 1–8, 2013.
- [18] Ric Hoefnagels, Martin Junginger, Christian Panzer, Gustav Resch, and Anne Held. Long term potentials and costs of RES Part I : potentials , diffusion and technological learning. Technical Report May, Fraunhofer Institute for Systems and Innovation Research (ISI), Germany, 2011.
- [19] L. El . Chaar, L. a. Lamont, and N. El . Zein. Review of photovoltaic technologies. *Renew. Sustain. energy Rev.*, 15(5):2165–2175, 2011.
- [20] Yun Seng Lim, Jianhui Wong, Miao San Serena Liew, Lin Yi Ace Khaw, Proportional integrator (PI) and fuzzy-controlled energy storage for zero-power flow between grid and local network with photovoltaic system, *Sustainable Energy*

- Technologies and Assessments, Volume 37,2020,100629,
- [21] ISSN 2213 1388, <https://doi.org/10.1016/j.seta.2020.100629>.
- [22] B. A. Francis, and W. M. Wonham, "The internal model principle for linear multivariable regulators," *Appl. Math. Optimization*, vol. 2, no. 2, pp. 170–194, 1975.
- [23] Mohamad Alaa Eddin Alali, Zakaria Sabiri, Yuri B. Shtessel, Jean-Pierre Barbot, Study of a common control strategy for grid-connected shunt active photovoltaic filter without DC/DC converter, *Sustainable Energy Technologies and Assessments*, Volume 45,2021,101149, ISSN 2213-1388, <https://doi.org/10.1016/j.seta.2021.101149>
- [24] B. A. Francis and W. M. Wonham. The internal model principle for linear multivariable regulators. *Appl. Math. Optim.*, 2(2):170–194, 1975.
- [25] Keliang Zhou, Danwei Wang, and Bin Zhang. Dual mode structure repetitive control of CVCF PWM inverters. 2009 IEEE 6th Int. Power Electron. Motion Control Conf., 3:1524–1526, may 2009.
- [26] Bin Zhang, Keliang Zhou, Yigang Wang, and Danwei Wang. Performance improvement of repetitive controlled PWM inverters: A phase-lead compensation solution. *Int. J. Circuit theory Appl.*, 38:453–469, 2010.
- [27] Wenzhou Lu, Keliang Zhou, Danwei Wang, and Ming Cheng. A general parallel structure repetitive control scheme for multiphase DC-AC PWM converters. *IEEE Trans. Power Electron.*, 28(8):3980–3987, 2013.
- [28] Marco Liserre, Remus Teodorescu, and Frede Blaabjerg. Multiple harmonics control for three-phase grid converter systems with the use of PI-RES current controller in a rotating frame. *IEEE Trans. Power Electron.*, 21(3):836–841, 2006.
- [29] Yongheng Yang, Keliang Zhou, and Frede Blaabjerg. Harmonics suppression for singlephase grid-connected PV systems in different operation modes. 2013 Twenty-Eighth Annu. IEEE Appl. Power Electron. Conf. Expo., pages 889–896, mar 2013.
- [30] Remus Teodorescu, Frede Blaabjerg, Marco Liserre, and Poh Chiang Loh. Proportionalresonant controllers and filters for grid-connected voltage-source

- converters. *IEE Proc. - Electr. Power Appl.*, 153(5):750–762, 2006.
- [31] Wenzhou Lu, Keliang Zhou, Danwei Wang, and Ming Cheng. A general parallel structure repetitive control scheme for multiphase DC-AC PWM converters. *IEEE Trans. Power Electron.*, 28(8):3980–3987, 2013.
- [32] Marco Liserre, Remus Teodorescu, and Frede Blaabjerg. Multiple harmonics control for three-phase grid converter systems with the use of PI-RES current controller in a rotating frame. *IEEE Trans. Power Electron.*, 21(3):836–841, 2006.
- [33] Mohamed Rashed, Christian Klumpner, and Greg Asher. Repetitive and resonant control for a single-phase grid-connected hybrid cascaded multilevel converter. *IEEE Trans. Power Electron.*, 28(5):2224–2234, 2013.
- [34] Electricity industry participation code 2010, Part 1, Preliminary provisions.
- [35] Zhenwei Cao and Gerard F. Ledwich. Periodic signals with fixed sampling rate. *IEEE/ASME Trans. Mechatronics*, 7(3):378–384, 2002.
- [36] Yigang Wang, Danwei Wang, Bin Zhang, and Keliang Zhou. Fractional delay based repetitive control with application to PWM dc/ac converters. In *16th IEEE Int. Conf. Control Appl.*, number October, pages 928–933, 2007.
- [37] Dong Chen, Junming Zhang, and Zhaoming Qian. An improved repetitive control scheme for grid-connected inverter with frequency-adaptive capability. *IEEE Trans. Ind. Electron.*, 60(2):814–823, 2013.
- [38] A. Narula and V. Verma, "Bi – directional trans – Z source boost converter for G2V/V2G applications," 2017 IEEE Transportation Electrification Conference (ITEC-India), pp. 1-6, 2017.
- [39] M. C. Falvo, D. Sbordone, I. S. Bayram and M. Devetsikiotis, "EV charging stations and modes: International standards," 2014 International Symposium on Power Electronics, Electrical Drives, Automation and Motion, pp. 1134-1139, 2014.
- [40] S. Habib, M. M. Khan, F. Abbas, L. Sang, M. U. Shahid and H. Tang, "A Comprehensive Study of Implemented International Standards, Technical Challenges, Impacts and Prospects for Electric Vehicles," in *IEEE Access*, vol. 6, pp. 13866-13890, 2018.

- [41] Das, H.S. & Rahman, Mohammad & Li, S. & Tan, C.W., "Electric vehicles standards, charging infrastructure, and impact on grid integration: A technological review," *Renewable and Sustainable Energy Reviews*, Vol. 120, 2020.
- [42] A. Sharma and R. Gupta, "Bharat DC001 Charging standard Based EV Fast Charger," *IECON 2020 The 46th Annual Conference of the IEEE Industrial Electronics Society*, pp. 3588-3593, 2020.
- [43] Standardisation of protocol for EV charging infrastructure 2017, [online] Available:
<https://dhi.nic.in/writereaddata/UploadFile/REPORT%20OF%20COMMITTEE636469551875975520.pdf>
- [44] Propelling Electric vehicles in India 2017, [online] Available:
<https://beeindia.gov.in/sites/default/files/2019%20-%20EY%20to%20BEE%20-%20Technical%20study%20on%20EVs%20%26%20Charging%20Infrastructure.pdf>
- [45] A. Gambhir, "Safety considerations for EV charging in India: Overview of global and Indian regulatory landscape with respect to electrical safety," 2017 IEEE Transportation Electrification Conference (ITEC- India), pp. 1-5, 2017.
- [46] SAE Electric Vehicle and Plug-in Hybrid Electric Vehicle Conductive Charge Coupler, SAE J1772, Jan. 2010.
- [47] International standard IEC 62196 2003, [online] Available:
https://webstore.iec.ch/preview/info_iec62196-1%7Bed1.0%7Den.pdf.
- [48] "Standard Technical Specifications of a DC Quick and Bi-directional Charger for Use with Electric Vehicles", IEEE 2030.1.1.
- [49] CHAdeMO protocol development 2021, [online] Available:
<https://www.chademo.com/activities/protocol-development>.
- [50] Connection set for conductive charging of electric vehicles 2015, [online] Available: <https://www.chinesestandard.net/PDF.aspx/GBT20234.1-2015>.
- [51] A. Mallik, J. Lu and A. Khaligh, "Sliding Mode Control of Single-Phase Interleaved Totem-Pole PFC for Electric Vehicle Onboard Chargers," in *IEEE Transactions on Vehicular Technology*, vol. 67, no. 9, pp. 8100-8109, Sept. 2018,

doi: 10.1109/TVT.2018.2848238.

- [52] A. Emadi, A. Khaligh, C. H. Rivetta and G. A. Williamson, "Constant power loads and negative impedance instability in automotive systems: definition, modeling, stability, and control of power electronic converters and motor drives," in *IEEE Transactions on Vehicular Technology*, vol. 55, no. 4, pp. 1112-1125, July 2006, doi: 10.1109/TVT.2006.877483.
- [53] Y. Yang, J. Pan, H. Wen, Z. Zhang, Z. Ke and L. Xu, "Double-Vector Model Predictive Control for Single-Phase Five-Level Actively Clamped Converters," in *IEEE Transactions on Transportation Electrification*, vol. 5, no. 4, pp. 1202-1213, Dec. 2019, doi: 10.1109/TTE.2019.2950510.
- [54] J. Kim, H. H. Choi and J. Jung, "MRAC-Based Voltage Controller for Three-Phase CVCF Inverters to Attenuate Parameter Uncertainties Under Critical Load Conditions," in *IEEE Trans. on Power Electron.*, vol. 35, no. 1, pp. 1002-1013, Jan. 2020.
- [55] T. D. Do, V. Q. Leu, Y. S. Choi, H. H. Choi, and J. W. Jung, "An adaptive voltage control strategy of three-phase inverter for stand-alone distributed generation systems," *IEEE Trans. Ind. Electron.*, vol.60, no.12, pp.5660– 5672, Dec. 2013.
- [56] Aakash Kumar Seth, Mukhtiar Singh, Modified repetitive control design for two stage off board Electric Vehicle charger, *ISA Transactions*,2021, ISSN0019-0578, <https://doi.org/10.1016/j.isatra.2021.09.015>.
- [57] Falkowski, P.; Sikorski, A. Finite control set model predictive control for grid-connected AC–DC converters with LCL filter. *IEEE Trans. Ind. Electron.* 2017, 65, 2844–2852.
- [58] B. A. Francis, and W. M. Wonham, "The internal model principle for linear multivariable regulators," *Appl. Math. Optimization*, vol. 2, no. 2, pp. 170–194, 1975.
- [59] P. C. Loh, Y. Tang, F. Blaabjerg, and P. Wang, "Mixed-frame and stationary-frame repetitive control schemes for compensating typical load and grid harmonics," *IET Power Electron.*, vol. 4, no. 2, pp. 218–226, 2011.
- [60] D. Kim and B. Lee, "Asymmetric Control Algorithm for Increasing Efficiency of

- Nonisolated On-Board Battery Chargers With a Single Controller," in IEEE Transactions on Vehicular Technology, vol. 66, no. 8, pp. 6693-6706, Aug. 2017, doi: 10.1109/TVT.2017.2655118.
- [61] C. Tan, Q. Chen, L. Zhang and K. Zhou, "Frequency-Adaptive Repetitive Control for Three-Phase Four-Leg V2G Inverters," in IEEE Transactions on Transportation Electrification, vol. 7, no. 4, pp. 2095-2103, Dec. 2021, doi: 10.1109/TTE.2021.3063467.
- [62] A. K. Seth and M. Singh, "Second-Order Ripple Minimization in Single-Phase Single-Stage Onboard PEV Charger," in IEEE Transactions on Transportation Electrification, vol. 7, no. 3, pp. 1186-1195, Sept. 2021, doi: 10.1109/TTE.2021.3049559.
- [63] M. Rashed, C. Klumpner, and G. Asher, "Repetitive and resonant control for a single-phase grid-connected hybrid cascaded multilevel converter," IEEE Trans. Power Electron., vol. 28, no. 5, pp. 2224–2234, May 2013.
- [64] Y. Fu, N. Cui, J. Song, Z. Chen, C. Fu and C. Zhang, "A Hybrid Control Strategy Based on Lagging Reactive Power Compensation for Vienna-Type Rectifier," in IEEE Transactions on Transportation Electrification, vol. 7, no. 2, pp. 825-837, June 2021, doi: 10.1109/TTE.2020.3030277.
- [65] O. C. Onar, J. Kobayashi and A. Khaligh, "A Fully Directional Universal Power Electronic Interface for EV, HEV, and PHEV Applications," IEEE Transactions on Power Electronics, vol. 28, no. 12, pp. 5489-5498, 2013.
- [66] A. Narula and V. Verma, "Bi directional trans Z source boost converter for G2V/V2G applications," in IEEE Transportation Electrification Conference (ITEC-India), Pune, 2017.
- [67] M. Singh, "Adaptive Network-Based Fuzzy Inference System for Sensorless Control of PMSG Based Wind Turbine with Power Quality Improvement Features," Ecole De Technologie Superieure, Montreal, 2010.